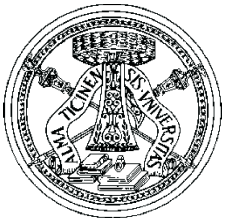

UNIVERSITY OF PAVIA

DEPARTMENT OF PHYSICS "ALESSANDRO VOLTA"

Dottorato di Ricerca in Fisica – XVIII ciclo –

NONLINEAR OPTICAL PROPERTIES OF PLANAR MICROCAVITIES AND PHOTONIC CRYSTAL SLABS

Doctoral thesis by

MARCO LISCIDINI

Supervisor: Prof. Lucio Claudio ANDREANI

to
Daniele, Dario and Matteo

Quid autem habes, quod non accepisti?

Contents

Introduction

Nonlinear optics has become increasingly important during the last decades because it has found application in the telecommunication field, especially for what concerns the propagation of optical signals in dielectric fibers and, above all, because of the possibility of exploiting harmonic generation in order to obtain coherent light in different spectral regions [1, 2].
Harmonic beam generation was observed for the first time in 1961 by Franken *et al.* and, just one year later, Bass *et al.* demonstrated the possibility to obtain monochromatic waves characterized by frequencies equal to a linear combination of those of incident waves on the sample [3, 4]. This process can be briefly summarized as it follows: while two monochromatic waves of frequencies ω_1 and ω_2 propagate in a nonlinear medium, they generate a nonlinear polarization that can be seen as an ensemble of dipoles that oscillate at multiple frequencies, or in general equal to a linear combination of ω_1 and ω_2. For example, when ω is converted to 2ω we have the so-called second harmonic generation (SHG) process and when we get 3ω we have third harmonic generation (THG). As a matter of fact the nonlinear polarization is the source of electromagnetic waves at frequencies different from the initial one. If we look at the experiments of Franken *et al.*, we observe that nonlinear effects in a dielectric medium are usually quite small and they require very powerful sources. Thus most of the efforts during these years have been devoted to achieve high enhancement of the harmonic generation process, in more and more compact devices, and to reduce the input power. Associated to harmonic generation is the occurrence of a *phase matching* condition, i.e. when harmonic beam propagates in phase with the nonlinear polarization. In such case the conversion efficiency is highly enhanced.

Since the first studies on second-harmonic generation (SHG), periodic structures have been indicated as suitable systems for achieving the phase matching condition even in cubic materials like GaAs, where there is no birefringence to compensate the refractive index dispersion [5, 6]. Other forms of phase matching have also been proposed, like using form birefringence induced by refractive index modulation in the long-wavelength limit [7, 8] or incorporating a separated quantum well region in the nonlinear media [9]. Another possible route for increasing SHG is to embed the nonlinear source in a Fabry-Pérot cavity, in order to enhance the pump field intensity

or to optimize the extraction efficiency of the harmonic field. Several studies have been conducted on external cavities [10, 11], where it is relatively easy to achieve double-resonance for both the pump and harmonic frequencies. Concerning monolithic cavities with dielectric mirrors, most studies focused on SHG in the presence of a single resonance [12, 13]. A doubly-resonant microcavity (DRM) is desirable since the performance of the structure can be optimized at both pump and harmonic frequencies [14–16].

In the last few years the concept of a photonic crystal has been increasingly applied to nonlinear optics [17, 18], especially for what concerns frequency conversion. The possibility of tailoring the dispersion relation through a periodic modulation of the refractive index gives additional degrees of freedom to achieve phase matching, moreover using the high density of states at the band edges allows increasing the amount of pump power available in the nonlinear layers [19–24].
More recently, one- and two-dimensional photonic crystal structures embedded in self-standing membrane [25] or in a planar waveguide [26] have been proposed as suitable platforms for integrated photonic circuits. In this structure light confinement along the vertical direction is determined by the waveguide, while the photonic pattern modifies propagation of light in the plane. These systems have attracted much attention since they can exhibit many properties of 3D photonic crystals but they are much easier to fabricate at sub-micron lengths. Theoretical and experimental studies have already demonstrated the possibility of achieving several order of magnitude enhancement of harmonic generation in carefully designed structures [27, 28].
Among many solutions, the choice of a Silicon-On-Insulator (SOI) waveguide offers great advantages in view of future integration of photonic devices. Indeed the SOI planar waveguide is characterized by a large refractive index contrast which allows good light confinement in a thin waveguide and, above all, the great development of silicon integrated circuits offers a high degree of control of processing technology.

The aim of this work is to give an original contribution to the knowledge of harmonic generation of light in photonic systems of present interest, such as planar microcavities and photonic crystals slabs. Our research study is mainly devoted to the understanding of the conditions that determine a considerable enhancement in the conversion efficiency, thereby providing some guidelines to the design of new devices.
For what concerns SHG, we concentrate our attention on doubly resonant microcavities: their design is challenging because of the refractive index dispersion. In this thesis we have developed an efficient method in order to solve this problem and to enhance SHG as much as possible. The nonlinear response of the DRM has been investigated in the case of bulk nonlinear-

ities and when it arises from symmetry breaking at the interfaces between two different media. In the first case we have considered cavities made of GaAs or AlGaAs embedded between Alox/AlGaAs dielectric mirrors, and we present theoretical results obtained in the un-depleted pump approximation. In the second case we present theoretical and experimental results regarding the nonlinear response of a doubly resonant microcavity of amorphous silicon nitride, whose design has been carried out with the method developed in this thesis.
A theoretical analysis of THG in the case SOI PhC slabs has been performed and compared with the experimental results. For the analysis of THG in photonic crystal slabs we have developed a numerical method, based on the well known linear scattering matrix theory [29]. This new method allows to treat nonlinear interactions in layered two-dimensional systems and we hope it is suitable for the investigation of nonlinear phenomena in several kind of photonic structures.

The work is organized as it follows. In chapter 1 we discuss some aspects of the nonlinear interaction which takes place in a bulk medium or at the interface between two media. The purpose of this chapter is to provide the necessary instruments for understanding the subsequent chapters, where second- and third- harmonic generation are analyzed in more complicated systems.
Second-harmonic generation in the case of a doubly resonant microcavity is discussed in detail in Chapter 2, where we present first a study of the linear properties of the microcavity and its design method, followed by nonlinear results for bulk and surface nonlinearities. In Chapter 3 we present the numerical method used for the calculation of THG in the case of PhC slabs, then we discuss the linear and nonlinear properties and finally we compare the results with the experimental data. Since the nonlinear response of the photonic crystal slab arises from a superposition of the effects of the SOI waveguide and the photonic crystal pattern, we present first the study of the un-patterned waveguide followed by those of the PhC slab.

This work is closely related to projects carried out by the Solid State Theory group of the University of Pavia at Department of Physics "A. Volta", headed by Prof. L. C. Andreani. Part of the work has been financed by "Istituto Nazionale per la Fisica della Materia" (INFM) through the project PRA-Photonic, and supported by MIUR through FIRB project "Miniaturized electronics and photonic system" as well as Cofin programs. The experimental results presented in this work has been obtained by the Department of Electronic (LAILAM - Laboratorio di Interazione Radiazione Materia) for SOI photonic crystal slabs and by University of Napoli and Politecnico di Torino in the case of amorphous silicon nitride microcavities.

Chapter 1

Elements of Nonlinear Optics

The purpose of this chapter is to introduce some basic concepts of nonlinear optics, especially for what concerns harmonic generation. First of all, in Sec. 1.1 we will try to understand which are the origins of the nonlinear response and how it can be described in a simple system, such as a single atom, using the anharmonic oscillator model. In Secs. 1.2 and 1.3 the problem of second harmonic generation will be analyzed in the case of bulk and surface nonlinearities. Finally, in the last part we shall introduce some important physical quantities which describe the nonlinear response of a system.
A detailed discussion of these topics is beyond the aim of this chapter and the reader can find a more complete treatment in several specialized textbooks [30–33].

1.1 Nonlinear Dielectric Response

The interaction of the electromagnetic radiation with matter will be treated within a macroscopic framework, i.e. we shall always deal with electric fields whose wavelength is several times larger than the size of the atoms and the interatomic bonds, characterizing the systems of interest. In this context, the electromagnetic properties can be described through the Maxwell equations, which can be written in the absence of sources as

$$\nabla \cdot \mathbf{D} = \mathbf{0} \qquad \nabla \cdot \mathbf{B} = \mathbf{0} \tag{1.1}$$

$$\nabla \times \mathbf{E} = -\frac{1}{c}\frac{\partial \mathbf{B}}{\partial t} \qquad \nabla \times \mathbf{H} = \frac{\mathbf{1}}{\mathbf{c}}\frac{\partial \mathbf{D}}{\partial \mathbf{t}}. \tag{1.2}$$

From now we assume nonmagnetic media (i.e. $\mathbf{B} = \mathbf{H}$) and absence of external currents or charges (i.e. $\rho = \mathbf{J} = 0$). The vectors $\mathbf{E}$ and $\mathbf{H}$ are the

electric and magnetic fields, respectively, while the electric displacement $\mathbf{D}$ is given by

$$\mathbf{D} = \mathbf{E} + 4\pi\mathbf{P}, \tag{1.3}$$

where $\mathbf{P}$ is the electric dipole moment for unit of volume. The polarization $\mathbf{P}$ is a complicated function of the electric field and it depends on the physical and chemical nature of the materials considered.
We can notice that an electron bound to an atom or molecule, or moving through a solid, experiences electric fields of the order of 10^9 V/cm. We shall assume to work with electric fields several times smaller than this value, so that $\mathbf{P}(\mathbf{r}, t)$ can be treated as locally and instantaneously dependent on the electric field. This assumption is strongly restrictive and there are many implications of a more realistic relation between $\mathbf{E}$ and $\mathbf{P}$. Nevertheless, it allows introducing some of the most important concepts while keeping the discussion to a reasonable degree of complexity.

Nonlinear susceptibility

Under this approximation, each component of the polarization vector can be expanded in a Taylor series of powers of the electric field

$$\begin{aligned} P_i(\mathbf{r}, t) = &\sum_j \chi^{(1)}_{ij} E_j(\mathbf{r}, t) + \sum_{jk} \chi^{(2)}_{ijk} E_j(\mathbf{r}, t) E_k(\mathbf{r}, t) \\ &+ \sum_{jkh} \chi^{(3)}_{ijkl} E_j(\mathbf{r}, t) E_k(\mathbf{r}, t) E_l(\mathbf{r}, t) + \cdots , \end{aligned} \tag{1.4}$$

where the $\chi^{(1)}_{ij}$ are the elements of a linear susceptibility tensor and $\chi^{(2)}_{ijk}$ and $\chi^{(3)}_{ijkl}$ are referred to as the second and third nonlinear susceptibilities, respectively.[1] As indicated by the notation used in Eq. (1.4), the linear and nonlinear responses of a medium are described through tensorial objects whose rank depends on the interaction order. The susceptibility tensors have explicit form reflecting the structural symmetry of the medium. In the following, we shall briefly discuss some important properties of these tensors which derive from simple symmetry considerations. During this work we shall deal with isotropic media, or cubic materials, for which the linear response has the same direction of the applied electric field. Nevertheless, we cannot forget that, in nonlinear optics there are several effects related to the tensorial nature of the linear response.[2]

In any real medium, the polarization vector, $\mathbf{P}(\mathbf{r}, t)$, does not depend only on the value of the electric field at the point $\mathbf{r}$ at the instant t. In

[1] Here we have not consider the first term of the Taylor series that corresponds to a spontaneous electric dipole moment which characterizes a particular class of materials, known as ferroelectrics.

[2] A very important class of materials is the birefringent one. These media are characterized by diagonal linear tensor with two different eigenvalues lead to the ordinary and extraordinary refractive indices.

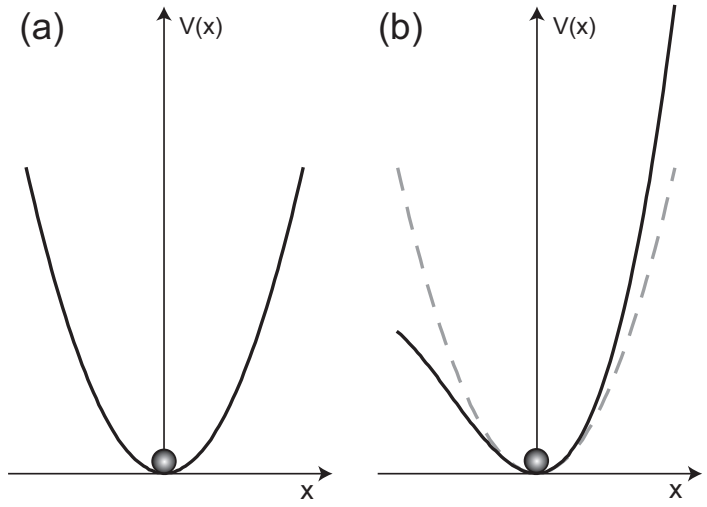

Figure 1.1: Electron in harmonic potential $V(x) = \frac{1}{2}m\omega_0 x^2$ (a) and in the case of cubic potential $V(x) = \frac{1}{2}m\omega_0 x^2 + \frac{1}{3}m\xi x^3$ (b). The presence of a cubic term in the potential V(x) breaks the symmetry respect to the vertical axes and gives origin to a nonlinear motion of the electron.

fact there is a time lag in the response of the medium. Such consideration results in a relation more complicated than Eq. (1.4).
If we consider the electric field **E** as a sum of monochromatic plane waves, this relation can be written, in a simpler way, in a Fourier space as

$$\mathbf{P}(\mathbf{k},\omega) = \mathbf{P^{(1)}}(\mathbf{k},\omega) + \mathbf{P^{(2)}}(\mathbf{k},\omega) + \cdots \tag{1.5}$$

where [3]

$$\mathbf{P^{(1)}}(\mathbf{k},\omega) = \chi^{(1)}(\mathbf{k},\omega) : \mathbf{E}(\mathbf{k},\omega), \tag{1.6}$$
$$\mathbf{P^{(2)}}(\mathbf{k},\omega) = \chi^{(2)}(\mathbf{k} = \mathbf{k}_1 + \mathbf{k}_2, \omega = \omega_1 + \omega_2) : \mathbf{E}(\mathbf{k}_1,\omega_1)\mathbf{E}(\mathbf{k}_2,\omega_2). \tag{1.7}$$

We assume to work only in the dipole approximation, therefore in the following discussions dependence of $\chi^{(n)}$ on **k** will be neglected.

Before starting our study on the harmonic generation phenomena in materials, let us consider a short example in order to better understand the origin of the nonlinear terms appearing in Eqs. (1.4) and (1.5).
We consider an electron that is bound to an infinitely massive center owing to a given potential $V(x)$. In the one-dimensional case the equation for the electron motion can be written as

$$m\ddot{x} + m\Gamma\dot{x} + \frac{\partial V(x)}{\partial x} = -eE(t) \tag{1.8}$$

[3] Here the symbol **:** indicates the tensorial product

Lorentz model

where m is the free electron mass, Γ is a damping rate and $E(t)$ is the external applied scalar electric field. For the harmonic potential $V(x) = \frac{1}{2}m\omega_0 x^2$, this problem reduces to the well known Lorentz model. If we consider an electric field

$$E(t) = E(\omega)e^{-\imath\omega t} + c.c.$$

it is easy to find that the motion of the electron is described by the equation

$$\begin{aligned} x(t) &= x(\omega)e^{\imath\omega t} + c.c. \\ &= -\frac{e}{m}E(\omega)\frac{e^{\imath\omega t}}{\omega_0^2 - 2\imath\gamma\omega - \omega^2} + c.c. \end{aligned} \tag{1.9}$$

The applied electric field $E(t)$ induces an electric dipole moment in the atom $p(x) = ex(t)$. If we consider an ensemble of atoms, with an electron density N, it is possible to provide an analytic expression for the nonlinear susceptibility

$$\chi(\omega) = \frac{Ne^2}{m}\frac{1}{\omega_0^2 - 2\imath\gamma\omega - \omega^2}\,. \tag{1.10}$$

Let us suppose, now, to drive the electron with two superimposed electric fields, with frequencies ω_1 and ω_2 respectively. We observe that the resulting displacement is the simple superposition of those at frequencies ω_1 and ω_2, which have the same expression of Eq. (1.9). Therefore, with a harmonic potential no second harmonic generation, or a interaction between the two input waves occur.

The latter example shows that if we wish to describe any frequency mixing we have to go beyond the harmonic approximation by considering a more complex potential, $V(x)$. Thus, we extend the previous model by introducing an anharmonic term [33].

$$V(x) = \frac{1}{2}m\omega_0 x^2 + \frac{1}{3}m\xi x^3 \tag{1.11}$$

Equation (1.8) then becomes:

$$\ddot{x} + \Gamma\dot{x} + \omega_0^2 x + \xi x^2 = -\frac{eE(t)}{m}\,. \tag{1.12}$$

Anharmonic oscillator

Because of the quadratic term, Eq. (1.12) cannot be solved in the same way as the linear Lorentz model. However, since in general the anharmonic term is very small compared to the harmonic one, it is possible to assume a solution in the form of a power series

$$x(t) = x_1(t) + x_2(t) + x_3(t) + \cdots\,. \tag{1.13}$$

where each term, $x_i(t)$, is proportional to the i-th power of the applied field, $E(t)$. If we consider again an external field given by the superposition of two plane waves, the nonlinear term appearing in (1.12) gives rise to a frequency mixing. Therefore, the propagating electromagnetic field generates a nonlinear polarization that oscillates at frequencies which are linear combinations of ω_1 and ω_2.

Even in this case we can derive an analytic expression for the linear polarization, which is identical to Eq. (1.10), but we can also provide an expression for the second-order nonlinear susceptibility. In particular, for the case of frequency sum $\omega_1 + \omega_2$, we get

$$\chi^{(2)}(\omega_3 = \omega_1 + \omega_2) = -\frac{m\xi}{N^2 e^3}[\chi^{(1)}(\omega_1)][\chi^{(1)}(\omega_2)][\chi^{(1)}(\omega_3)] \tag{1.14}$$

The analysis of this simple model can help to better understand some characteristics of the nonlinear interaction. First of all, we notice that the nonlinear interaction has its origin in the potential that the electrons, or more generally the charges, experience. Such potential, which cannot be simply an harmonic one, and the nonlinear response must reflects its symmetry properties. In particular, it is worth noting that if we consider an even potential (i.e $V(x) = V(-x)$), we would not observe any second-order nonlinear effect [4]. Such model can be extended to the case of higher order susceptibility tensors by considering a more complex potential, $V(x)$, in Eq. (1.8).

Another important information can be obtained by observing the three dimensional generalization of the Eq. (1.14) ***Miller's rule***

$$\chi^{(2)}_{ijk}(\omega_3 = \omega_1 + \omega_2) = \Delta_{ijk}[\chi^{(1)}_{ii}(\omega_1)][\chi^{(1)}_{jj}(\omega_2)][\chi^{(1)}_{kk}(\omega_3)] \tag{1.15}$$

This result is known as "Miller's rule" [34]. The coefficient Δ_{ijk} can be empirically determined and Miller has shown that it is almost constant for a wide range of materials. This rule has turned out to be a very important one in the search for new nonlinear media, since it tells basically that high refractive index corresponds to high nonlinear coefficient.

In the example we have just described, we assume a solution in the form of a Taylor series by making the hypothesis that the nonlinear interaction is small compared to the linear one. It is worth spending few words about the order of magnitude of the nonlinear susceptibilities in dielectric media, which will be considered in the next examples and chapters.

The dominant contribution to the nonlinear susceptibility at optical frequencies is due to the outermost electrons of the atoms constituting the material, which experience an average electric field E_a. In practice, the

[4] This is, in general, the case of amorphous media, or Si and Ge, in which the second-order nonlinear susceptibility , $\chi^{(2)}$, is very small and it is due only to quadrupole terms.

Semiconductor	$\chi^{(2)}_{\xi\xi\xi}$ (10^{-6} esu)	$\chi^{(3)}_{\xi\xi\xi\xi}$ (10^{-10} esu)
Ge	–	$6.0 \pm 50\%$
Si	–	$0.32 \pm 50\%$
GaAs	2.0	0.5 [a]
InAs	2.4	0.6 [a]

(a) Theoretical values

Table 1.1: Second- and third- order nonlinear susceptibilities for some typical semiconductor materials. In the coordinate system defined by crystallographic axes, the only non-vanishing components of $\chi^{(2)}_{ijk}$ for these materials correspond to $i \neq j \neq k$. In the table for III-V compound $\chi^{(2)}_{\xi\xi\xi} = \frac{2}{\sqrt{3}}\chi^{(2)}_{ijk}$, while for the Si and Ge $\chi^{(3)}_{\xi\xi\xi\xi} = \frac{1}{3}(\chi^{(3)}_{iiii} + 6\chi^{(3)}_{iijj})$.

nonlinear effect starts to be significant only when the incident field intensity is of the same order of magnitude as this field. We can therefore estimate that the average second- and third-order nonlinear susceptibilities scale as $\langle\chi^{(2)}\rangle \sim \langle\chi^{(1)}\rangle/E_a$ and $\langle\chi^{(3)}\rangle \sim \langle\chi^{(1)}\rangle/E_a^2$, respectively, where $\langle\chi^{(1)}\rangle$ indicates the average value of the linear susceptibility. In Table 1.1, the nonlinear susceptibilities of some typical semiconductor are reported as a guide for the reader [33, 35–37].

1.2 Second Harmonic Generation

In the example of the anharmonic oscillator we have seen that when two monochromatic waves at different frequencies ω_1 and ω_2 propagate within a medium characterized by $\chi^{(2)} \neq 0$, they induced a nonlinear polarization that oscillates at frequencies which are a linear combination of ω_1 and ω_2. The polarization can be viewed as an ensemble of oscillating dipoles, or antennas, which are source of electromagnetic waves. As a result, we assist to a partial or total frequency conversion of the initial field. In this Section we shall briefly describe the simplest case of frequency conversion i.e. the second harmonic generation (SHG).

Nonlinear wave equation

The electromagnetic field propagation in a medium is described by the equation

$$\left[\nabla \times (\nabla \times) + \frac{1}{c^2}\frac{\partial^2}{\partial t^2}\varepsilon\cdot\right]\mathbf{E}(\mathbf{r},t) = -\frac{4\pi}{c^2}\frac{\partial^2}{\partial t^2}\mathbf{P}^{NL}(\mathbf{r},t) \qquad (1.16)$$

where $\mathbf{P}^{NL}$ indicates the nonlinear polarization. We now restrict ourselves

to the one-dimensional problem, and we assume the field propagation along the direction $\hat{\mathbf{z}}$. As we are interested in the description of the second harmonic generation, we limit our discussion to two interacting waves: the so called *pump* field, at frequency ω, and the second harmonic one at frequency 2ω, which can be written as

$$\begin{aligned}\mathbf{E}_{\omega}(z,t) &= \mathbf{E}_{\omega}(z)e^{-\imath(\omega t - k_{\omega}z)} \\ \mathbf{E}_{2\omega}(z,t) &= \mathbf{E}_{2\omega}(z)e^{-\imath(2\omega t - k_{2\omega}z)}.\end{aligned} \tag{1.17}$$

Here $k(\omega) = \omega n(\omega)/c$ is the wave vector of the pump field. Since we are working with complex fields, even the complex conjugate counterpart of the Eq. 1.17 has to be considered.

Second-Harmonic Generation

From the Eqs. (1.7) and (1.17), we can write the nonlinear polarization at the pump and the harmonic frequencies as

$$\mathbf{P}^{NL}_{\omega}(z,t) = \chi^{(2)} : \mathbf{E}^{*}_{\omega}(z,t)\mathbf{E}_{2\omega}(z,t)e^{-\imath[\omega t - (k_{2\omega} - k_{\omega})z]} \tag{1.18}$$

$$\mathbf{P}^{NL}_{2\omega}(z,t) = \chi^{(2)} : \mathbf{E}_{\omega}(z,t)\mathbf{E}_{\omega}(z,t)e^{-\imath(2\omega t - 2k_{\omega}z)} \tag{1.19}$$

In the linear case of isotropic medium, or in a cubic material when the propagation of the electromagnetic wave is along one of the principal axes, the polarization and field lie in the xy plane. However, when the nonlinear interaction is considered, even in such a simple case, the nonlinear polarization (and therefore the pump and harmonic fields) is not transverse respect to the propagation direction. In this case, it is worth decomposing $\mathbf{P}^{NL}$ and $\mathbf{E}$ in the sum of transverse ($\perp$) and the longitudinal ($\parallel$) components (see Fig. 1.2). Now, Eq. (1.16) can be written for the pump and harmonic field as[5]

$$\begin{aligned}\frac{\partial^2}{\partial z^2}\mathbf{E}_{\omega_i,\perp} + \omega_i^2\frac{\varepsilon_{\perp(\omega_i)}}{c^2}\mathbf{E}_{\omega_i,\perp} + \frac{4\pi\omega_i^2}{c^2}\mathbf{P}^{NL}_{\omega_i,\perp} \\ +\hat{\mathbf{z}}\left[\omega_i^2\frac{\varepsilon_{\parallel}(\omega_i)}{c^2}E_{\omega_i,\parallel} + \frac{4\pi\omega_i^2}{c^2}P^{NL}_{\omega_i,\parallel}\right] = 0\end{aligned} \tag{1.20}$$

while the first of Eqs. (1.1) gives

$$\frac{\partial}{\partial z}\left[\varepsilon_{\parallel}(\omega_i)E_{\omega_i,\parallel} + 4\pi P^{NL}_{\parallel}\right] = 0. \tag{1.21}$$

Here we have introduced $\varepsilon_{\parallel}$ and $\varepsilon_{\perp}$, which describe the linear dielectric response along the directions parallel and perpendicular to the pump propagation axis, respectively.

Non-depletion approximation

As a matter of fact, we obtain a system of nonlinear differential equations in which the presence of the nonlinear polarization terms couples Eqs.

[5]It is straightforward to show that $\nabla \times \nabla \times \mathbf{E} = \partial^2\mathbf{E}_{\perp}/\partial z^2$.

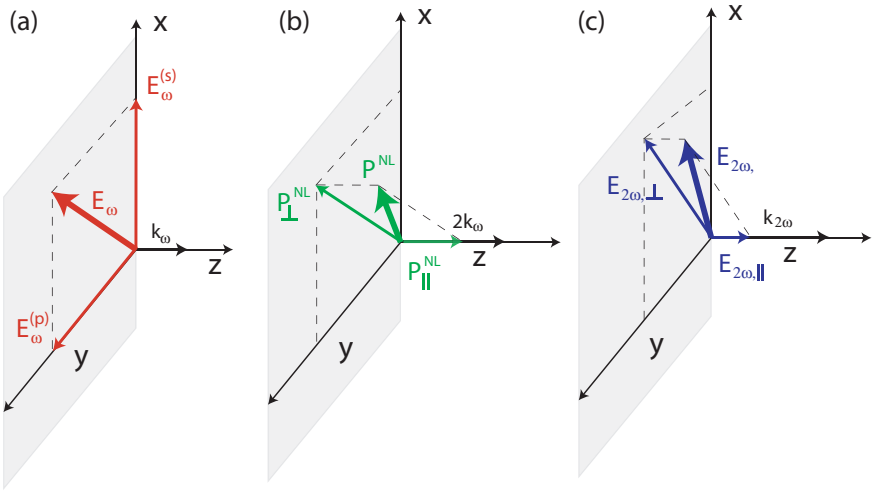

Figure 1.2: (a) If we neglect any nonlinear effect on the pump field we get that it is transverse respect to the propagation direction. (b) The direction of the nonlinear polarization generated depends on the tensor shape and in general it is different from the incident one. The nonlinear interaction propagates with a wave vector equal to $2\mathbf{k}_\omega$. (c) Finally, the second harmonic field generated by the nonlinear polarization propagates with a wave vector $\mathbf{k}_{2\omega}$ and the electromagnetic field has a transverse component and one along the propagation direction.

(1.20) for the pump and harmonic fields. As the two waves propagate through the nonlinear medium, the electromagnetic energy is transferred from the fundamental to the second harmonic, and viceversa. A general solution of this problem is complicated even in this simple case, nevertheless we can introduce a further simplification: in the following discussion, we shall assume that the pump field propagates linearly, neglecting the pump intensity depletion due to the harmonic generation. This assumption is known as *pump non-depletion approximation*. As a matter of fact, this is not a physically unrealistic situation. Indeed, as we have seen in the previous Section, the nonlinear coefficients are very small and thus, in many cases, the amount of radiation generated is small as well.

In this approximation the solution of Eq.(1.21) is immediately given by

$$E_{\omega_i,\parallel}(z) = -\frac{4\pi}{\varepsilon_\parallel(\omega_i)} P_\parallel^{NL}(z). \tag{1.22}$$

Then, by inserting the expression of $E_\parallel$ in (1.20) we obtain a new equation

for the transverse generated field, which is written as

$$\left(\frac{\partial^2}{\partial z^2} + k_{2\omega}^2\right)\mathbf{E}_\perp(z) = -\frac{16\pi\omega^2}{c^2}\mathbf{P}_\perp^{NL}(z). \tag{1.23}$$

The transversal component of the harmonic field can be found easily in the limit of *slowly varying envelope approximation*, when Eq. (1.23) becomes[6]

$$\frac{\mathrm{d}E_{2\omega}(z)}{\mathrm{d}z} = -\imath\frac{8\pi\omega^2}{k_{2\omega}c^2}\bar{\chi}^{(2)}E_\omega^2(z)e^{\imath\Delta k} \tag{1.24}$$

where $\Delta k = 2k_\omega - k_{2\omega}$. Notice that Eq. (1.24) is a scalar equation, since we can write $\mathbf{E}_{2\omega} = \hat{\mathbf{e}}E_{2\omega}$, with $\hat{\mathbf{e}}$ directed as $\mathbf{P}_\perp^{NL}$, while $\bar{\chi}^{(2)}E_\omega^2$ is the amplitude of the effective transverse nonlinear polarization.

Now, let us suppose that at the surface of the nonlinear material ($z = 0$) the harmonic field vanishes, while it builds up as the pump field propagates within the medium and is expressed as

$$E_{2\omega}(z) = -\frac{16\pi\imath\omega^2}{k_{2\omega}c^2}\bar{\chi}^{(2)}E_\omega^2\,\frac{\sin(\Delta kz/2)}{\Delta k}\,e^{\imath\frac{\Delta kz}{2}}. \tag{1.25}$$

The energy per unit area and unit time is determined by evaluating the corresponding Poynting vector

$$S_{2\omega}(z) = \frac{64\pi\omega^3|\bar{\chi}^{(2)}|^2}{c^3k_{2\omega}}|E_\omega|^4\,\frac{\sin^2(\Delta kz/2)}{(\Delta k^2)} \tag{1.26}$$

This simple result allows us making some important and general considerations on the second harmonic generation process, which are at the bases of several applications.

The first obvious consequence of Eq. (1.26) is that the strength of the nonlinear response depends on $|\chi^{(2)}|^2$, therefore the choice of the material is extremely important in the applications. In the previous Section, we have seen that Miller's rule can help in the search for best material. In this work we shall only deal with semiconductor materials, which are quite interesting not only because their considerable nonlinear properties, but also because of the high degree of control in the growth process, which gives the opportunity of creating artificial structures characterized by high $\chi^{(2)}$ values. In these systems, thanks to an optimization of the width and the composition of the different layers, it is possible to engineer the electronic and the optical properties [38, 39].

[6]Here we assume that the variation of the complex field amplitude with z is small enough to neglect the term $\mathrm{d}^2E_\perp/\mathrm{d}z^2 << -2k\mathrm{d}E_\perp/\mathrm{d}z$.

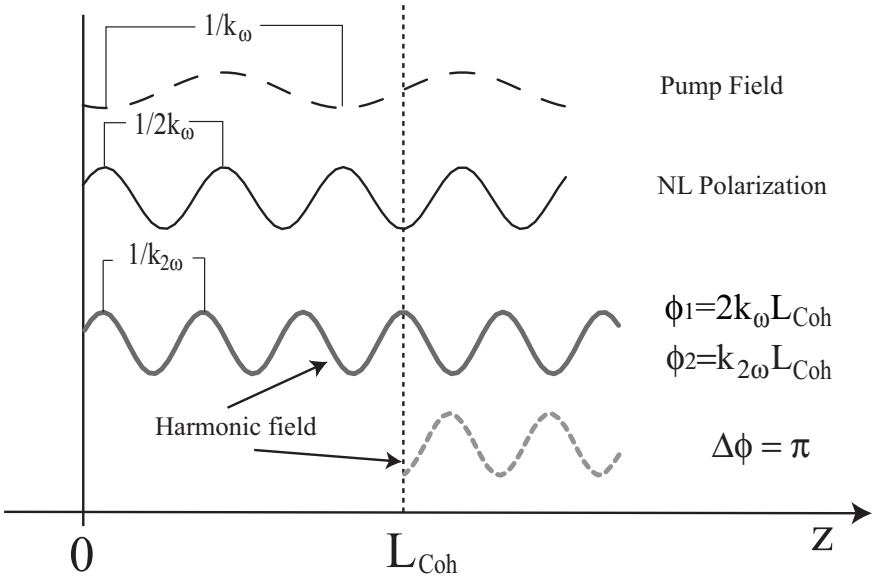

Figure 1.3: Because of the refractive index dispersion, the pump field and the harmonic generated one travel at the different velocities thus, in general, two contributions generated in two different points of the nonlinear medium are not in phase. The distance at which the two contribution are exactly in phase opposition is called coherent length (L_{Coh}).

Eq. (1.26) shows that the second harmonic intensity scales quadratically with $|E_\omega|^2$. This fact, even though not surprising, underlines that the possibility of achieving high pump field intensity in the nonlinear medium is a key point of nonlinear applications. In the present case, the pump power is just determined by the incident power (that is by the available laser source), but in other systems, high pump field intensity can be achieved, i.e., by exploiting resonance effects in a microcavity or slow group velocity at the photonic band edge [12, 13, 19–21]. Finally, another crucial parameter appearing in the expression (1.26) is Δk, which is a function of the phase velocities of the pump and harmonic waves. When the pump field propagates through the nonlinear medium, it generates a nonlinear polarization whose spatial periodicity is given by $1/2k_\omega$, while any second-harmonic generated wave propagates with a wave vector $k_{2\omega}$. If we consider two different contributions generated at z=0 and z=L, respectively, we observe a phase mismatch $\Delta\phi = 2k_\omega - k_{2\omega} = (\Delta k)L$. As a consequence, only the contributions generated within a length

Coherence length

$$L_{Coh} = \frac{\pi}{\Delta k} \tag{1.27}$$

will interfere constructively. Alternatively, the highest output we can expect to be generated from a nonlinear crystal is the signal from one coherence length, no matter how long the crystal is. If, on the other hand, $\Delta k = 0$ (*phase matching condition*), and in the pump non-depletion limit, the signal is proportional to the square of the crystal length.

Phase-matching techniques

Because of the natural material refractive index dispersion, in general the phase matching condition is not automatically fulfilled. Nevertheless several techniques have been proposed in order to exploit the total length of the nonlinear crystal even when it is larger than the coherence length. A first way to do this was suggested by Bloembergen et al. [5, 40] and it consist in a periodical modulation of the $\chi^{(2)}$ sign: if the period is taken equal to the coherence length, all the different contribution interfere constructively. This strategy is called *quasi-phase matching*. We notice that in this case the phase matching condition is not satisfied, since the dispersion of the refractive index is not compensated at all, and $\Delta k \neq 0$.

A method to obtain true phase matching (i.e. $\Delta k = 0$) is to employ the birefringence of a uniaxial crystal. In this method, proposed by Therhune et al. [41], and independently by Giordmaine [42], the refractive index dispersion is compensated by working with the pump and harmonic field which are differently polarized. In particular, if both the pump field components have the same polarization, we speak of "type-I" phase matching, otherwise the phase matching is called of "type-II".

Other forms of phase matching have also been proposed, like using form birefringence induced by refractive index modulation in the long-wavelength limit [7, 8] or incorporating a separated quantum well region in the nonlinear media [9]. The possibility of tailoring the dispersion relation through a periodic modulation of the refractive index, as it happens in photonic crystals, gives additional degrees of freedom to achieve phase matching [19, 21, 43].

1.3 Bulk and surface nonlinearities

In Sec. 1.1 and 1.2 we have treated the case of nonlinear response taking place in bulk matter. Nevertheless, on the surface of a material, or at the interface between two media, one can experience the presence of nonlinear interactions that differ distinctly and qualitatively from those we have seen in bulk materials. The origin of such nonlinearities lies in the low symmetry of the atomic and molecular sites at a surface. In particular, even a material with an inversion center, as gases, liquids or silicon and germanium, for which the bulk second-order nonlinear contribution vanishes, can exhibit second harmonic generation at the surface, or interface with another medium [44–47].

The experimental results collected in almost 40 years, clearly suggest that

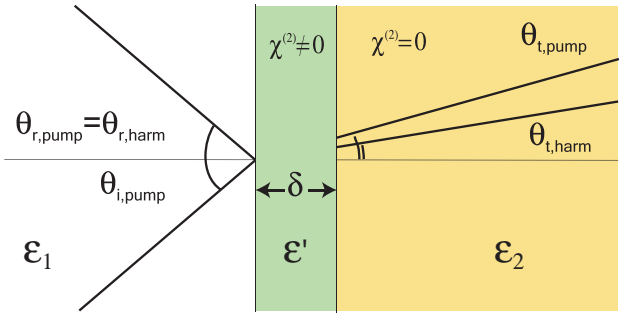

Figure 1.4: The surface nonlinear contribution is modeled introducing a layer of thin δ with a bulk nonlinearity $\chi^{(2)}$ whose non-null elements are the same of the surface tensor.

Surface nonlinearity

there are two distinct contributions to the surface nonlinearity. In the surface layer, or at an interface, the inversion symmetry is necessarily broken, and hence the second-order nonlinearity is nonvanishing in the dipole approximation. Nevertheless, the structural discontinuity can determine a field discontinuity at the surface leading to a quadrupole-type surface contribution. Notice, that the field discontinuity and the structural discontinuity contribute separately to the surface nonlinearity [48][7]. Since the nonlinear response depends on the surface geometry, where the inversion symmetry is broken, it follows that the second harmonic signal is a powerful probe of surface and interface shape.[49–51].

In this work we have conducted a study of systems in which the surface contribution plays a central rule in the nonlinear response. In order to model the surface nonlinearity, we have introduced an interface layer, characterized by an effective bulk nonlinearity (see Fig. 2.21). For our purposes, this layer can be defined as the region where the structure and the field change significantly. In general, the thickness δ of an interface layer is always much smaller than an optical wavelength and even in real cases the nonlinear contribution is originated in a small region, and not by an infinitesimal surface [32]. As we shall see, this approximation allows providing a description a multilayered system, in the case of interface nonlinearities by using the well known nonlinear transfer matrix method [52].

We discuss now the simple example of the second harmonic radiation from a plane of nonlinear dipoles for which an analytic approach is still possible. An incoming pump field at frequency ω from the medium 1 gives rise to a nonlinear polarization P^{NL} in the interface layer (see figure 2.21. This nonlinear source determines a reflected and transmitted field at frequency

[7] Let us consider, for example, a liquid-solid interface with a refractive index matching, only the structural contribution is present since the field is continuous along the interface.

2ω, here we shall consider only the reflected one.
We treat the nonlinear contribution as originated from a sheet of polarization embedded in an interface layer with a dielectric constant ε'[8], thus the $\mathbf{P}^{NL}$ has the form

$$\mathbf{P}^{NL}(z) = \mathbf{P}^{NL}\delta(z)\exp[i(2\mathbf{k}_\omega \cdot \mathbf{r} - 2\omega t)] \tag{1.28}$$

By solving the nonlinear wave equation (1.16) with the appropriate boundary conditions we obtain the reflected second-harmonic field amplitude for the p and s polarization respectively [53].

$$\mathbf{E}_p^{2\omega} = \frac{4\pi\imath k_1}{\varepsilon_2 k_{1z} + \varepsilon_1 k_{2z}} \left(k_{2z} P_x^{NL}\hat{\mathbf{x}} + \frac{\varepsilon_2}{\varepsilon'} k_x P_z^{NL}\hat{\mathbf{z}} \right) \tag{1.29}$$

$$\mathbf{E}_s^{2\omega} = \frac{4\pi\imath k_1}{k_{1z} + k_{2z}} \frac{k_{1z}}{\varepsilon_1} P_y^{NL}\hat{\mathbf{y}} \tag{1.30}$$

where k_1 and k_2 are the wave vectors of the harmonic field in the media 1 and 2 respectively; while x, y and z denote the components in the laboratory coordinate system, with $k_{1z} = k_1 \cos\theta_i$, $k_{2z} = k_2 \cos\theta_r$ and $k_{2x} = k_2 \sin\theta_r$. The angle θ_i is the incidence angle, while θ_r can be evaluated through the Snell's law. Finally P_x^{NL}, P_y^{NL} and P_z^{NL} are the Cartesian components of the second-order nonlinear polarization.

Nonlinear tensor shape

The knowledge of the reflected second-harmonic amplitude is determined only by the complete knowledge of the nonlinear polarization which is determined by the shape of the tensor $\chi^{(2)}$. For a planar interface, as the one considered in this example, the inversion symmetry is broken along the z axis, nevertheless the rotational symmetry around the z axis is preserved. As a result many of the 27 components of $\chi^{(2)}$ disappear. There are only seven non-vanishing components of the second order nonlinear tensor and, since there is also an equivalence of the x and y direction at an isotropic surface, only three tensor elements are independent:

$$\chi^{(2)}_{zzz} \tag{1.31}$$

$$\chi^{(2)}_{zxx} = \chi^{(2)}_{zyy} \tag{1.32}$$

$$\chi^{(2)}_{xxz} = \chi^{(2)}_{xzx} = \chi^{(2)}_{yyz} = \chi^{(2)}_{yzy} \tag{1.33}$$

Let us compare this result with the one obtained in the previous section for the harmonic generation in a nonlinear medium in the case of bulk $\chi^{(2)}$. The first important difference which characterizes the surface and the bulk response is that the first one is independent on the layer widths. Indeed, in the case just described we observe that the layer length, even the one of the

[8]Here we shall assume that the dielectric constant ε' is the average of the one of the medium 1 and 2, nevertheless the choice is not unique.

interface layer, does not enter in the final results, therefore the amplitude of the harmonic field depends uniquely on the nature of the interface and, in this case, the coherence length that we have defined in the previous section is totally meaningless. In both cases the nonlinear response depends on the tensor shape. Nevertheless, while for the surface nonlinearity $\chi^{(2)}$ is determined by the interface geometry, in the case of the bulk the tensor it depends on the material considered.

1.4 Nonlinear coefficients

Conversion efficiency

In the previous example we have seen how to evaluate the amplitude of the second harmonic field inside a nonlinear medium. In practice, one can not measure this quantity but rather the intensity of the harmonic field generated outside the system. In the case of the harmonic generation it is useful to define the *conversion efficiency* which measures the amount of the pump field which is converted into the harmonic one. We can simply write

$$\eta_r = \frac{I^r_{\rm harm}}{I_{\rm pump}} \tag{1.34}$$

$$\eta_t = \frac{I^t_{\rm harm}}{I_{\rm pump}} \tag{1.35}$$

where $I_{\rm harm}$ and $I_{\rm pump}$ are the intensities of the reflected or transmitted harmonic and pump fields, respectively. This definition is completely general and it holds also in the case of third harmonic generation. It is worth to underline that, since the intensity of the n-th harmonic field is a function of the n-th power of the pump field, η does not simply depend on the characteristics of the system, but even on the pump field intensity. For this reason it is useful to introduce two other quantities, called *nonlinear reflectance* and *nonlinear transmittance*, which are defined as

Nonlinear coefficients

$$R^{\rm NL} = \frac{I^r_{\rm harm}}{(I_{\rm pump})^n} \tag{1.36}$$

$$T^{\rm NL} = \frac{I^t_{\rm harm}}{(I_{\rm pump})^n}. \tag{1.37}$$

We emphasize that these coefficients are not dimensionless and they have the dimension of the inverse of the (n-1)th power of the field intensity. It is straightforward to relate the conversion efficiency to the nonlinear transmittance

$$\eta_t = T^{\rm NL}(I_{pump})^{n-1} \tag{1.38}$$

In presenting our results we prefer using nonlinear reflectance and transmittance, since they are only a function of the system properties, and they are independent of the pump field intensity.

Chapter 2

Second Harmonic Generation in a Doubly Resonant Microcavity

The possibility of exploited nonlinear effects, such as harmonic generation, in integrated optical devices, requires the capability of achieving high conversion efficiency in micrometer scale devices. Semiconductors are among the best candidates because of their high nonlinearity and the high degree of control of the growth process technology. Unfortunately frequency conversion in cubic materials like GaAs or AlGaAs is limited by the difficulty of achieving phase-matching which is instead easily obtained in birefringent nonlinear materials. Even amorphous silicon nitride (a-$Si_{1-x}N_x$:H) is a suitable system for generating second harmonic generation, and in particular in the visible range due to is large band gap. In this system surface second order nonlinearity arise at the interface between layers with a different silicon concentration due to breaking of symmetry.

In this chapter we discuss the possibility to design a microcavity in order to achieve a great enhancement of second harmonic generation (SHG) in the case of bulk and surface nonlinearities. We demonstrate that the conversion efficiency is maximum when the structure is resonant for both the pump and harmonic frequencies, and phase matching is achieved. The design of a doubly resonant microcavity is difficult because of refractive index dispersion. In order to achieve double resonance, it is necessary to provide a design of DBR characterized by high reflectivity at the pump and harmonic frequencies, and furthermore to determine the appropriate cavity layer length.

In Secs. 2.1 and 2.2 the problem of design a doubly resonant microcavity in presence of non-birefringent dispersive media is theoretically discussed. We present the concepts of photonic gap and defect mode maps, which rep-

resent the fundamental tools in the search for doubly resonant microcavity parameters. Even though the aim of the discussion is to provide an efficient design method for doubly resonant microcavity, most of results are general and can find application in the design of several one dimensional photonic structures.
A Theoretical study of SHG problem in doubly resonant microcavities with dielectric mirrors is presented in Sec. 2.3. Here the problem is analytically treated: starting from the fundamental work of Berger on SHG in monolithic cavities [14], we complete the discussion by providing simple expressions of the cavity enhancement factor in phase-matching and anti phase-matching cases in the limit of highly reflectance mirrors. These results show an exponential growth of SHG efficiency as a function of the number of periods in the mirrors. The exponential growth is maximum when double resonance as well as phase matching are simultaneously achieved.
Numerical results obtained with a nonlinear transfer matrix method are in substantial agreement with the analytical model. In Sec. 2.4 a preliminary study of GaAs DRM with Alox/AlGaAs periodic mirrors is done for a pump wavelength of $2\mu m$. In Sec. 2.5 the problem of SHG is widely discussed in the case of a AlGaAs cavity, when the pump can be tuned at the more convenient wavelength of $1.550\mu m$ and higher enhancement can be achieved. Here localized phase-matching and anti-phase matching concepts and their roles in harmonic generation process are presented in detailed.
A collaboration with the research groups of F. Giorgis in Torino and S. Lettieri in Napoli has offered the opportunity of studying second harmonic generation in doubly resonant microcavities based on amorphous silicon nitride. We design a DRM that has been growth in Torino and whose linear properties have been characterized in Pavia, finally SHG measurements were performed in Napoli. This work led to the non obvious conclusion that even in the case of surface nonlinearity, enhancement of SHG can be obtained using doubly resonant systems. All these results are presented in Sec. 2.6.
In Sec. 2.7 some considerations on Kerr effect in doubly resonant cavities are presented. Here we want to justify the approximation adopted in all SHG calculation in which higher order nonlinear effects have been neglected.

2.1 Dual wavelength dielectric mirrors

The possibility of designing a doubly-resonant structure, in order to enhance SHG process, depends on the capability of growing dual-wavelength dielectric mirrors (DWDM) characterized by two stop-bands, at the pump and harmonic frequencies. In this case, one has to depart from the usual $\lambda/4$ condition for which no stop-band is present for the harmonic field, and to look for a more general design. Different approaches are possible: op-

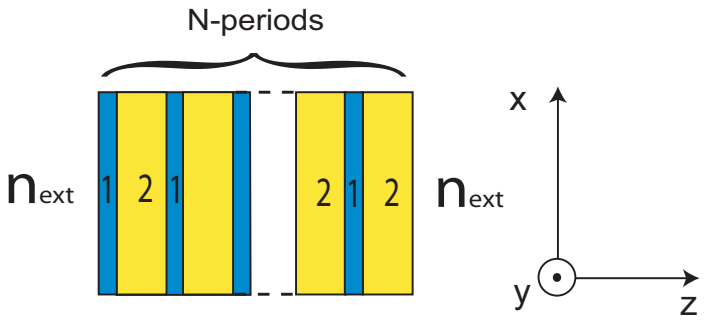

Figure 2.1: Scheme of a distributed Bragg reflector. (DBR)

timizing the performances of the mirrors by building them layer-by-layer in a non periodic structure [15], or working with non-$\lambda/4$ periodic mirrors [14, 16, 54]. Here we assume to work only with periodic distributed Bragg reflector (DBR) formed by the repetition of a bilayer period as sketched in Fig. 2.1. The equivalent infinite system is an ideal onedimensional 1DPC, characterized by a periodic dielectric function along the z direction. The so- ***Gap map***
lution of the Helmholtz equation for the electromagnetic field can be reduced to an eigenvalue problem, where the field is described by Bloch functions and the eigenvalues represent the energies allowed to the propagating modes. In perfect analogy with the electronic problem in a crystal, the eigenvalues can be organized in a photonic band structure [55]. The dispersion relations $\omega = \omega(k)$ for the propagating modes are found by the transfer-matrix method and Bloch-Floquet theorem in the form of an implicit equation that is the optical analogue of the Kronig-Penny model[56]:

$$\begin{aligned} \cos(q\Lambda) &= \cos(k_{1,z}L_1)\cos(k_{2,z}L_2) \\ &- \frac{1}{2}\left(\frac{\alpha_1}{\alpha_2}+\frac{\alpha_2}{\alpha_1}\right)\sin(k_{1,z}L_1)\sin(k_{2,z}L_2), \end{aligned} \tag{2.1}$$

where $\Lambda = L_1 + L_2$ is the DBR period, q is the Bloch vector, L_1 and L_2 are the layer widths (see Fig. 2.2a), $k_{i,z} = (\omega/c)n_i\cos\theta_i$, $i = 1, 2$ are the z-components of the wave vectors in the layers, $n_i = n_i(\omega)$ are the refractive indices including material dispersion, while θ_i depends on the incident angle θ and the external refractive index n_{ext} through Snell's law $\theta_i = \arcsin\{(n_{\text{ext}}/n_i)\sin\theta\}$. Since we work at a finite incidence angle we have to distinguish between transverse electric (TE or s-polarized) and transverse magnetic (TM or p-polarized) modes, with the following expres-

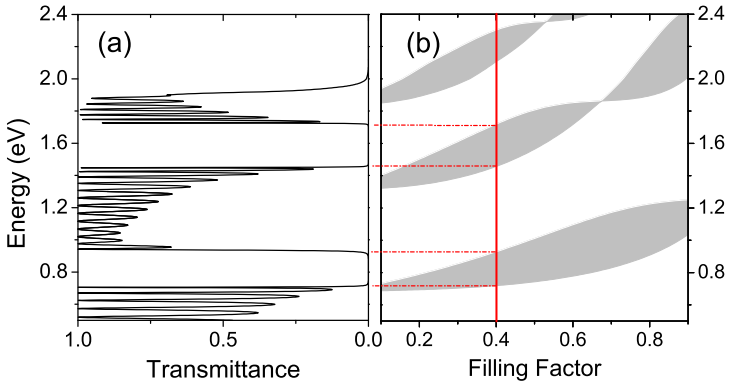

Figure 2.2: (a) Linear transmittance for a DBR consisting of Alox (material 1) and $Al_{0.4}Ga_{0.6}$ (material 2) with period $\Lambda \equiv L_1 + L_2$=292 nm and filling factor $f = L_1/(L_1 + L_2) = 0.4$ All the calculations are performed assuming incidence angle $\theta = 30^\circ$ and p-polarized electric field.(b) Gap map as a function of the filling factor.

sions for the factors α_i of Eq.(2.1):

$$\left.\begin{aligned}\alpha_1 &= n_2 \cos\theta_1 \\ \alpha_2 &= n_1 \cos\theta_2\end{aligned}\right\} \quad \text{TM modes,}$$

$$\left.\begin{aligned}\alpha_1 &= n_1 \cos\theta_1 \\ \alpha_2 &= n_2 \cos\theta_2\end{aligned}\right\} \quad \text{TE modes.}$$

A notable feature of the formalism is that the material dispersion of the refractive indices can be easily taken into account. In the following examples we shall use the material dispersion of GaAs, AlAs and of the $Al_xGa_{1-x}As$ alloy as reported in the literature [57]. As in the case of the Kronig-Penney model we find forbidden frequency intervals or *photonic gaps*, for which the Bloch vector is completely imaginary, corresponding to non-propagating electromagnetic modes. Solving numerically Eq.(2.1) we can easily provide a map of the position of the gaps by varying the DBR parameters or the incidence angle. We show an example in Fig. 2.2b, where the gap position of a DBR made of oxidized AlAs (or Alox, layer 1) and $Al_{0.4}Ga_{0.6}As$ (layer 2) is plotted as a function of the filling factor $f = L_1/\Lambda$ with $\Lambda = 292\,\text{nm}$, for an

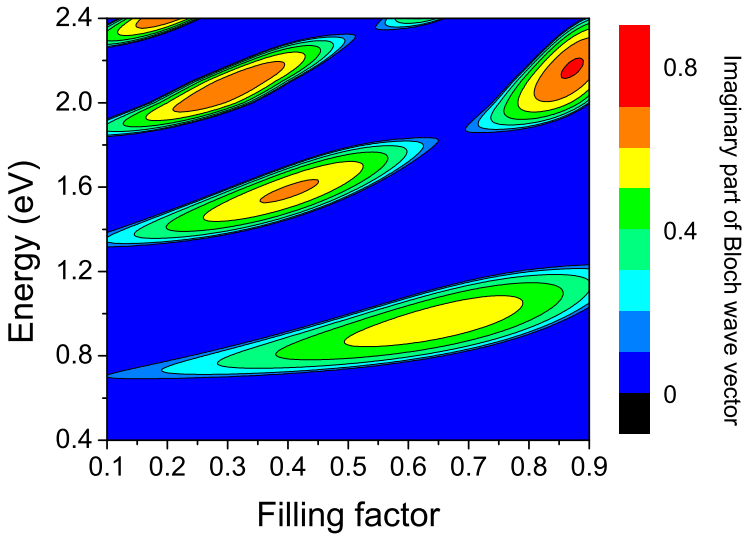

Figure 2.3: Imaginary part of the Bloch wave-vector as a function of the filling factor. for a 1DPC consisting of Alox (material 1) and $Al_{0.4}Ga_{0.6}$ (material 2) with period $\Lambda \equiv L_1 + L_2$=292 nm All the calculations are performed assuming incidence angle $\theta = 30°$ and p-polarized electric field

incidence angle $\theta = 30°$ and p-polarization. In the figure 2.2a we report the linear transmittance of the DBR corresponding to the filling factor $f = 0.4$, note that the stop-bands of the finite structure correspond to the gaps of the equivalent 1DPC.When the $\lambda/4$ condition is fulfilled, the first-order gap has a maximum width while the second-order gap vanishes: the corresponding filling factor will be called $f \equiv f_{\lambda/4}$. Under this condition, the reflectance at the center of the first-order stop band is also maximum. The gap maps available in the literature are usually reported in dimensionless units, since they are calculated for fixed values of the dielectric constant and they are scalable with the period of the photonic lattice [55]. Here the gap positions are reported in energy units because our goal is to study the relative positions of the photonic gaps at ω and 2ω, hence the material dispersion cannot be neglected and the gap maps are not scalable. Within the gap, Eq. (2.1) can be solved only for an imaginary Bloch vector which indicates an exponential decay of the electric field in the DBR. This decay is strictly related to the mirror reflectivity of a finite structure, which scales exponentially with

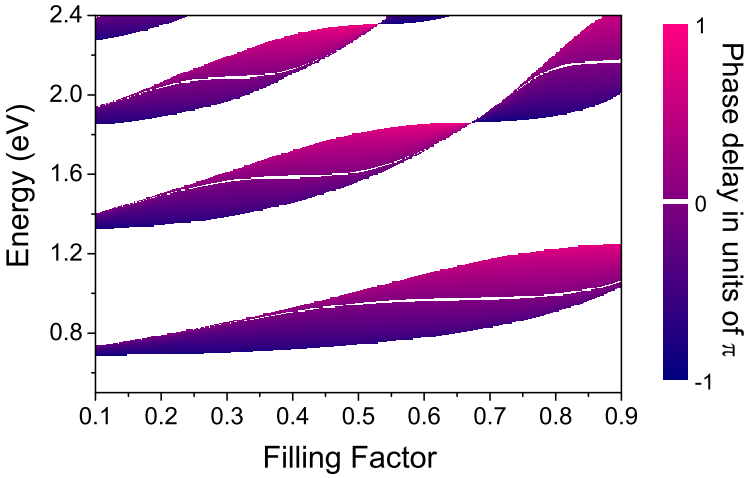

Figure 2.4: Reflectance phase delay as a function of the filling factor. for a 1DPC consisting of Alox (material 1) and $Al_{0.4}Ga_{0.6}$ (material 2) with period $\Lambda \equiv L_1 + L_2$=292 nm All the calculations are performed assuming incidence angle $\theta = 30°$ and p-polarized electric field

the number of periods. Thus, the dielectric mirrors offer the advantage of great flexibility and the possibility of tuning the reflectance by varying the number N of periods in the multilayer. It is possible to provide a map of the imaginary part of the wave vector as a function of filling factor. In Fig. 2.3 this map has been evaluated for the example just described above. Even if this study can give many informations about the reflectivity of the mirrors and therefore about the quality factor (Q-factor) of the final microcavity, the reader must remember that the Q-factor does not depend only on the imaginary part of the wave vector, but also on the refractive index contrast between the cavity layer and the adjacent mirrors layers. Therefore, this map can not be considered any sort of "Q-map" nevertheless, it describes its exponential growth as a function of the number N of periods in the mirrors, as it will be clarified later.

Phase delay

A remarkable difference between dielectric and metallic mirrors is the phase change of the field associated to reflection. Indeed, while in a metallic mirror the phase of the field changes only of multiples of π, dielectric mirrors

are characterized by a complex reflection coefficient

$$r = \sqrt{R}e^{\imath\phi}, \tag{2.2}$$

where $R = |r^2|$ is the mirror reflectance, while ϕ is the reflection phase which is, in general, a complicated function of the mirror structure, of the incident external medium refractive index n_{ext}, and of the field polarization and frequency. In the case of periodic mirrors in the limit $R \simeq 1$ (*i.e.,* for sufficiently large N), it has been demonstrated by Apfel [58, 59] that the reflection phase delay within the stop-bands depends only on the period composition and external medium refractive index, but it is independent on N. Moreover the phase delays seen by two different external media of refractive index n_0 and n_c, respectively, are related by the simple equation

$$n_0 \tan\frac{\phi_0}{2} = n_c \tan\frac{\phi_c}{2} \tag{2.3}$$

In Fig. 2.4 we report the first example, to our knowledge, of a map of reflection phase delay as a function of filling factor. The phase is shown in a color scale within the photonic gaps where, for the case of finite N, the reflectance is close to unity. The results for the phase delay in reflection will play a crucial role for SHG problem, which will be discussed in Sec. 2.3

Material choice

Let us look for a DWDM whose first-order gap (for the pump beam) is centered around the convenient wavelength $\lambda = 1.55\,\mu$m. In Figs. 2.5a and 2.5b we plot the gap maps for two systems with weak and strong refractive index contrast, respectively. The energies of the second-order gap (for the harmonic beam) are divided by two in order to visualize better the filling factors for which two gaps occur simultaneously at ω and 2ω: the darkest regions in the plots correspond to their superposition. In both cases we consider p-polarized pump, s-polarized second harmonic beams and an angle of incidence $\theta = 30°$.

Figure 2.5a refers to the case of AlAs/GaAs mirrors with $\Lambda = 250$ nm. This material combination presents a low refractive index contrast, therefore the photonic gaps are quite small. Moreover, the relatively high dispersion in the energy range under consideration makes the harmonic gap to lie below the pump one. The combination of these features allows designing a periodic DWDM only for a narrow range of filling factors $0.63 < f < 0.83$, with a very small superposition region in energy.

In Fig. 2.5b we present the case of a Alox/$Al_{0.4}Ga_{0.6}As$ DBR with $\Lambda = 292$ nm. The harmonic gap is almost entirely contained in the pump one, hence a DWDM can be realized for any filling-factor values, except the one corresponding to the $\lambda/4$ condition for which no harmonic gap occurs. With a filling factor $f = 0.4$, which is the case indicated by arrows in Fig. 2.2a, the pump gap is centered around 0.8 eV ($\lambda = 1.55\,\mu$m). The situation presented in Fig. 2.5b is the most advantageous one, indeed the small

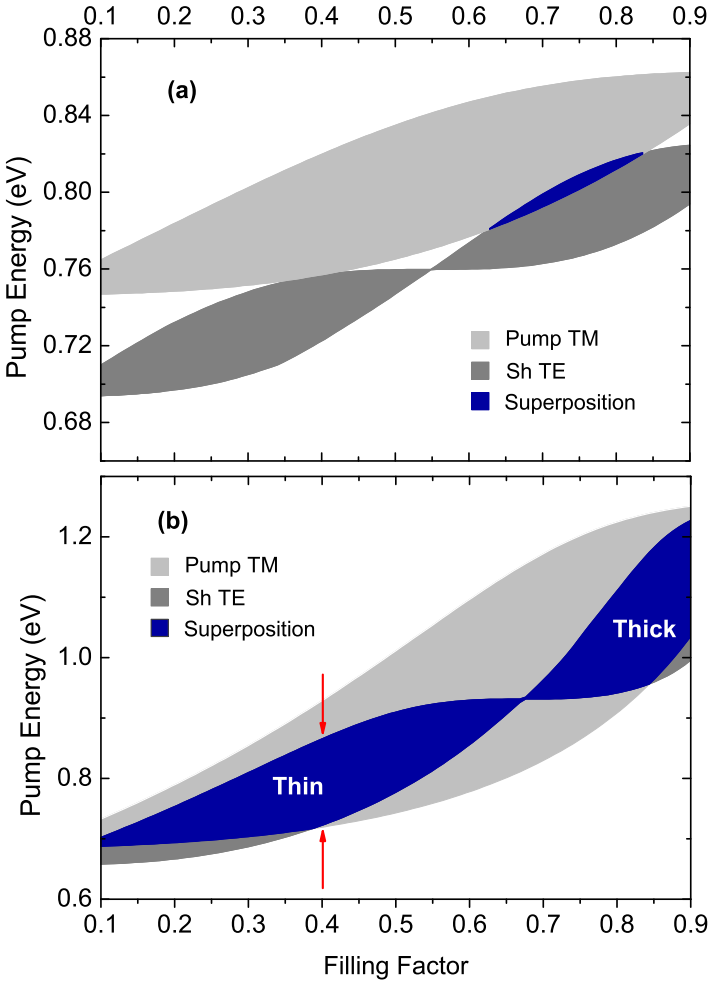

Figure 2.5: Gap maps as a function of filling factor in a low index contrast AlAs/GaAs DBR with $\Lambda = 250$ nm (a) and a high index contrast $Alox/Al_{0.4}Ga_{0.6}As$ DBR with $\Lambda = 292$ nm (b). The energies of the harmonic gaps are divided by two. In both cases we assume p-polarized pump, s-polarized harmonic and an incidence angle $\theta = 30°$.

material dispersion guarantees that the pump and harmonic gap centers are close to each other for any filling factor values, while the high refractive index contrast allows to achieve large gaps with a wide superposition region, and also to get high reflectance in the stop bands with a small number of DBR periods. The solution presented in Fig. 2.5b for a Alox/$Al_{0.4}Ga_{0.6}As$ DWDM centered at 0.8 eV is not unique, since the period Λ or the incidence angle can be tuned in order to center the pump and harmonic gaps at the desired energy. The structures with a pump gap centered at 0.8 eV will be thinner when f is small, therefore we speak of a *thin configuration* when $f < f_{\lambda/4}$ and a *thick configuration* in the opposite case $f > f_{\lambda/4}$. It will be clear in Sec. 2.3 that, in the case of a DRM, the choice of working in thin or thick configuration is not arbitrary. Indeed, as shown in Fig. 2.4b, these two configurations are characterized by a different reflection phase: this fact has important consequences in the phase matching of second harmonic generation process.

Using the gap map technique it is possible to design a dual-wavelength dielectric mirror taking into account the refractive index dispersion. It has been shown that periodic DBR structures cannot be usefully employed in the case of low index contrast, highly dispersive material combinations like AlAs/GaAs. For these materials, non-periodic structures like those of Ref. [15] may remain the best solution for the realization of DWDMs. In the more favorable case of high index contrast DBRs like Alox/$Al_{0.4}Ga_{0.6}As$, the superposition region between pump and harmonic gaps is sufficiently large to have a robust DWDM structure which can be tuned by changing either the DBR period (in the design) or the incidence angle (in the experiment). In the following Section we discuss how such a DWDM can be used to achieve double resonance in a microcavity structure.

2.2 Doubly-Resonant Microcavity

The possibility to obtain doubly-resonant microcavities has been already investigated for pseudo-metallic mirrors at normal incidence [14] or for non-periodic mirrors [15]. With metallic or pseudo-metallic mirrors the phase delay in reflection is $\phi = 0$ or π and therefore the position of the resonances depends exclusively on the cavity length, L_c. The index dispersion of the cavity material may be compensated by taking L_c to be equal to the coherence length [14]. Moreover, the temperature-dependence of the refractive index is taken as an experimental tuning parameter. On the other hand, for non-periodic dielectric mirrors, the cavity length is of the order of the wavelength of light and the angle of incidence is used as a tuning parameter [15]. The disadvantage of non-periodic mirrors is that the structure is very sensitive to small deviations in the layer thicknesses, and also it is not easy to derive clear trends for the Q-factors and the conversion efficiency as a

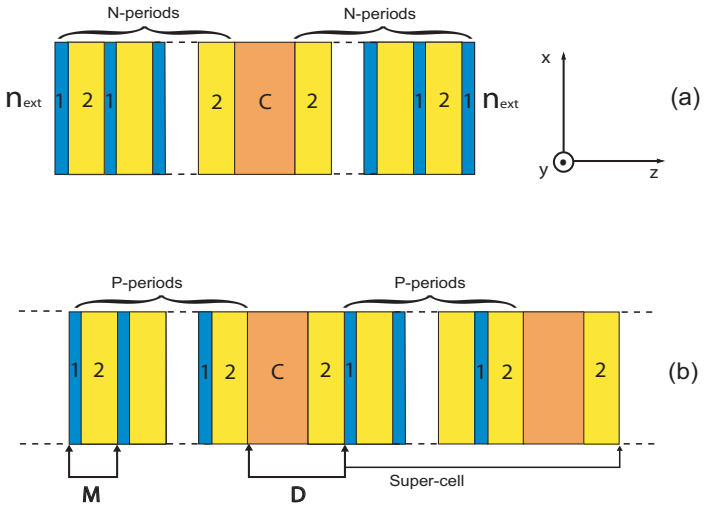

Figure 2.6: Scheme of a doubly-resonant microcavity (a) and the corresponding ideal periodic system (b).

function of structure length.

In this Section we investigate the possibility of realizing a microcavity with two resonances centered at ω and 2ω, even in the presence of dispersive materials. The idea is to employ periodic DWDM with high refractive index contrast and to use the angle of incidence as a fine-tuning parameter. We consider a microcavity composed by a layer of width L_c embedded between two identical mirrors characterized by a complex reflection coefficient $r(\omega) = \sqrt{R(\omega)}\exp[\imath\phi(\omega)]$. The linear transmittance is

$$T(\omega) = \frac{(1-R(\omega))^2}{1+R(\omega)^2 - 2R(\omega)\cos\delta(\omega)} \tag{2.4}$$

with

$$\delta(\omega) = 2k_{c,z}(\omega)L_c + 2\phi(\omega), \tag{2.5}$$

where $k_{c,z} = (\omega/c)n_c\cos\theta_c$ is the z component of the wave vector, n_c is the refractive index in the cavity layer and θ_c is found again by Snell's law. The system is resonant at specific frequencies ω_m when $\delta(\omega_m)$ is a multiple of 2π [14]. The phase change $\phi(\omega)$ of a DBR is strongly dependent on frequency [58–63], thus the resonance position of the cavity mode inside the stop band is a complicated function of the structure parameters and of the incidence angle. Analytic expressions for the resonance position are available only when the cavity mode is close to the center of the stop band [62], where $\phi(\omega)$ can be approximated by a linear function of frequency.

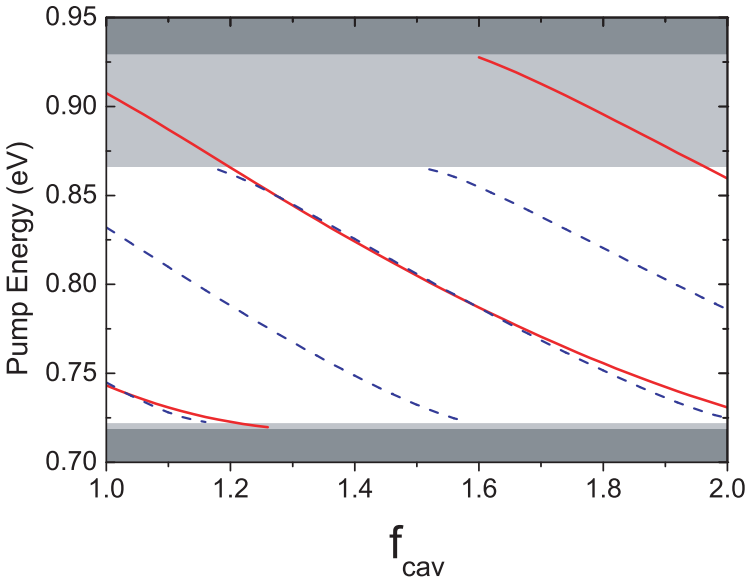

Figure 2.7: Position of p-polarized pump (solid lines) and s-polarized harmonic (dashed lines) defect modes inside their respective gaps as a function of $f_{\rm cav} = L_c/\Lambda$. *The mirror is composed by* $P = 20$ *periods of alternating* $L_1 = 116.8$ *nm (Alox) and* $L_2 = 175.2$ *nm (*$Al_{0.4}Ga_{0.6}As$*) layers, with* $\Lambda = 292$ *nm; the incidence angle* $\theta = 30°$. *Harmonic energies are divided by two. The white region indicates an harmonic gap superimposed to the pump one (light grey), while the darkest zone indicate the absence of a gap.*

Once a DWDM at the working frequency regions is designed (i.e., Λ, f and θ are known), the DRM is obtained by introducing a defect with length L_c in the periodic structure, as shown in Fig. 2.6a. We consider an equivalent infinite periodic system constituted by the repetition of a super-cell composed by $P + 1/2$ periods of the DWDM and by the defect, as shown in Fig. 2.6b. The presence of periodically repeated defects in the 1DPC structure introduces localized states in the photonic band gaps [1]. The problem of finding the desired cavity width for double resonance can be solved as follows. If we consider the transfer matrix $\mathbf{M}$ of a single mirror period and the transfer matrix $\mathbf{D}$ of the bilayer L_c/L_2 (see Fig. 2.6b), then the transfer matrix $\mathbf{T}$ of the super-cell is given by

$$\mathbf{T} = \mathbf{D}\mathbf{M}^P. \tag{2.6}$$

By indicating with $\mathbf{E_0}$ and $\mathbf{E_{\Lambda_s}}$ the electric field vector at the beginning and

[1] The number P of periods in the equivalent infinite systems should be large enough to avoid coupling between the different defect layers.

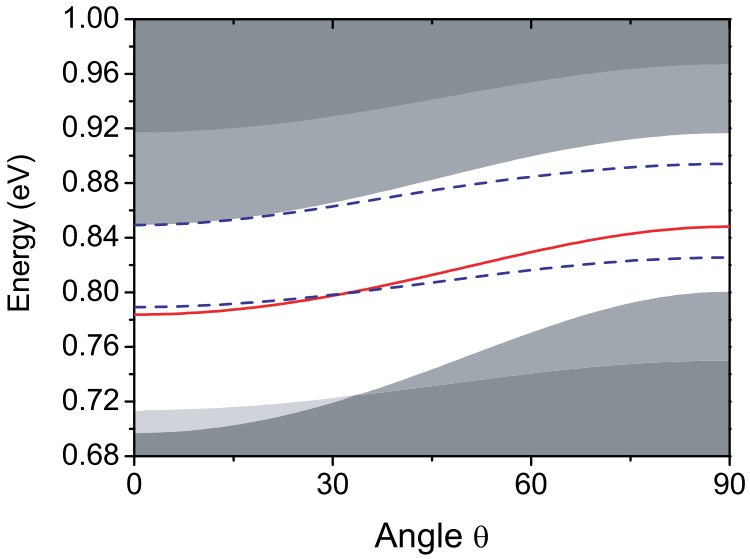

Figure 2.8: Position of p-polarized pump (solid lines) and s-polarized harmonic (dashed lines) defect modes inside their respective gaps as a function of incidence angle θ. The mirror is composed by $P = 20$ periods of alternating $L_1 = 116.8$ nm (Alox) and $L_2 = 175.2$ nm ($Al_{0.4}Ga_{0.6}As$) layers, with $\Lambda = 292$ nm; $L_c = 449.7$nm.. Harmonic energies are divided by two. The white region indicates an harmonic gap (light grey) superimposed to the pump one (grey), while the darkest zone indicate the absence of a gap.

at the end of a single super-cell, discrete translational symmetry implies that

$$\mathbf{E}_{\mathbf{\Lambda_s}} = e^{\imath q_s \Lambda_s} \mathbf{E_0}, \tag{2.7}$$

where $\Lambda_s = P\Lambda + L_2 + L_c$ is the super-cell length and q_s is the Bloch vector. Thus it follows that $\exp(\pm \imath q_s \Lambda_s)$ are the eigenvalues of $\mathbf{T}$ and therefore

$$\mathtt{Tr}(\mathbf{T}) = 2\cos(q_s \Lambda_s). \tag{2.8}$$

Defect map

This equation is the generalization of Eq.(2.1) and it contains implicitly the dispersion relation of the photonic system described above. In perfect analogy with the strategy we used in Sec. 2.1, it is possible to provide a *defect map*, i.e., the positions of defect modes inside the gap can be evaluated as a function of the cavity length L_c or the incidence angle θ.

In Fig. 2.7 we show an example of a defect map, where the defect positions are plotted as a function of $f_{cav} = L_c/\Lambda$ [64]. As the thickness of the cavity layer increases, the defect modes move across the gap but with different slopes because of the material dispersion. For a wide range of f_{cav}

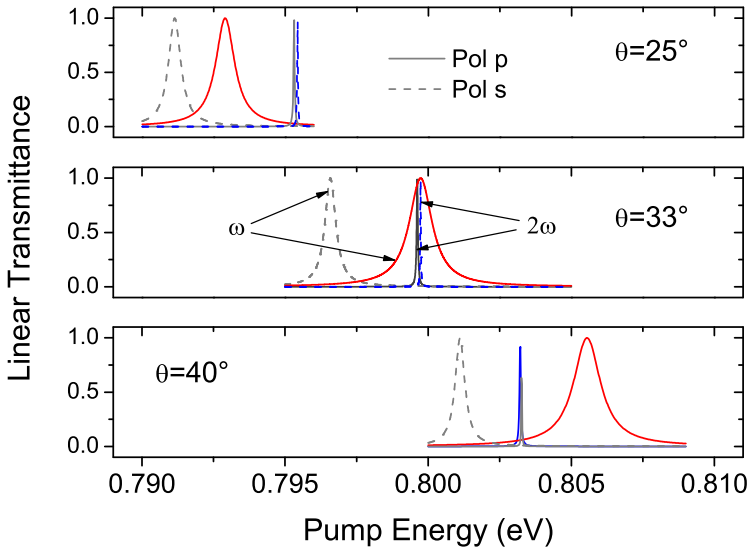

Figure 2.9: Tuning of the resonance positions by changing the incidence angle in a DRM: linear transmittance for p (solid) and s (dashed lines) polarizations for the pump and harmonic fields at $\theta = 25°, 33°$ and $40°$. Structure parameters: $L_1 = 116.8$ nm (Alox), $L_2 = 175.2$ nm ($Al_{0.4}Ga_{0.6}As$) and $L_c = 449.7$ nm ($Al_{0.25}Ga_{0.75}As$), with $N = 6$ periods in the DBRs. Double resonance occurs at $\theta = 33°$.

values we find that the p-polarized defect mode is close to the s-polarized harmonic one. The small difference could be compensated by changing the angle of incidence. Here we choose the parameters in such a way that the double-resonance condition occurs close to the center of the stop bands, where the Q-factor of the cavity modes is largest.

Analogously, in Fig. 2.8 we report a defect map as a function of the incidence angle θ. This parameter affects strongly linear and nonlinear properties of the structure, in particular the gap and defect mode positions. Another crucial quantity which characterize the microcavity is its quality factor, which depends on the mirror reflectance that depends on the field polarization and the incidence angle. In the design of microcavity structures we chose to fulfill the double-resonance condition at a finite θ and for different polarizations of the pump and harmonic waves. In Fig. 2.9 we show the linear transmittance of a DRM for the pump and harmonic fields

Resonance angle tuning

in both s and p polarizations. The harmonic energies were divided by two in order to visualize better the occurrence of a double resonance. Because of the polarization splitting of cavity modes, four resonances (two at ω and two at 2ω) are present. When the angle grows from $\theta = 25°$ to $\theta = 40°$, the resonances shift towards higher energies, and at $\theta = 33°$ the p-polarized pump resonance overlaps the s-polarized harmonic one.

The power of the incidence angle as a tuning parameter depends on the strength of the polarization splitting [62, 65]. A careful study of this problem, conducted through the defect-map method, has shown that the polarization splitting is extremely sensitive to the DBR parameters. In particular, the splitting is larger for a high refractive index contrast and when f is far from $f_{\lambda/4}$. In actual experiments, besides the incidence angle, the thickness variation of the epitaxial structure due to growth inhomogeneity could also be used to adjust the energy position of the double resonance.

As a general remark in closing this Section, the gap- and defect-map methods represent an efficient tool for the design of microcavity structures. Moreover this method can be applied even working at normal incidence when other resonance tuning parameters (e.g. temperature) can be used. Since the results are not scalable when material dispersion is considered, the design should be studied for each specific case. In the following we give examples of microcavities that are optimized for efficient SHG at double resonance.

2.3 Theory of Second Harmonic Generation in Doubly Resonant Microcavities

In this Section we analyze the results for second-harmonic generation (SHG) in a doubly resonant microcavity and in the case of bulk nonlinearity and when pump delpletion can be neglected. This assumption allows to divide the SHG process in three independent steps: (i) linear propagation of the pump field, (ii) generation of a nonlinear polarization and of a source field at the harmonic frequency, (iii) propagation of the second-harmonic field along the structure. We show that in DRM all these aspects can be optimized simultaneously and a great enhancement of the nonlinear conversion may be achieved.

Cavity enhancement factor

The second harmonic generated by the DRM can be compared to the one by the isolated cavity layer (or single-pass conversion). The ratio between the nonlinear transmittance of the cavity $T_{\rm cav}^{NL}$ and the one of the correspondent single layer $T_{\rm layer}^{NL}$ represents the enhancement due to the resonant cavity. Berger [14] has given an analytic expression for the cavity

enhancement factor η of a symmetric structure:

$$\eta = \left| \frac{T_\omega \sqrt{T_{2\omega}} \{1 + R_\omega \sqrt{R_{2\omega}} \exp(\imath \delta_{\mathrm{m}})\}}{\{1 - R_\omega \exp(\imath \delta_\omega)\}^2 \{1 - R_{2\omega} \exp(\imath \delta_{2\omega})\}} \right|^2, \tag{2.9}$$

where $\delta_\omega = \delta(\omega)$ and $\delta_{2\omega} = \delta(2\omega)$ have been already specified in Eq. (2.5), while

$$\delta_{\mathrm{m}} = \phi_{j,\omega} + \phi_{k,\omega} + 2k_{z,\omega} L + \phi_{i,2\omega} + k_{z,2\omega} L, \tag{2.10}$$

where i, j, k are the cartesian components coupled by the nonlinear susceptibility $\chi^{(2)}_{ijk}$. The factor δ_m describes the phase mismatch between the nonlinear polarization P^{NL} and the free harmonic field.

From Eq. (2.9) we observe that the cavity enhancement of SHG depends on the terms in curly brackets, which describe the effects of pump and harmonic field distributions (in the denominators) and of their phase mismatch (in the numerator). When a resonance at ω and 2ω occurs, the denominators of the expression (2.9) tend to vanish: this is the signature of a double-resonance condition. However, the SHG efficiency is enhanced only when the quantity $\delta_m \neq \pi\,[2\pi]$, otherwise the numerator also tends to vanish and the efficiency is reduced. The cavity enhancement is maximum when all the factors δ_ω, $\delta_{2\omega}$ and δ_m are multiple of 2π. Starting by the relation (2.5) and (2.10), it is easy to demonstrate that, in a *symmetric* cavity with double resonance, δ_m must be an integer multiple of π: the two situations that can occur are analyzed below.

When $\delta_m = 2n\pi$, which we call a *phase matching condition*, the nonlinear polarization is in phase with the harmonic field. For high reflectance mirrors we get

$$\eta_{\mathrm{pm}} \simeq \frac{4}{(1 - R_\omega)^2 (1 - R_{2\omega})} \propto Q_\omega^2 Q_{2\omega}. \tag{2.11}$$

PM case

In this situation all aspects of the harmonic generation process are optimized, and the cavity enhancement of SHG grows with the Q-factors at ω and 2ω.

When $\delta_m = (2n+1)\pi$, which is called *anti-phase matching condition*, the nonlinear polarization P^{NL} in the cavity layer is exactly out of phase with respect to the free harmonic field. This means that the coupling between the nonlinear polarization and the free harmonic field is weak, yielding a low extraction efficiency. Again we look at the $R_{\omega,2\omega} \to 1$ limit and obtain:

$$\eta_{\mathrm{apm}} \simeq \frac{(1 - R_\omega + \frac{1}{2}(1 - R_{2\omega}))^2}{(1 - R_\omega)^2 (1 - R_{2\omega})}. \tag{2.12}$$

APM case

Here we observe that there are two types of behavior according to the rapidity with which R_ω and $R_{2\omega}$ tend to unit. In particular we obtain:

$$\eta_{\mathrm{apm}} \simeq \frac{1 - R_{2\omega}}{4(1 - R_\omega)^2} \propto \frac{Q_\omega^2}{Q_{2\omega}} \tag{2.13}$$

when $\frac{1-R_\omega}{1-R_{2\omega}} \to 0$, and

$$\eta_{\rm apm} \simeq \frac{1}{(1-R_{2\omega})} \propto Q_{2\omega} \tag{2.14}$$

when $\frac{1-R_\omega}{1-R_{2\omega}} \to \infty$. This result shows that, in the case of anti-phase matching, the enhancement of SHG is much smaller than in the phase-matched situation.

The expressions (2.11), (2.13)-(2.14) can be compared with the enhancement factor of a single-resonant microcavity. We treat only the case of a resonance at the pump frequency ω. The cavity enhancement can be expressed as

SRM case

$$\eta_{\rm SRM} = \frac{1}{(1-R_\omega)^2} T_{2\omega} M_\omega \propto Q_\omega^2, \tag{2.15}$$

where $M(\omega)$ is a function describing the mismatch between the nonlinear polarization and the harmonic field. In general, since $T_{2\omega}$ and M do not present any resonance, pump field confinement is the only relevant effect.

The cavity enhancement factor is a function of mirror reflectance at ω and 2ω and therefore of the number N of periods in the DBRs. It is useful to express the Q-factors as $Q \propto \exp(2N\kappa\Lambda)$, where κ is the imaginary part of the Bloch vector in the photonic gap. From expressions (2.11), (2.13)-(2.15) we can derive the trend of the cavity enhancement as a function of N:

$$\eta_{\rm DRM,pm} \propto \exp[2N(2\kappa_\omega + \kappa_{2\omega})\Lambda] \tag{2.16}$$

$$\eta_{\rm DRM,apm} \propto \begin{cases} \exp[2N(2\kappa_\omega - \kappa_{2\omega})\Lambda], & \kappa_\omega \geq \kappa_{2\omega} \\ \exp[2N(\kappa_{2\omega})\Lambda], & \kappa_\omega < \kappa_{2\omega}, \end{cases} \tag{2.17}$$

$$\eta_{\rm SRM} \propto \exp[4N\kappa_\omega], \tag{2.18}$$

The conversion efficiency η is largest in the phase matched DRM when

$$Q_{\omega,\rm DRM}^2 Q_{2\omega,\rm DRM} > Q_{\omega,\rm SRM}^2 \tag{2.19}$$

and the exponential growth with the number of period is faster when

$$2\kappa_\omega^{DRM} + \kappa_{2\omega}^{DRM} > 2\kappa_\omega^{SRM}. \tag{2.20}$$

This condition can be fulfilled by proper structure design, as illustrated below. The Q-factors of the resonances depend also on the refractive index of the cavity medium and on which way the DBR is truncated near the cavity. The expression above refers to the case of equivalent microcavities in the sense that both have the same number of periods, the mirrors have the same composition, and they are truncated in the same way.

In expression (2.9) we have implicitly considered the case in which the generated second harmonic has a specific polarization and, in particular, that only one element $\chi^{(2)}_{ijk}$ of the nonlinear susceptibility is involved in the process. In general, for specific in/out polarization configurations, more than one tensor component is involved and the phase-matched one (if any) will be dominating. Also, Eq. (2.9) is derived by assuming that only the cavity layer be nonlinear. Thus Eq. (2.9) should be viewed as a useful guide for the design of microcavities with high SHG efficiency, but it cannot replace the numerical calculations which are presented below.

Although it is not possible to provide a general rule which tells *a priori* which DRMs are characterized by phase matching for a specific $\chi^{(2)}$ configuration, the DRMs can be divided in two classes, namely *thick* and *thin*, which depend on the DWDM used. We observe that, in general, these two classes are characterized by complementary behavior of δ_m. This fact is a consequence of the different phase delay which we have in thick and thin configuration at 2ω, in particular by looking at Fig. 2.4 we can notice that the phase delay changes by π when $f_{\lambda/4}$ is crossed. In the following we discuss examples of doubly-resonant microcavities for *p-s* and *s-p* nonlinear conversion where thick and thin mirror configuration are assumed.

In the following section we present a systematic study of DRM with GaAs or AlGaAs cavity layers and Alox/AlGaAs dielectric mirrors. All the results are presented with a chronological order, from the first designed and studied DRM, composed by a layer of GaAs embedded between two periodic mirrors in thick configuration, to the last structure, designed in order to work at pump wavelelngth equal $1.550\mu m$ in *s-p* configuration, for which the cavity enhancement is maximum. Numerical calculations presented in Secs. 2.4 and 2.5 are performed using nonlinear transfer matrix method [52] (see appendix A) with the measured nonlinear susceptibilities of the $Al_xGa_{1-x}As$ alloy [66] and are valid in the limit of negligible pump depletion.

2.4 GaAs cavity with AlGaAs/Alox dielectric mirrors

GaAs cavity

The goal is to demonstrate the possibility of designing a DRM with non-birefringent dispersive media. The choice of GaAs as a cavity layer is motivated by its high nonlinearity, nevertheless it forces to work with a pump wavelength larger than 1.8μ in order to avoid SH signal absorption, which starts at $0.9\mu m$.

The following results refer to single and double resonant microcavities with a GaAs cavity layer and with DBRs constituted of alternate layers of $Al_{0.4}Ga_{0.6}As$ (layer 1) and Alox (oxidized AlAs, layer 2). The field components coupled by the $\chi^{(2)}$ tensor depend on the growth direction of the sample as dis-

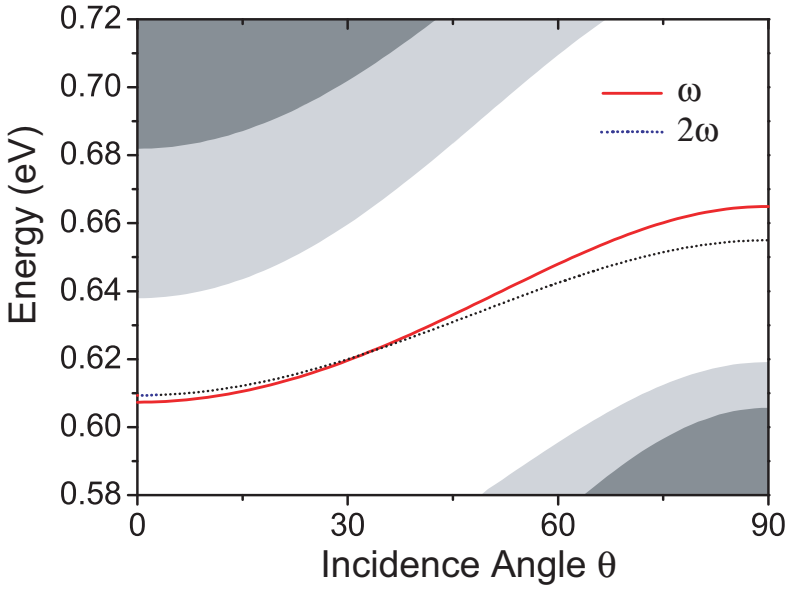

Figure 2.10: Energies of p-polarized pump (solid) and s-polarized SH defect modes in the stop bands (dotted) as a function of the angle of incidence. The dark and light grey areas denote the regions outside the stop band for the pump and SH wave, respectively. Parameters are given in the text.

cussed in Chapter 1. We have considered two different orientations of the nonlinear GaAs layer: [111] (with plane of incidence $[1\bar{1}0]$) and [001] (with plane of incidence [010]), the non-vanishing $\chi^{(2)}$ are reported in Fig. 2.13. In all calculations we take into account the refractive index dispersion of the materials.[57].

The design of a DRM structure is made for a pump wavelength $\lambda = 2\mu$m using the method presented in Secs. 2.1 and 2.2. We optimize the thicknesses L_1, L_2 of the DBR layers in order to obtain first- and second-order stop bands (or photonic gaps) of comparable size, working in thick configuration.[14] Moreover, we choose the cavity layer thickness in such a way that the defect modes are resonant with the pump and harmonic waves at a finite angle of incidence. The following parameters are obtained: $L_1 = 104.8$ nm, $L_2 = 408.9$ nm, $L_c = 675$ nm. Figure 2.10 shows the angular dispersion of the defect modes at ω and 2ω, the latter being divided by two in order to visualize the double-resonance condition. The two defect modes are seen to cross at an angle of incidence around $\theta = 30°$.

We now calculate numerically the SH conversion efficiency by the nonlinear transfer matrix method.[52] The nonlinear transmittance T^{NL} normal-

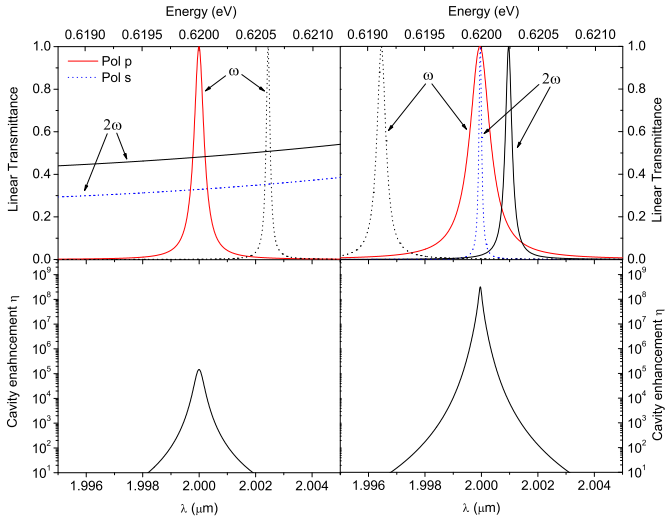

Figure 2.11: Linear and nonlinear transmittance versus pump wavelength for a single-resonant (left) and doubly-resonant microcavity (right) with $N = 6$ periods, at $\theta = 30°$. The SH calculation assumes a [111] orientation and p-s conversion.

ized to that of an isolated cavity layer directly yields the cavity enhancement η. In Fig.2.11 we compare the linear and nonlinear transmittance of SRM and DRM with [111] orientation. While in the first case the structure is designed to obtain only a pump resonance ($\lambda/4$ DBRs and no gap at 2ω), in the DRM all aspects of harmonic generation are optimized. In fact, in the DRM we have at the same time pump field confinement, good extraction efficiency of the SH, and phase matching between the two waves. Notice that the cavity modes at 2ω are shifted towards lower energies with respect to the pump by the material dispersion and that double resonance for p-s SH conversion is achieved by taking advantage of the polarization splitting since we are working at finite incidence angles. As we shall see in Sec. 2.5 linear transmittance does not provide any information on the phase of the nonlinear polarization relative to the harmonic field. Here we can certainly affirm that we are in phase matching condition, by looking at the great enhancement in SHG associated to double resonance. This is confirmed by the results shown in Fig. 2.12, where cavity enhancement peak value is plotted versus the number N of period in the DBR. As we have seen in previous section, in all cases T^{NL} depends exponentially on N through the Q-factors: $T^{NL} \propto Q_\omega^2 Q_{2\omega}$ for a DRM with phase matching, $T^{NL} \propto Q_\omega^2 / Q_{2\omega}$ for a

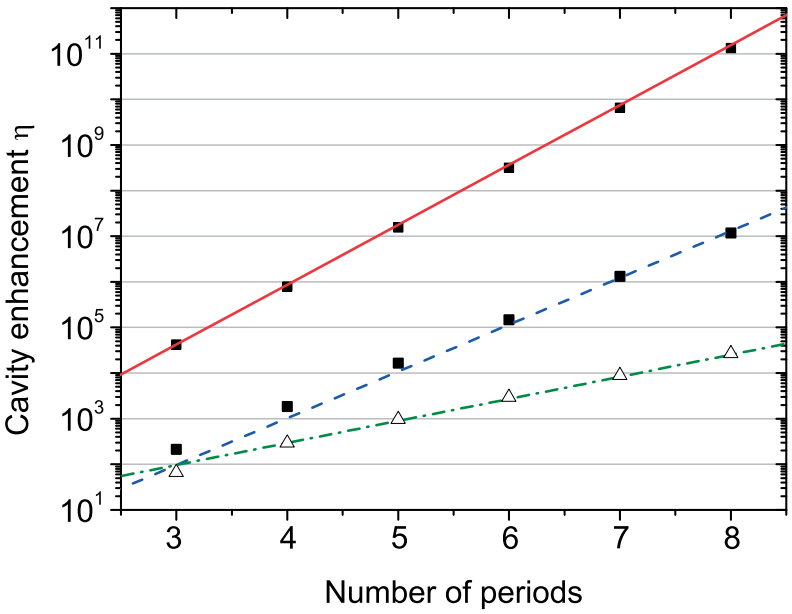

Figure 2.12: Nonlinear transmittance as a function of N for double-resonant microcavities with both phase matching and anti-phase matching, and for single-resonant microcavities. The symbols denote the results of the transfer matrix calculation, while the lines represent the trends given by the Q-factors.

DRM with anti-phase matching, $T^{NL} \propto Q_\omega^2$ for a SRM.

The results that have been shown demonstrate a great enhancement of SHG in a phase-matched doubly resonant microcavity. Nevertheless this structure present several practical limitations: a shorter DRM is desirable , in which the pump wavelength is tuned around $1.550\mu m$, and finally the growth orientation [001] is preferable. This new goal requires a more in-depth study of the SHG process in doubly resonant systems, which is presented in the following section.

2.5 AlGaAs cavity with AlGaAs/Alox dielectric mirrors

AlGaAs cavity

In this section we are going to consider AlGaAs cavity with periodic dielectric mirrors made of Alox/AlGaAs in thin configuration [67]. All the structures presented here are designed in order to operate at a pump wavelength around $1.5\mu m$, the choice of a thin configuration allows to achieve

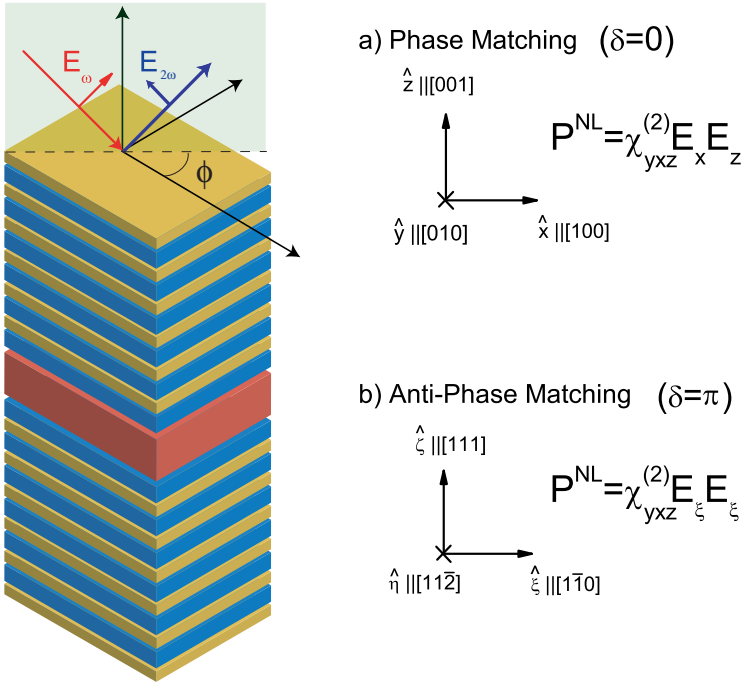

Figure 2.13: Scheme of nonlinear microcavity, with two different growth directions [001] (a) and [111] (b). In the former case the nonlinear polarization is proportional to $E_x E_z$, while in the latter case P^{NL} is proportional to E_ξ^2.

high conversion efficiency in very compact structures and offers the experimental advantage of growing the phase matched structure in [001] direction. Two different in/out field polarizations are considered, $p-s$, with growth orientation [001] and [111], and $s-p$ when the z axis is taken in the [001] direction.

2.5.1 P-S configuration

The DRM is composed by a $Al_{0.25}Ga_{0.75}As$ cavity layer of width $L_c = 449.7\,nm$, embedded in two DWDM that are composed by alternated layers of Alox and $Al_{0.4}Ga_{0.6}As$, whose gap map is presented in figure 2.5b. When $f = 0.4$ we get a wide superposition of the pump and harmonic gaps around 0.8 eV, which corresponds to the following mirrors parameters: $L_1 = 116.8\,nm$ (Alox) and $L_2 = 175.2\,nm$ ($Al_{0.4}Ga_{0.6}As$). The pump resonance is tuned at the convenient wavelength of $1.55\,\mu m$ ($E = 0.8$ eV). This corresponds to the thin configuration marked with arrows in Fig. 2.5.

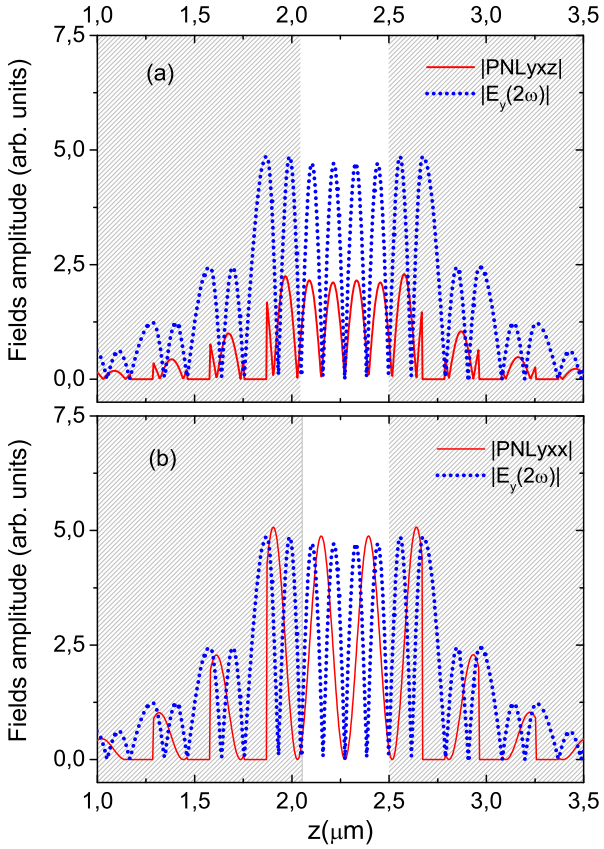

Figure 2.14: Nonlinear polarization (solid line) and free harmonic field (dashed line) in the DRM structure at the resonance frequency $E = 0.8$ eV in the case of phase matching (a) and anti-phase matching (b). The growth orientation is taken to be [001] and [111], respectively. The number of periods $N = 7$ and the incidence angle $\theta = 33^\circ$. The white area represents the cavity region.

The microcavity has been designed in order to achieve double resonance in p-s configuration and phase matching when the growth orientation is [001] so that the only relevant element of the nonlinear susceptibility tensor is $\chi^{(2)}_{yzx}$. In the case of a [001] growth direction (see Fig. 2.13a), the *s*-polarized nonlinear polarization is proportional to the product $E_x E_z$ and,

as it turns out, we get phase matching. In the opposite case of a [111] growth direction (Fig. 2.13b), instead, the nonlinear polarization is proportional to E_ξ^2. In this case the anti-phase matching situation is realized.

If we look the *s*-polarized nonlinear polarization and harmonic fields at the resonance frequencies, shown in Fig. 2.14, we notice that the two quantities oscillate in phase in the phase matching case (a) but are out of phase in the the anti-phase matching case (b). This figure allows to visualize in physical terms the reason for the strongly increased SHG efficiency in the case of phase-matching. However, these conditions are satisfied only inside the cavity layer. Since the $\chi^{(2)}$ of the $Al_{0.25}Ga_{0.75}As$ and $Al_{0.4}Ga_{0.6}As$ are comparable [66], the contributions of the nonlinear layers of the DWDM have to be considered. Nevertheless we observe that, in both cases, the behavior of the system is well described by Eq. (2.9): indeed at 0.8 eV the pump field is strongly confined in the cavity layer which represents the dominant contribution to SHG.

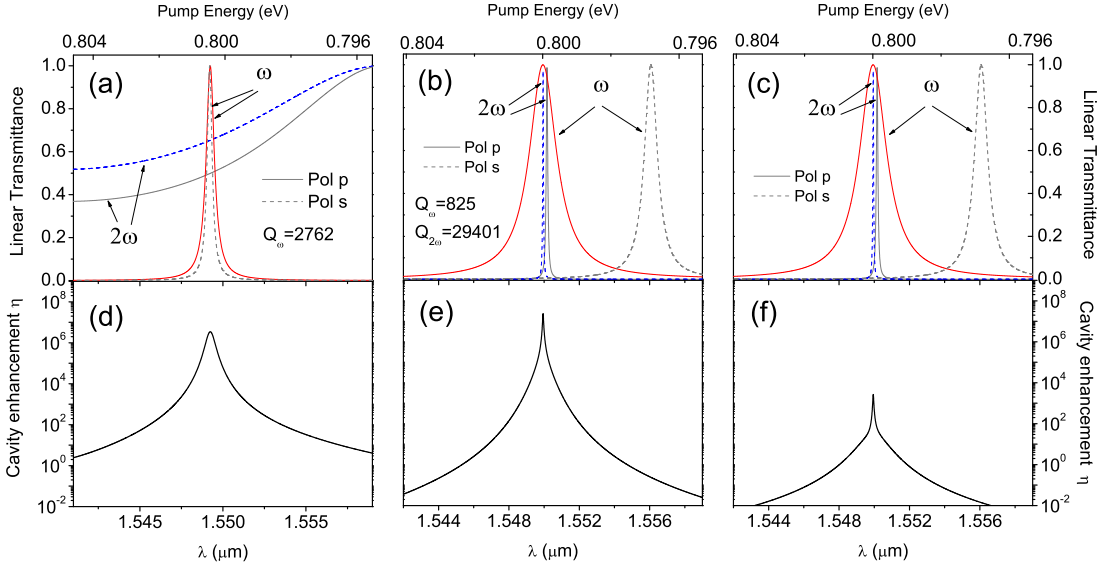

Figure 2.15: Linear transmittance versus pump wavelength for a single-resonant microcavity with [001] growth direction (a) and doubly-resonant microcavities in phase matching ([001] growth direction) (b) and anti-phase matching ([111] growth direction)(c). The respective cavity enhancement factors are reported in panels (d),(e) and (f). The SRM and DRM are constituted by a cavity layer of $Al_{0.25}Ga_{0.75}As$ embedded in two mirrors composed by $N = 7$ periods of alternating $Alox/Al_{0.4}Ga_{0.6}As$. In the case of SRM $L_c = 242.8$ nm, $L_1 = 231.6$ nm and $L_2 = 123.8$ nm, while for the DRM $L_c = 449.7$ nm, $L_1 = 116.8$ nm and $L_2 = 175.2$ nm. The pump and harmonic fields are p and s polarized, respectively. The incidence angle $\theta = 29°$ for SRM and $\theta = 33°$ for DRMs.

PM and growth direction

Let us demonstrate more generally that the same structure parameters can be used in order to achieve double resonance with phase- or anti-phase matching when the growth direction is changed from [001] to [111]. From Eq. (2.10) we evaluate $\delta_{\rm m}$ for the two different cases:

$$\delta_{\rm m}^{[001]} = \phi_{x,\omega} + \phi_{z,\omega} + 2k_{z,\omega}L + \phi_{y,2\omega} + k_{z,2\omega}L, \tag{2.21}$$

$$\delta_{\rm m}^{[111]} = \phi_{\xi,\omega} + \phi_{\xi,\omega} + 2k_{z,\omega}L + \phi_{\eta,2\omega} + k_{z,2\omega}L. \tag{2.22}$$

Since $\phi_{z,\omega} = \phi_{x,\omega} + \pi$, if we subtract (2.21) from (2.22) we obtain that

$$\delta_{\rm m}^{[001]} - \delta_{\rm m}^{[111]} = \pi. \tag{2.23}$$

Thus, for the present *p*-*s* configuration it possible to switch from the phase-matching to the anti-phase matching condition by changing the substrate orientation.

We compare the DRM with a single-resonant microcavity formed by a $\lambda/2$ layer of $Al_{0.25}Ga_{0.75}As$ with $L_c = 242.8$ nm embedded between two identical $\lambda/4$ DBRs constituted by $N = 7$ periods of Alox/$Al_{0.4}Ga_{0.6}As$ with $L_1 = 231.6$ nm and $L_2 = 123.8$ nm. The linear transmittance at ω and 2ω and the cavity enhancement factor of the SRM and DRM in the phase matching and anti-phase matching cases are plotted in Fig. 2.15 as a function of pump wavelength. In the case of the SRM the pump linear transmittance exhibits two resonances tuned around 1.55 μm, while the transmittance at 2ω is structureless. Both DRMs are characterized by the same linear transmittance spectra, in particular we observe resonances for the p and s modes at ω and 2ω, double resonance being achieved in *p*-*s* configuration. From the linear spectra of Fig. 2.15 it is possible to have indication about the values of the Q-factor for the pump and the harmonic resonances, in particular we notice that in the single-resonant microcavity Q_ω is greater than in the DRM. Nevertheless, the cavity enhancement factor is about 10 times larger in the DRM with phase matching because it is proportional to the product $Q_\omega^2 Q_{2\omega}$. Also, the DRM in phase-matching configuration has 10^4 higher SHG efficiency than in the anti-phase matched case.

Exponential growth with N

In Fig. 2.16a we compare the trends of the cavity enhancement factors calculated through the nonlinear transfer matrix method to the ones predicted by the analytical formulation as a function of the number N of mirror periods for the DRM. In all cases we observe an exponential growth. The phase-matched DRM exhibits the highest cavity enhancement for all values of N. For N=6 periods the enhancement factor is higher than 10^6. The analytical results are generally close to the numerical ones, except in the SRM, for which the mirror layers give a significant contribution and the analytic formula (2.9) underestimates the conversion efficiency. In Fig. 2.16b we report the quality factors of the resonances involved in the nonlinear

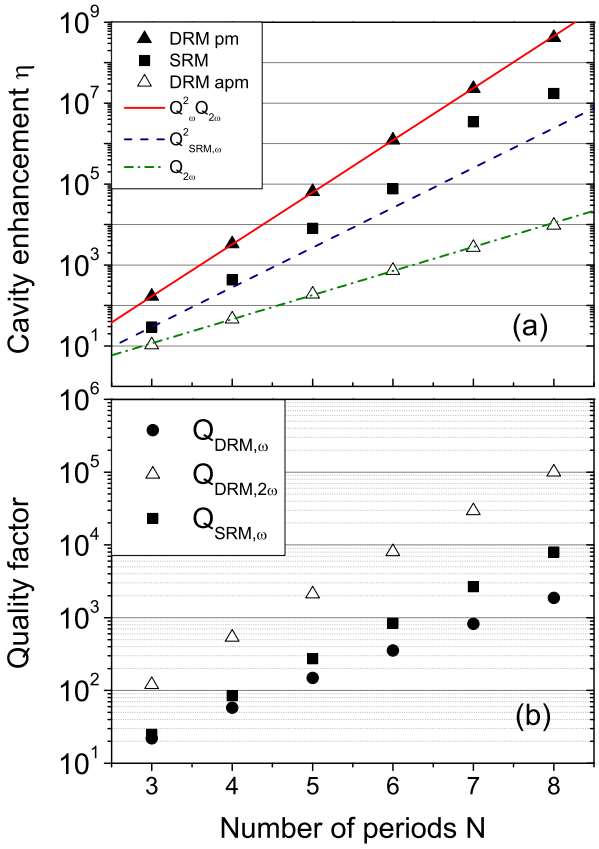

Figure 2.16: (a) Cavity enhancement factor in p-s configuration as a function of the number N of mirror periods for a doubly-resonant microcavity in phase matching and anti-phase matching, and for a single-resonant microcavity. The symbols denote the results of the transfer matrix calculation, while the lines represent the exponential trend predicted by the analytical formulation. (b) Quality factors of the resonances at the pump and harmonic frequencies. Structure parameters are as in Fig. 2.15. The incidence angles are $\theta = 29°$ and $\theta = 33°$ for the SRM and DRM, respectively.

process. Note that, while the Q-factors of the pump resonances are comparable, the Q-factor of the harmonic one is considerably higher, therefore the cavity enhancement in the anti-phase matching condition follows the trend

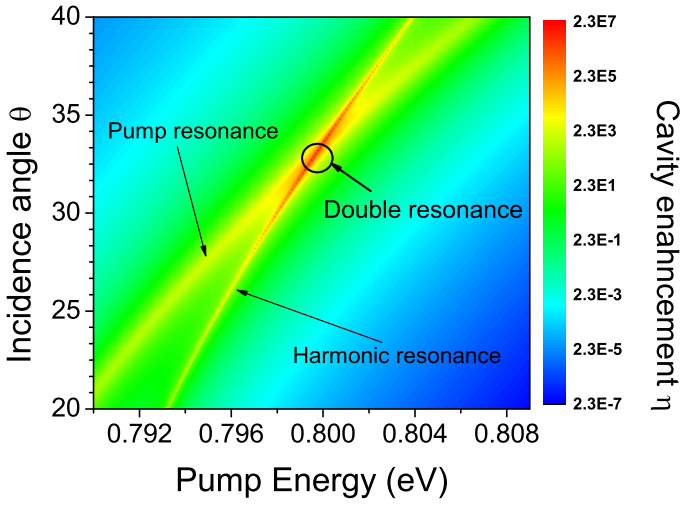

Figure 2.17: Cavity enhancement factor (color scale) as a function of pump energy and incidence angle, for N=7 and in phase matching configuration.

predicted by Eq. (2.14). The higher Q-factor at 2ω follows from choosing a *p-s* configuration (the DBR reflectance at finite angle of incidence is obviously higher for *s* than for *p* polarization). In real samples, the Q-factors of Fabry-Pérot in high-quality microcavities can be of the order of a few thousands: thus the enhancement factor for the present DRM is limited by the Q-factor at 2ω. In the following subsection a different configuration with more balanced Q-factor values is proposed.

In Fig. 2.17 we give a summary of the above discussion: the enhancement factor due to the presence of the resonance at the pump and harmonic frequencies is clearly visible. As we have seen their relative position is a function of the incidence angle, which is as a powerful tuning parameter so that at $\theta = 33°$ we achieve the maximum cavity enhancement because of the doubly resonance condition. Notice in particular that the higher Q-factor of the harmonic resonance is well visible since the corresponding enhancement line is thinner than the pump one.

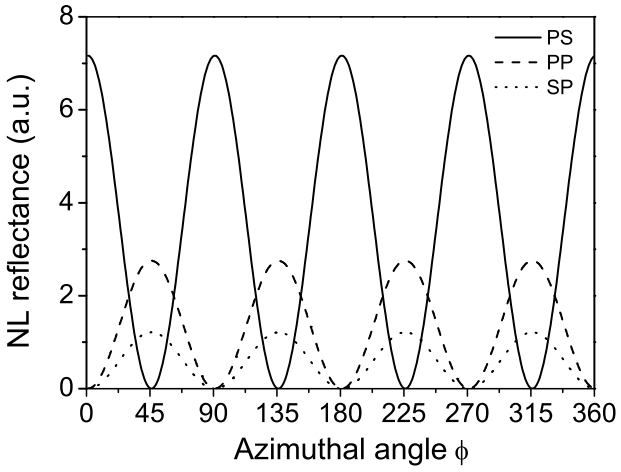

Figure 2.18: Nonlinear reflectance of a semi-infinite $Al_{0.25}Ga_{0.75}As$ layer oriented along [001], as a function of azimuthal angle with respect to [100] direction. The incidence angle is $\theta = 45^\circ$ and the pump wavelength $\lambda = 1.5\,\mu m$.

2.5.2 S-P configuration

The DRM structure presented in the previous section exhibits a very high enhancement of the generated second-harmonic as compared to the SRM one, especially if we consider the conversion efficiency vs the total device length. Nevertheless, the strong SHG enhancement is mostly related to the very high Q-factor of the harmonic resonance, which followed from choosing a *p*-*s* polarization configuration (the DBR reflectance at finite angle of incidence is obviously higher for *s*-polarization).

In this subsection we present a DRM with phase matching in which the Q-factors at ω and 2ω are of the same order. We choose to work in *s*-*p* configuration in order to reduce the Q-factor at the harmonic frequency, while maintaining the polarization splitting of the cavity resonances in order to use the incidence angle as a tuning parameter. We consider only a [001] growth direction: in order to have a finite nonlinear polarization with *s*-polarized pump, the plane of incidence must be oriented along a [110] crystallographic axis. In other words, as compared to the structure shown in Fig. 2.13a, the sample must be rotated by an azimuthal angle $\phi = 45^\circ$. In Fig. 2.18 the nonlinear reflectance is plotted as a function of the azimuthal angle ϕ between the plane of incidence and the direction [100]. The crystal

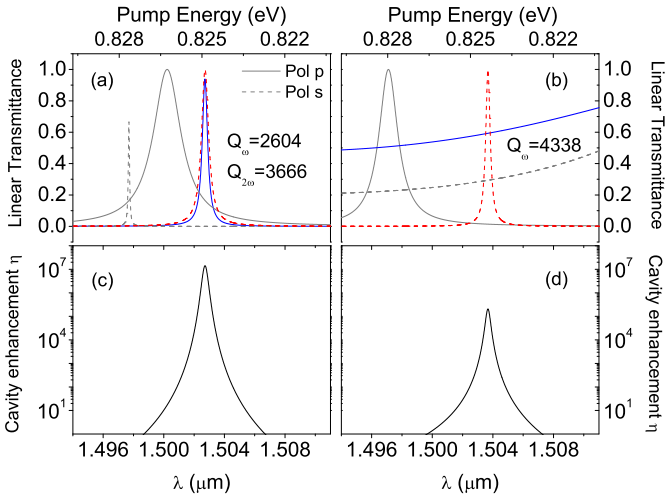

Figure 2.19: Linear transmittance versus pump wavelength for a phase-matched DRM (a) and a SRM (b) and their respective cavity enhancement factors in s-p configuration (c),(d). The growth direction is assumed [001] and the incidence angle $\theta = 41°$. The DRM and SRM are formed by a defect of $Al_{0.25}Ga_{0.75}As$ embedded in two mirrors composed by N=5 periods of alternating $Al_{0.4}Ga_{0.6}As$/Alox. In the case of DRM $L_c = 744\,nm$, $L_1 = 170\,nm$ and $L_2 = 140\,nm$, while for the SRM $L_c = 245\,nm$, $L_1 = 113\,nm$ and $L_2 = 230\,nm$.

orientation is still assumed [001] and the incident angle is $\theta = 45°$. All the possible in/out polarization configurations are displayed. We observe that for any value of ϕ the conversion *s-s* is forbidden, while for $\phi = 45°$ the SHG in *s-p* and *p-p* have a maxima. If we look at the nonlinear tensor $\chi^{(2)}$ in *s-p* configuration, for $\phi = 45°$, we observe that only the component $\chi^{(2)}_{zyy}$ takes part in the SHG process. In this section we shall assume this configuration and consider only phase-matching microcavities. Following the gap-map method developed in Secs. 2.1 and 2.2, we design a DRM in which double resonance is achieved for an incidence angle close to $\theta = 40°$ at the pump wavelength $\lambda = 1.5\,\mu m$. We found the following parameters: the DRM is formed by a $Al_{0.25}Ga_{0.75}As$ layer of width $L_c = 744\,nm$ embedded in $Al_{0.4}Ga_{0.6}As$/Alox DWDM with $L_1 = 170\,nm$ ($Al_{0.4}Ga_{0.6}As$) and $L_2 = 140\,nm$ (Alox). The SRM is made of a $\lambda/2$ $Al_{0.25}Ga_{0.75}As$ layer of width $L_c = 245\,nm$ embedded between two $Al_{0.4}Ga_{0.6}As$/Alox $\lambda/4$ mirrors with $L_1 = 113\,nm$ ($Al_{0.4}Ga_{0.6}As$) and $L_2 = 230\,nm$ (Alox). Note that the

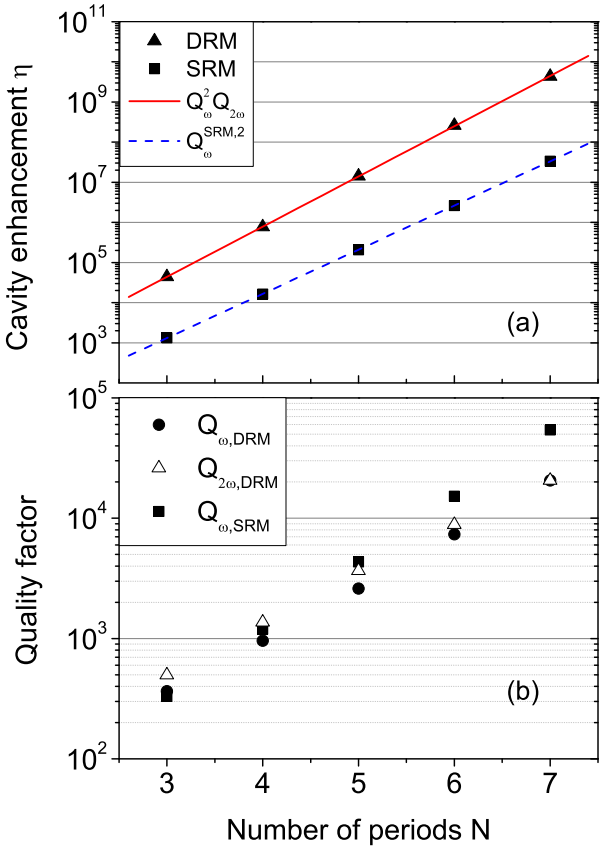

Figure 2.20: (a) Cavity enhancement factor in s-p configuration for a phase-matched double-resonant microcavity and for a single-resonant microcavity. The symbols denote the results of the transfer matrix calculation, while the lines represent the exponential trend predicted by the analytical formulation. (b) Quality factors of the resonances. Parameters are as in Fig. 2.19.

DBR layer nearest to the cavity is Alox.

In Fig. 2.19 the linear transmittance at ω and 2ω is plotted as a function of pump wavelength for the DRM (a) and the SRM (b) in *s-p* configuration. Again for the DRM we get a superposition of the pump and harmonic resonances, while in the SRM we have only one resonance centered

around 1.5 μm for the *s*-polarized mode. It is interesting to observe that the Q-factors of the DRM resonances are both lower than the SRM one. Nevertheless, the enhancement factor of the DRM is superior to that of the SRM by more than two orders of magnitude. Therefore in the present *s-p* configuration a DRM can have higher nonlinear conversion as compared to a SRM while requiring lower Q-factors. Thus, the DRM is on all respects more convenient than a SRM.

In Fig. 2.20 we plot the cavity enhancement and the *Lower Q-factors* quality factors as a function of the number N of mirror periods. Again the cavity enhancement η grows exponentially with N, moreover there is good agreement between numerical and analytical calculations. This result follows from the different DBR configuration, in which the Alox layer is adjacent to the cavity one. In this way the index contrast close to the cavity increases and furthermore the two Alox layers do not present a $\chi^{(2)}$ nonlinearity, so that their contribution is vanishing.

The present DRM structure in *s-p* configuration allows achieving a cavity enhancement of the order of 10^7 and a nonlinear transmittance of $\sim 10^{-12} m^2/W$ with a device length smaller than 4μm and Q-factors of the order of a few thousands. The notable feature of this configuration is that the Q factors at ω and 2ω are comparable. In conclusion the present structure may be a convenient one in view of obtaining high nonlinear conversion in a double-resonant cavity system.

2.6 Amorphous silicon nitride doubly resonant microcavities

Surface nonlinearity

In the previous section the problem of SHG in doubly resonant system has been discussed for the case of bulk nonlinearity. As we have seen in Sec. 1.3, SHG from centrosymmetric materials originates from two different sources: surface nonlinearity and non-local bulk quadrupole nonlinearity. It has been suggested in Ref. [68] that the mechanism for SHG in the related system a-Si:H does not follow from a bulk nonlinear susceptibility $\chi^{(2)}$ (which vanishes on the average for these amorphous materials, due to a small-range topological disorder), but rather from a surface contribution, i.e., inversion symmetry is macroscopically broken at the film-substrate and film-air interfaces, thereby leading to a surface $\chi^{(2)}$ originating from dipole layers. In that work a clear evidence was found for two resonances at about 1.2 eV and 1.4 eV, independently of the polarization state of the impinging beam. These results strongly suggest that the (local) surface contribution in second order nonlinear susceptibility is the dominant one in amorphous silicon. In fact, those resonances are close to the 1.15 and 1.3 eV spectral resonances observed by Pedersen and Morgen in the SHG spectrum of bulk silicon due

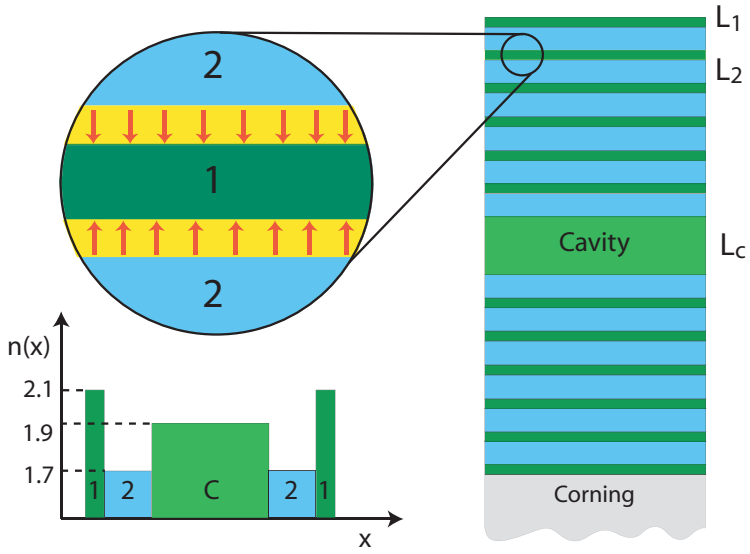

Figure 2.21: Layout of the microcavity structure, made of a defect layer "c" embedded between two dielectric mirrors made of layer "1" and "2". A fictitious layer is introduced at each interface, the red arrows denote the directions from low to high refractive index, which determine the sign of the $\chi^{(2)}$ components.

to transitions from rest-atom to ad-atom dangling-bond surface states [69]. The same conclusion is expected to apply also to the a-$Si_{1-x}N_x$:H multilayers investigated here. In order to verify such effect, one can monitor the SH signal while exposing the sample to the same surface selective process or interaction, such as, for example, gas and/or liquid absorption. Here we analyze the nonlinear response of a doubly resonant microcavity based on amorphous silicon nitride (a-$Si_{1-x}N_x$:H), for which second order nonlinearity arises from lack of inversion symmetry at the interface between two different layers.

These structures are suitable systems for generating second harmonic in the visible region, due to their large band gap [70]. The microcavities can be produced by modulating the refractive index, which increases as a function of the nitrogen content [71, 72].

The transmitted second harmonic intensity was calculated by means of the nonlinear transfer matrix method [52]. The surface $\chi^{(2)}$ is described by introducing very thin layers of thickness δ (typically 0.1 nm) at the interfaces, with a refractive index which is the average between those at the two sides of the interface and an effective bulk $\chi^{(2)}_{\text{bulk}}$ given by $\chi^{(2)}_{\text{bulk}} = \chi^{(2)}/\delta$. The surface nonlinear susceptibility has three non-vanishing components: $\chi^{(2)}_{zzz}, \chi^{(2)}_{xzx}$

and $\chi^{(2)}_{zxx}$ since the surface $\chi^{(2)}$ is generated from dipoles which have a component pointing from the low to the high refractive index medium as shown in Fig. 2.21. Each of the $\chi^{(2)}$ component changes its sign when the ordering of the refractive indices is reversed [73][2]. For simplicity, we assumed the surface $\chi^{(2)}$ of the a-$Si_{0.57}N_{0.43}$/a-Si_3N_4 and a-Si_3N_4/a-$Si_{0.45}N_{0.55}$ interfaces to be the same.

A layout of the microcavity is shown in Fig. 2.21. The structure parameters are as follows: L_1=73nm (a-$Si_{0.57}N_{0.43}$), L_2=219 nm (a-Si_3N_4), L_c=613nm (a-$Si_{0.45}N_{0.55}$). The design has been done by the procedure described in Secs. 2.1 and 2.2 in order to achieve double resonance at a finite incidence angle $\theta = 40°$, for p-polarized pump and harmonic waves. The sample has been grown in Torino by the research group of Prof. F. Giorgis using 13.56 MHz Plasma Enhanced Chemical Vapor Deposition (PECVD) system on 7059 Corning glass substrates with area 10 x 10 cm^2.

Sample growth

The composition of the a-$Si_{1-x}N_x$:H layers was controlled by operating on the ammonia fraction present in a SiH_4+NH_3 plasma, by fixing the total flux at 75 sccm. Their thickness was estimated taking into account the growth rate calculated by homogeneous thin films previously grown, while the composition (x=N/Si+N) of the alloys has been estimated by considering their refractive indices n, through a calibration curve $n(x)$ obtained by Rutherford backscattering spectrometry and optical interferometry performed on some selected a-$Si_{1-x}N_x$:H specimens. The substrate temperature, gas pressure and electrode distance were fixed at 200 °C, 0.35 Torr and 20 mm respectively.

Linear characterization

Measurement of transmittance spectra were performed in Napoli by the research group of S. Lettieri [74]. The results are in close agreement with numerical calculations of the transmission spectrum based on a linear transfer matrix method. In Fig. 2.22 we show the experimental transmittance for p-polarized impinging light at $\theta = 40°$ (open dots) in a wavelength range centered on the fundamental resonance ($\lambda = 1.09\,\mu$m) and the transmission at the doubled frequency (full dots). It is to be noted that the transmission peaks overlap: in other words, double resonance occurs.

Nonlinear results

In Fig. 2.23 we show a typical SH spectrum obtained in transmission geometry for p-polarized fundamental beam. The full dots are the experimental data, while the continuous line is the result of the numerical calculation which we will discuss below. The SH signal increases by a factor of about

[2]The sign change of $\chi^{(2)}$ (or of the effective $\chi^{(2)}_{\rm bulk}$) when the interface is reversed is analogous to the mechanism occurring in periodic poling, which may be used to achieve quasi phase matching in isotropic nonlinear materials.

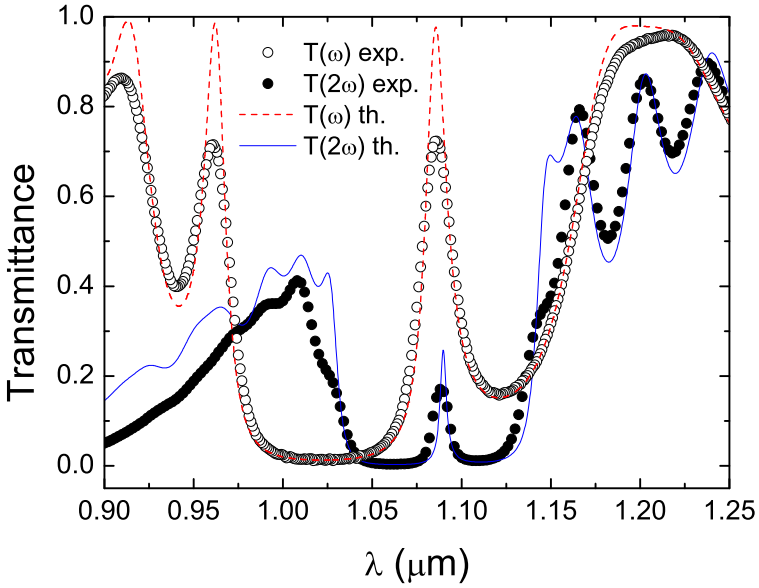

Figure 2.22: Linear transmittance for p-polarized light at an angle of incidence $\theta = 40°$, in the spectral region of the pump wave (open dots and dashed line) and of the harmonic wave (full dot and solid line), as a function of pump wavelength. Points: experimental results. Lines: theory.

10^2 as the fundamental wavelength goes from the first order stop-band to a resonant wavelength of the structure (central resonance and band-edge peaks): the central peak in the SH spectrum corresponds to the double resonance of the microcavity, while the other features corresponds to the edges of the stop-bands. The resonant enhancement can be ascribed to a high intensity of the light beams at the fundamental and harmonic frequencies at the interfaces surrounding the cavity layer. Moreover, it is interesting to note that the SH signal detected at the central resonance is hundreds of times larger than the one obtained on a single amorphous silicon nitride film.

The nonlinear performances of a-$Si_{1-x}N_x$:H microcavity are quite similar to the bulk system one, in the sense that in both cases the double resonance condition determines a good enhancement of SHG. Nevertheless we wish to emphasize that the analytic treatment of SHG presented in Sec. 2.3 is based on the assumption that the cavity layer is characterized by bulk

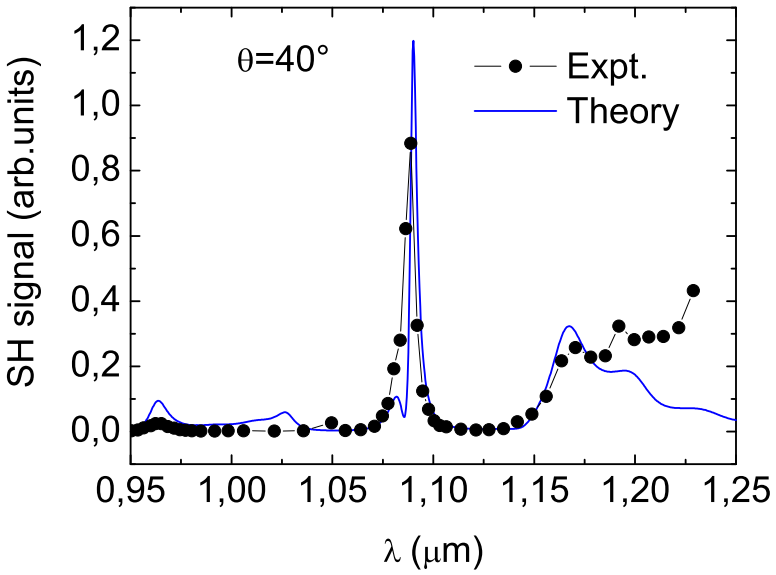

Figure 2.23: Transmitted second-harmonic signal as a function of pump wavelength, for p-polarized pump and harmonic waves, at an angle of incidence $\theta = 40°$.

nonlinearity, while in the present case nonlinear polarization is localized in only at the multilayer interfaces. For this reason the analytic results can not be immediately applied and require an opportune generalization, which is beyond the aim of this work.

2.7 Remarks on Kerr effect in microcavities

In Secs. 2.4, 2.5 and 2.6 we have described the use of planar microcavities in order to increase the conversion efficiency of SHG and, in particular, we have focused our attention on double resonant microcavities. It should be clear that the main advantage in using a MC is the high pump field intensity that can be achieved in the cavity layer, which is proportional to the cavity Q-factor. When the pump field intensity is so high, further higher order nonlinear effects which can affect light propagation in the structure are present. If we limit our attention to third order nonlinearity, the most important one is the Kerr effect [3]. As a matter of fact in a medium charac- ***Kerr effect***

[3]This effect is at the base of many interesting phenomena such as light and dark solitons and light filamentation [75, 76].

terized by cubic nonlinearity the propagating field induces a refractive index change which is proportional to the field intensity

$$n = n_0 + n_2 I, \tag{2.24}$$

where n_0 is the linear refractive index, while n_2 depends on the third order nonlinear susceptibility according to

$$n_2 = \frac{4\pi^2 \chi^{(3)}}{n_0^2 c}. \tag{2.25}$$

In a microcavity (or simply in a Fabry-Pérot resonator) with cubic nonlinearity, Kerr effect can lead to optical bistability [77–80]. Here we are not interested in a detailed study of the phenomenon, even though it is the subject of considerable applicative interests.
In the calculation of the second-order nonlinear response, which we have presented in Secs. 2.4, 2.5 and 2.6, we completely neglected any other nonlinear effect. Of course this drastic approximation has to be justified, since very high Q-factors have been predicted for Alox/$Al_{1-x}Ga_xAs$ microcavities and the electric field in the cavity is enhanced correspondingly. We performed a calculation of the linear transmittance at the pump frequencies by using the transfer matrix method which has been modified in order to include the refractive index modulation induced by the third order nonlinearity [4].

In Fig. 2.24 we show the linear transmittance as a function of the pump energies for increasing incident intensities. We observe a slight shift of the pump resonance position peak (only 40μ eV !) due to the induced refractive index change. This very small deviation is obtained by considering input intensities which are compatible with a non depletion regime for second harmonic generation (i.e. conversion efficiency less than 10%). In this case the refractive index can change considerably across the cavity layer, but since, very high field intensity are reached only in a small cavity region, the average refractive index deviation is small.
Other calculations have been performed for higher pump field intensities and effects of optical bistability have been observed, nevertheless in this limit the nonlinear transfer matrix method cannot be applied for a description of the second harmonic generation because pump depletion should be considered.

In conclusion we can affirm that in the cases we have examined, higher order nonlinearities, and in particular refractive index change induce by the Kerr effect can be neglected. the physical region is the distributed nature of the dielectric mirrors: a high refractive index change occurs only

[4] Note that the Kerr effect can affect only the pump resonance position, as a matter of fact, in the limit of negligible pump depletion, the harmonic generated field is not enough intense to induce sensitive refractive index changes at 2ω, even for very high Q-factors.

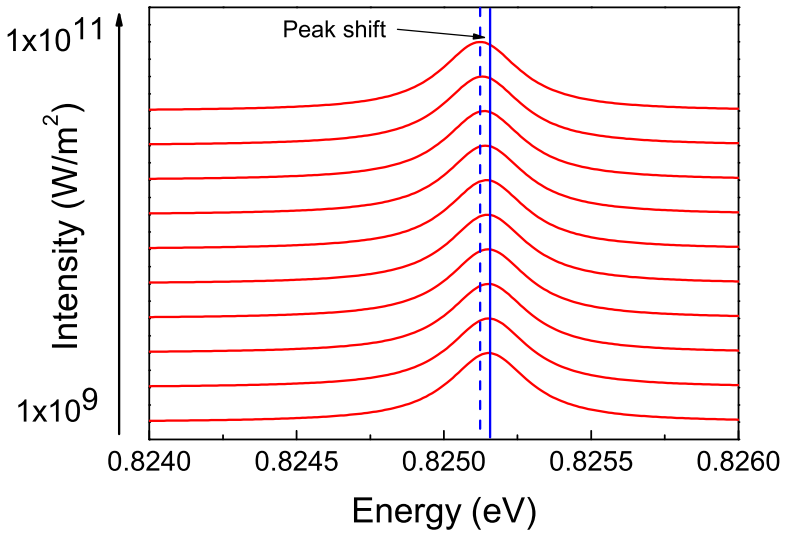

Figure 2.24: Linear transmittance as a function of the pump energy and intensity of a doubly resonant microcavity, at an angle of incidence $\theta = 40^\circ$ for s polarized incident field. The structure is the same of the linear and nonlinear calculations shown in Fig . 2.19 The DRM is formed by a defect of $Al_{0.25}Ga_{0.75}As$ embedded in two mirrors composed by N=5 periods of alternating $Al_{0.4}Ga_{0.6}As/Alox$ with $L_c = 744\,nm$, $L_1 = 170\,nm$ and $L_2 = 140\,nm$.

in the cavity layer, but it has small effect on the mode frequency which is determined to a large extent by properties of the mirrors. This is true in particular in doubly resonant structure in which high conversion efficiency require lower Q-values and therefore it is easier avoiding bistability effects.

2.8 Conclusions

We have shown that it is possible to design doubly-resonant microcavities using cubic materials where there is no birefringence to compensate the refractive index dispersion. To this purpose, it is essential to realize dual-wavelength dielectric mirrors with two stop-bands centered around the pump and the second-harmonic frequencies. The use of periodic mirrors allows the design to be carried out by means of the photonic gap map concept,

and makes the sample growth more robust against imperfections. Analogously, a planar microcavity can be viewed as a one-dimensional photonic crystal with a repeated defect layer. All the structure parameters can be found as a function of incidence angle and field polarizations. This way the incidence angle can be used as a powerful experimental parameter in order to tune the relative pump and harmonic resonance positions, in particular by exploiting the polarization splitting in *p*-*s* and *s*-*p* configurations.

A symmetric doubly-resonant microcavity is characterized by the presence of a precise phase relation between the nonlinear polarization and the harmonic field within the cavity layer. In particular we observe two different situations, namely phase matching and anti-phase matching. In the phase-matched case the nonlinear polarization is perfectly in phase with the harmonic field, resulting in a very high cavity enhancement factor which can be more than two orders of magnitude greater than in an equivalent single resonant microcavity. Furthermore, the increase in nonlinear conversion can be achieved with Q-factors at the pump and harmonic frequencies which are lower than in the reference single-resonant microcavity with $\lambda/4$ mirrors. In the anti-phase matched situation, the second harmonic generation turns out to be much less efficient since the nonlinear polarization is out of phase with respect to the harmonic field and the extraction efficiency of the generated harmonic field is drastically reduced. In all these cases there is exponential growth of the conversion efficiency as a function of the number of periods in the dielectric mirrors. Specific design for phase-matched, doubly-resonant microcavities in both *p*-*s* and *s*-*p* configurations have been provided that are amenable to experimental verification.

We have reported the first realization of a doubly resonant microcavity based on periodic mirrors, using a-$Si_{1-x}N_x$:H based multilayer with surface nonlinearity. Second harmonic emission properties of the structure were experimentally investigated, demonstrating that the double resonance condition significantly enhances the second harmonic conversion efficiency even in the case of surface nonlinearity. We also demonstrated that the experimental results can be properly described by a theoretical model based on the nonlinear transfer matrix method, in which the nonlinear polarization localized at the interfaces is taken into account by the introduction of fictitious layers at the interfaces. The results open the way towards improving the conversion efficiency in monolithic cavities made of centrosymmetric or amorphous materials.

Finally, we have briefly investigated the behavior of a doubly resonant microcavity including the Kerr effect, taking place inside the cavity layer. We have observed that for pump field intensities in the limit of negligible pump depletion, in these structures third order nonlinear effects can be neglected.

Chapter 3

Third-Harmonic Generation in Waveguides and Photonic Crystal Slabs

In this chapter we present a detailed study of third harmonic generation (THG) in Silicon-On-Insulator planar waveguides and photonic crystal slabs. Theoretical modeling of these phenomena has required the development of a new numerical method in order to describe nonlinear properties of PhC-slabs. In fact, the analysis of a planar waveguide can be performed by using the nonlinear transfer matrix method [52], nevertheless in the case of photonic crystal slabs, this method is numerically unstable. In Secs. 3.1 and 3.2 we present theoretical and numerical results regarding THG in a simple waveguide and corresponding one-dimensional photonic crystal slabs, respectively. The comparison of the nonlinear response of these two systems is necessary in order to understand the different roles of vertical field confinement induced in the waveguide and in the photonic crystal slab. In particular, we report the first observation of resonant enhancement of THG in SOI PhC slabs when the pump is frequency- and momentum-matched to a photonic mode of the structure. This work is the results of a collaboration with the research group of M. Malvezzi at electronics Department of the University of Pavia, where all the measurements presented here were performed.

In order to improve the agreement of theoretical calculations with measurements, we have developed an extension of the well-known scattering matrix (**S**-matrix) method [29] in order to include the analysis of nonlin-

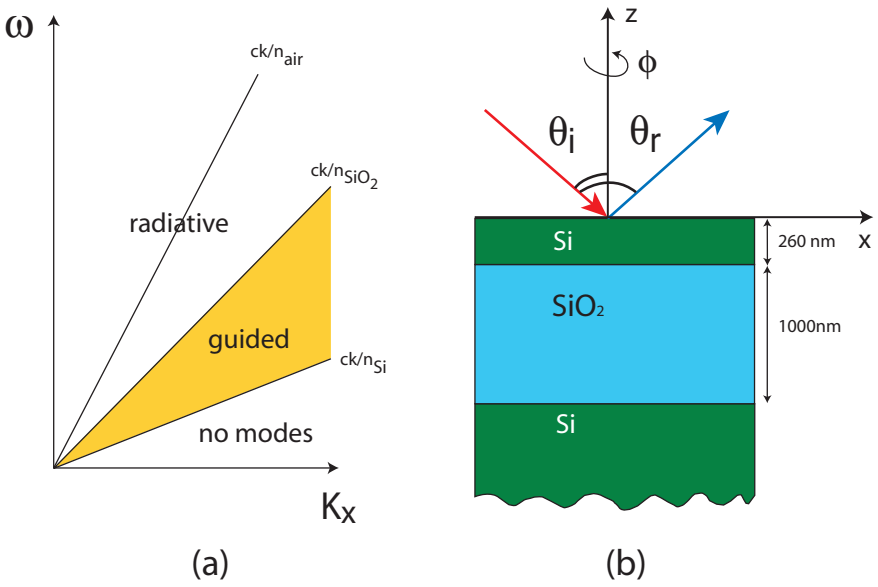

Figure 3.1: (a) Nature of photonic modes for a waveguide in the $k_x\omega$ plane. The light lines define radiative and guided mode regions. (b) Scheme of the SOI waveguide and geometry of the optical setup for third harmonic generation.

ear response of periodical pattern multilayer systems in limit of negligible pump depletion. This method is presented in Sec. 3.3 but unfortunately no numerical results are shown since its numerically implementation has to be still completed.

3.1 The SOI Planar Waveguide

In this section we shall describe the nonlinear response of a planar waveguide. This system has been chosen to represent the standard specimen, for comparison with the optical response from a 1D patterned sample.
Planar waveguide are commonly constituted of a thin slabs of high refractive index material (*core*), embedded between low index semi-infinite media (*cladding*). When the thickness of the core region is comparable with the wavelength of the electromagnetic radiation, we observe interesting effects in light propagation which are determined by the vertical confinement. Photonic modes can be calculated by solving Maxwell's equations and the solution are classified as guided and radiative (leaky) modes[56]. The first ones are evanescent in the cladding and oscillating within the core region,

and are discretized by the confining potential along z. The latter are oscillating also in the cladding region, as they radiate energy far away from the guiding layer. In the plane $k_x\omega$ the guided and radiative modes lies in different regions which are separated by the dispersion light lines (see Fig. 3.11).

The waveguide investigated here is a SOI wafer constituted by a silicon substrate , a SiO_2 layer, and a thin silicon top layer as shown in Fig. 3.11a. The high refractive index contrast between silicon ($n_1 \sim 3.5$) and silica ($n_2 \sim 1.45$) defines a planar waveguide, whose silica cladding and silicon core layers are $1\mu m$ and $0.26\mu m$ thick, respectively.

As we have seen in Chapter 1 silicon exhibits a very low second harmonic generation because of its centrosymmetric crystalline structure. On the other hand, the third harmonic generation process does not require the lack of inversion symmetry and is quite efficient in silicon. The study of reflected THG in this system can be done using the nonlinear transfer matrix, theoretical results are compared with measurements performed in Pavia. The geometry of the experimental layout is sketched in Fig. 3.11b, including notations for angles involved in the experiment: the angle of incidence θ and the azimuthal angle ϕ. THG is measured in a reflection geometry at two different pump wavelengths of 810nm and 1550nm, the choice of reflection geometry is due to high absorption of TH signal by silicon which makes it difficult to perform an experiment in transmission configuration [81].

Nonlinear tensor shape

In Fig. 3.2 we report measurements of reflected THG as a function of the azimuthal angle ϕ. Note in particular that since we are dealing with cubic materials, all linear properties are independent of ϕ and the $\pi/2$ periodic trend reported in Fig. 3.2 follows form on the symmetry properties of third order nonlinear susceptibility tensor. In centrosymmetric crystals, like silicon, $\chi^{(3)}$ has two independent nonvanishing elements A and B, and the i-th component of nonlinear polarization generated can be written as [82]:

$$P_{3\omega,i} = B(\mathbf{E}\cdot\mathbf{E})E_i + (A-B)E_i^3. \tag{3.1}$$

where $\mathbf{E}$ indicate the pump field vector. The first term of Eq. (3.1) determines a THG which has the same polarization of the incident pump field, while the second term exhibits a rotational symmetry which depends on the growth direction that, in the present case, is equal to [100] and is associated to a fourfold rotational symmetry. An analysis of the reflected THG intensity shows that the signal generated in the case of a waveguide can be two orders of magnitude higher than in the case of silicon, as reported in Fig. 3.2. This enhancement cannot be considered as a general characteristic of a SOI waveguide and it depends on the pump wavelength. Nevertheless it indicates that a modification of the spatial distributions of pump and harmonic fields along the vertical direction can lead to a great amplification of the TH signal. In our case, multiple reflections of the pump beam from the

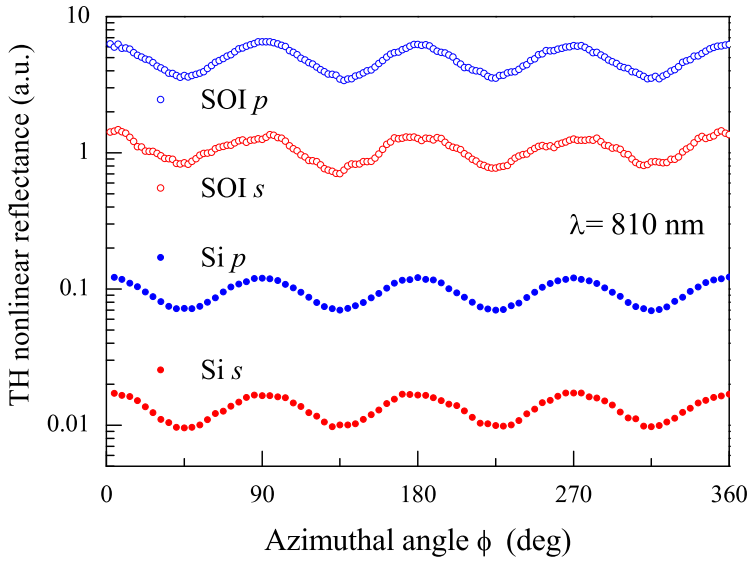

*Figure 3.2: Experimental TH nonlinear reflectivity as a function of azimuthal angle from the surface of the SOI planar waveguide (*open circles*) and of [100] bulk silicon sample (*full circle*), for p-polarized pump (*blue*) and s-polarized pump (*red*). Pump wavelength* $\lambda = 810$*nm and incidence angle* $\theta = 45°$.

interfaces result in constructive interference of the fundamental field into the core Si layer.

Incidence angle dependence

The waveguide configuration strongly modifies also the TH nonlinear reflectance when measured *versus* the angle of incidence θ. In Figs. 3.3 and 3.4 the nonlinear reflectance is plotted as a function of incidence angle for *s*-polarized (a) and *p*-polarized (b) input power for pump wavelength equal to 810nm and 1550nm, respectively. Note that the angular trends are completely different from those of the corresponding bulk silicon response [81] and that they depend on the pump wavelength. In both cases, at 810nm and 1550nm, the agreement between measured and experimental data is quite satisfactory. In Figs. 3.3 and 3.4, panel (c), the linear Fresnel transmission coefficients calculated for the multilayer structure are plotted. In the first case, for $\lambda = 810$nm, the TH escape length is less than 10nm (the TH linear transmission coefficient across the waveguide is zero for both polarizations),

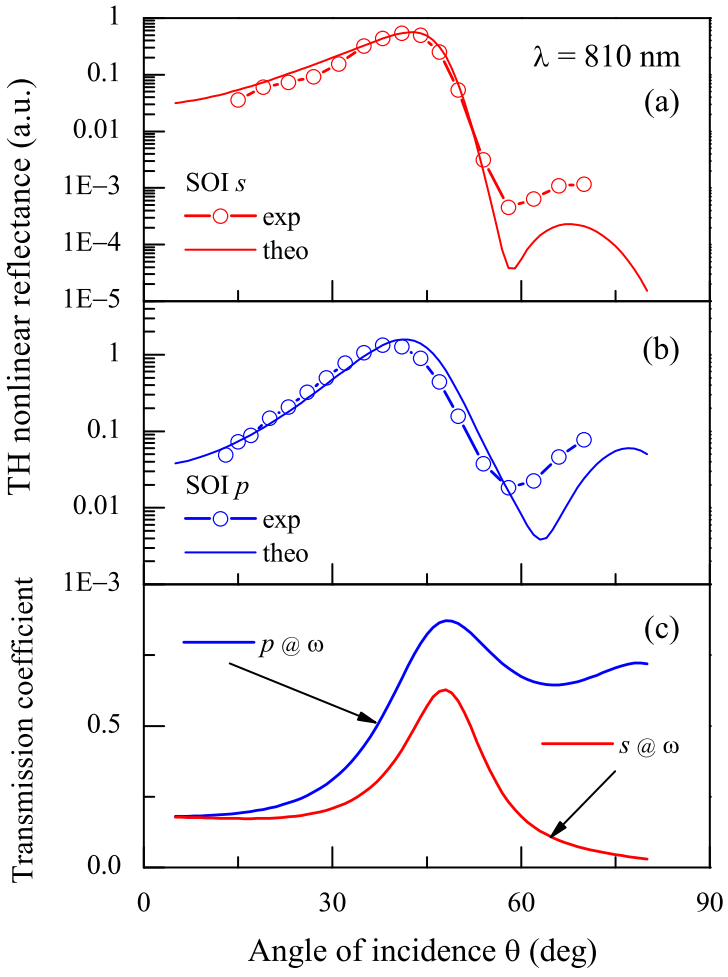

Figure 3.3: Experimental (open circles) *and calculated* (continuous lines) *TH nonlinear reflectance at 810 nm as a function of the angle of incidence, of a SOI planar waveguide, for (a) s-polarized and (b) p-polarized input. (c) Calculated linear transmission coefficients at ω for the two polarizations. The transmission coefficient at 3ω are zero because of the high absorption.*

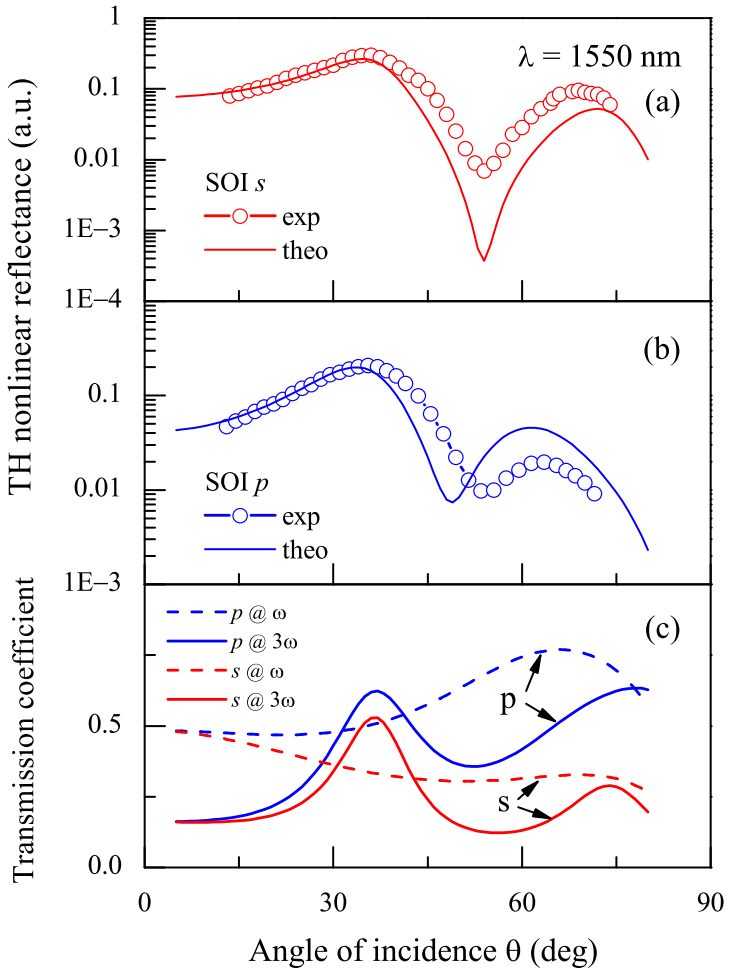

Figure 3.4: Experimental (open circles) *and calculated* (continuous lines) *TH nonlinear reflectance at 1550 nm as a function of the angle of incidence, of a SOI planar waveguide, for (a) s-polarized and (b) p-polarized input. (c) Calculated linear transmission coefficients at* ω (solid line) *and* 3ω (dashed line) *for the two polarizations.*

while the pump beam is fully propagating across the multilayer. In this case the reflected TH field is generated very close to the air/silicon interface and its angular behavior can be described starting from the linear transmission at ω, which gives indication on the pump field intensity flowing in the structure.
When the pump wavelength is tuned at 1550nm, the TH beam propagates along the structure (the penetration depth is about 1.4 micron) and the pump beam is not absorbed. In this case the nonlinear SOI reflectance is heavily affected by the response of the system at the TH frequency. As a matter of fact TH reflectance closely follows the angular behavior of the linear transmittance coefficient at 3ω, thus reflecting the higher extraction efficiency of the TH field generated from the silicon waveguide.

We can conclude by observing that even a such simple system the reflected THG can be characterized by a complicated angular and frequency dependence. This is the resuld of an interplay of linear propagation at ω and 3ω, nonlinear interaction and absorption.

3.2 The Photonic Crystal Slab

Let us consider now the case in which a periodic pattern is superposed on the SOI waveguide. A photonic crystals embedded in a planar waveguide is called *photonic crystal slab* (PhC-Slab). A scheme of the structure and an image of the sample are shown in Fig. 3.5a and b, respectively. In the last few years these systems have attracted a lot of interest since they allow a full three dimensional control of light and they are also much easier to fabricate than a three dimensional photonic crystal [55, 56]. Before considering the problem of THG it is necessary to give a brief overview of the most interesting linear properties of such systems.

Light-line problem

Light propagation in a patterned waveguide presents several differences with respect to the ideal reference system (i.e. the bare waveguide). One of the most important issues is the so-called *light-line problem*: as a matter of fact only the modes whose energy lies below the light line are truly guided, while those lying in the radiative region are coupled to leaky modes and thus are subject to radiative losses (see Fig. 3.5c). Truly guided mode exist only in systems with a strong refractive index contrast as in present case. They are evanescent in the direction perpendicular to the plane and their dispersion can be measured by attenuated total reflectance [63, 83], in this case light propagation is characterized only by extrinsic losses due to disorder. On the contrary, quasi-guided modes lie above the light line and are associated to sharp resonances arising from coupling of the incident light with the photonic structures: the dispersion of these mode can be measured using a variable angle reflectance technique [84]. Analogously, linear scattering matrix theory can be used in order to evaluate theoretical reflectance spectra

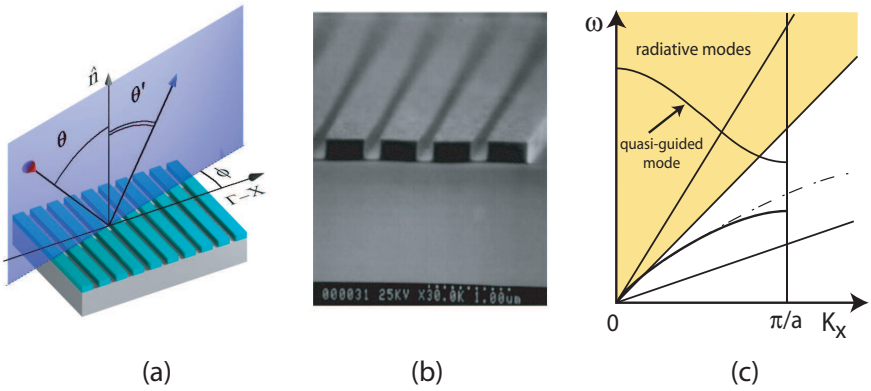

Figure 3.5: (a)Geometry of the optical setup for TH nonlinear measurements. The in-plane angle θ identifies the incident direction of radiation and θ' indicates the direction of radiation collection. The angle ϕ describes the rotation around the vertical axes respect to the $\Gamma - X$ direction.(b) Picture of L4 sample. (c) illustration of the nature of photonic eigenmodes in photonic crystal slabs.

and to reconstruct the mode dispersion curves [29].

The sample L4 we have considered is constituted by a patterned waveguide whose silica cladding and silicon core are 1000nm and 260nm thick, respectively (as in Sec. 3.1), and a periodic pattern in the core layer with lattice constant equal to $a = 650$nm and 0.18 of air fraction [85]. The sample was prepared at LPN-Marcoussis by D. Peyrade and Y. Chen, the scanning electron microscope image of the lattice, shown in Fig. 3.5b, reveals the very good quality of the sample.

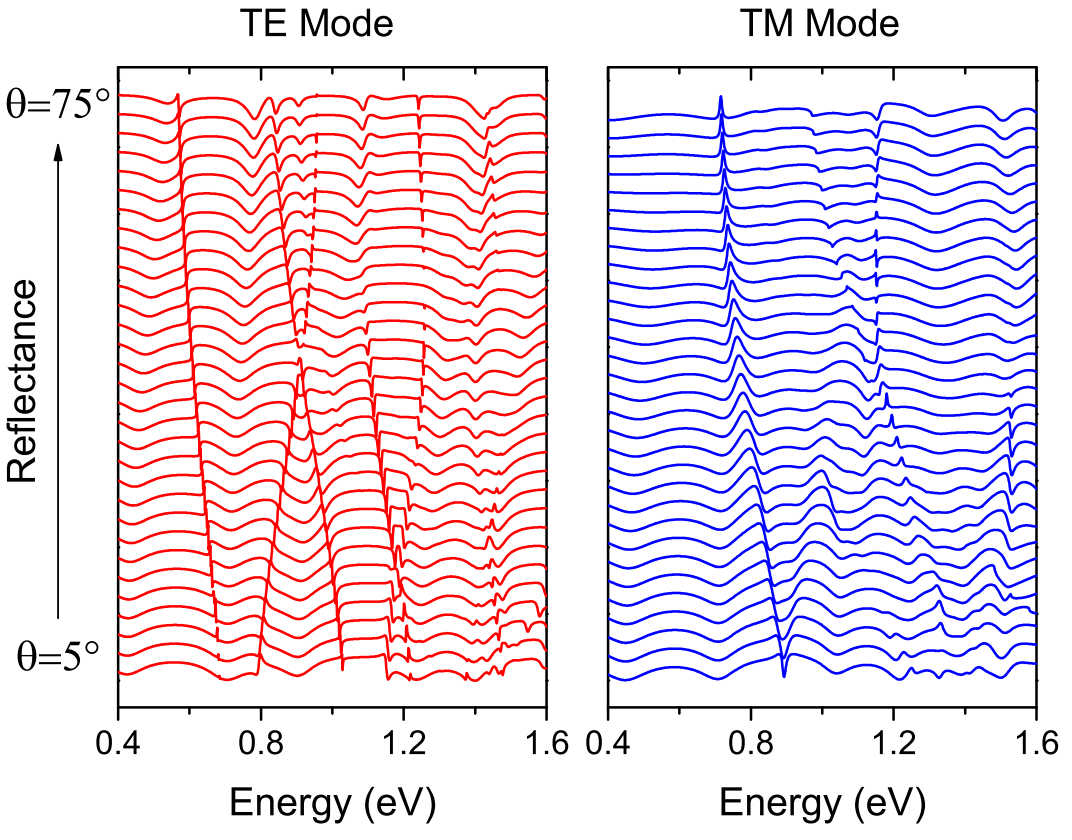

Figure 3.6: Calculated TE and TM linear reflectance spectra of sample L4 from $\theta = 0^\circ$ to $\theta = 60^\circ$.

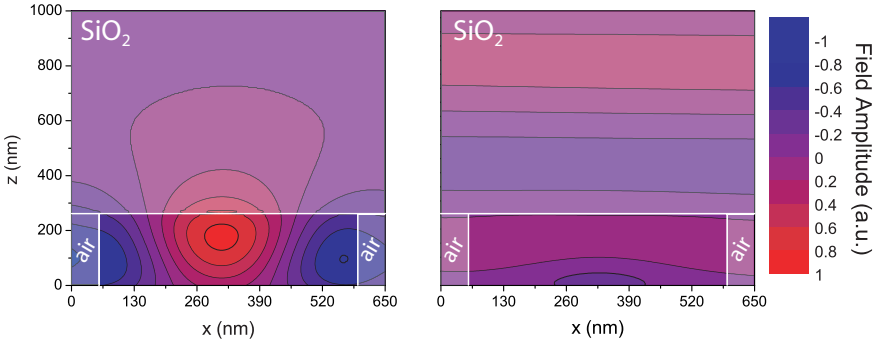

Figure 3.7: Calculation of E_y amplitude distribution inside L4 sample in the case of resonant (a) and non-resonant coupling (b). The shaded areas represent linear regions (air and silica) while the brightest area indicates the silicon.

Pump field distribution

In Fig. 3.6 calculated reflectance spectra of L4 for TE (*s*-polarized) and TM (*p*-polarized) modes are shown as a function of energy at several incidence angles. The theoretical calculation shows narrow resonant peaks superimposed to an interference pattern which is associated to the waveguide vertical structure. This peaks correspond to a resonant coupling with a quasi-guided mode and their dispersion as a function of incidence angle describe the photonic bands dispersion. When the electromagnetic radiation is coupled to a quasi-guided mode, the electric field turns out to be much more intense in the core region as it is shown in Fig. 3.7. This effect can be exploited in harmonic generation process, in particular to obtained intense nonlinear polarization when pump is resonant with the photonic band, or to achieve high extraction efficiency by coupling the harmonic signal to a quasi-guided mode. Enhancement of harmonic generation through resonant coupling was theoretically predicted in Ref. [27] and observed in GaAs [28, 86] and GaN [87, 88] systems. When frequency- and momentum matching is simultaneously realized for pump and harmonic beams we are in *resonant to resonant* configuration, otherwise when only the pump or the harmonic field are coupled to a photonic band we are in *resonant to non-resonant* and *non-resonant to resonant* case, respectively. In the present case we look for resonant coupling of laser radiation with photonic modes structures (i.e resonant to non resonant configuration), and we select an infrared wavelength for the pump field. There are several reasons that motivate this choice: from an experimental point of view, the effect of the disorder associated to Rayleigh scattering grow like ω^4, leading to a general broadening of higher-lying bands, but also photonic bands calculations are increasingly less accurate at high energies, also because the present PhC slab becomes multimode. One expects that therefore higher pump and stronger

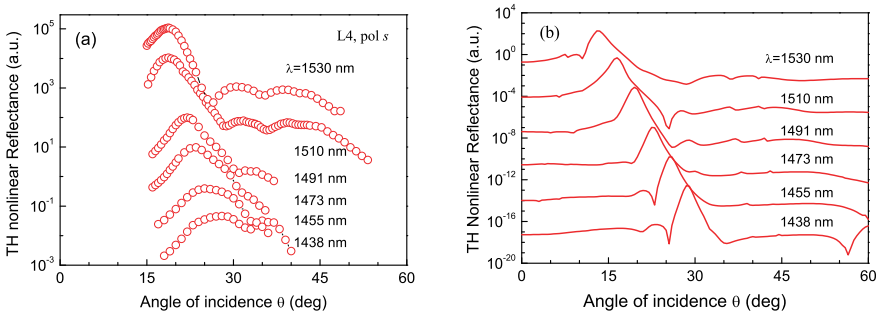

Figure 3.8: Experimental (a) and theoretical (b) behavior of third-harmonic nonlinear reflectance of sample L4, as a function of the angle of incedence for various wavelengths, with s polarized pump. the curves are offset for clarity.

nonlinear signals may be obtained.

It is worth remembering that the experiment is conducted in a surface reflection geometry, in which the incident electromagnetic wave dose not propagate along the waveguide plane. The comparison between PhC-slab and the bare waveguide can be done without introducing any coherence length, which is not easy to define in a PhC-slab.

Nonlinear results

Experimental and theoretical results for reflected THG are shown as a function of incidence angle for different pump wavelength, in the case of *s*-polarized pump, in Fig. 3.8a and b, respectively. For each pump wavelength the peak position corresponds to the linear reflectance resonance associated to a photonic mode and the dispersion as a function of pump λ is reproduced in the nonlinear calculations. This demonstrates that the enhancement of more than two orders of magnitude with respect to the bare waveguide signal is due to a resonant coupling of the pump with a quasi-guided mode.

3.3 Nonlinear scattering matrix method

Using the nonlinear transfer matrix method, it is possible to describe second- and third-harmonic generation in any homogeneous multilayer structure. In the limit of negligible pump depletion this method is an exact solution and it requires little computing time. Nevertheless the use of this method, even for solving linear problems, has found several limitations in patterned multilayer structures (like the one shown in Fig. 3.9a) due to its intrinsic numerical instability in the presence of evanescent Fourier model method. In order to study linear light propagation in these systems, Whittaker and Culshaw

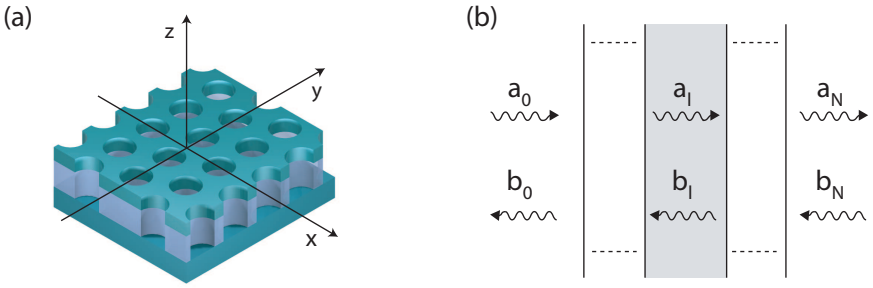

Figure 3.9: (a) Typical two dimensional pattern multilayer structure.(b) Forward and backward propagating waves in each pattern layer.

have described a scattering matrix method, which is essentially equivalent to Fourier modal method well known in diffraction grating theories. [89–92]. Here we present an extension of this method which allows to treat not only the linear propagation, but also harmonic generation in limit of negligible pump depletion. After a brief overview of the linear scattering matrix method we shall present its nonlinear extension, that can be divided in three independent steps: (i) description of pump field propagation and calculation of the nonlinear polarization, (ii) evaluation of the bound field in the nonlinear layers and (iii) calculation of reflected and transmitted harmonic fields.

3.3.1 The Scattering Matrix Method

A detailed description of the linear scattering matrix method implemented in this work [29]. Nevertheless it is worth to recall the main features of the method before introducing its nonlinear extension. The outline of the numerical method is as follows: the electromagnetic waves are expanded on a plane-waves set and Maxwell's equations are written in-plane momentum representation. The band structure of each patterned layer, taken to be homogeneous in the z direction, is evaluated yielding a set of states which propagates in the z direction as simple plane waves $\exp(\imath qz)$ (see Fig. 3.9b); the electromagnetic field is expanded on this set in terms of forward and backward Bloch states; finally the scattering matrix is constructed.

Linear problem

We consider Maxwell's equations (1.2), we assume a harmonic time dependence $\exp(-\imath\omega t)$ for all fields and a linear displacement vector $\mathbf{D} = \varepsilon\mathbf{E}$. Rescaling $\omega/c \to \omega$ we obtain

$$\nabla \times \mathbf{H} = -\imath\varepsilon\mathbf{E}, \qquad \nabla \times \mathbf{E} = \imath\omega^2\mathbf{H} \tag{3.2}$$

These equations can be written in the momentum representation and, if we consider the field components separately, we obtain a set of six equations

$$\imath\hat{k}_y h_z(z) - h'_y(z) = -\imath\hat{\varepsilon}e_x(z) \tag{3.3a}$$

$$h'_x(z) - \imath\hat{k}_x h_z(z) - = -\imath\hat{\varepsilon}e_y(z) \tag{3.3b}$$

$$\imath\hat{k}_x h_y(z) - \imath\hat{k}_y h_x(z) = -\hat{\varepsilon}e_z(z) \tag{3.3c}$$

and

$$\imath\hat{k}_y e_z(z) - e'_y(z) = \imath\omega^2 h_x(z) \tag{3.4a}$$

$$e'_x(z) - \imath\hat{k}_x e_z(z) - = \imath\omega^2 h_y(z) \tag{3.4b}$$

$$\imath\hat{k}_x e'_y - \imath\hat{k}_y e_x(z) = \imath\omega^2 h_z(z) \tag{3.4c}$$

where $h_i(z)$ and $e_i(z)$ are the in-plane fourier component vectors whose elements depend on the incident wave vector $\mathbf{k}$ and are a function of z. Here the symbol $(\prime)$ indicates partial derivative respect to the z coordinate[1]. The matrices $\hat{k}_x$ and $\hat{k}_y$ are diagonal, with $(\hat{k}_x)_{\mathbf{GG}} = (k_x + G_x)$ and $(\hat{k}_y)_{\mathbf{GG}} = (k_y + G_y)$, where G_x and G_y are the reciprocal lattice vector components. Finally the matrix $\hat{\varepsilon}$ is defined as $\hat{\varepsilon}_{\mathbf{GG}} = \tilde{\varepsilon}(\mathbf{G} - \mathbf{G}')$, where the symbol $\sim$ indicates the in-plane Fourier expansion of the dielectric function for a single layer. In practice, for a numerical calculation, the set of reciprocal lattice vector must be truncated, thus $h_i(z)$ and $e_i(z)$ have dimension N_G, while $\hat{k}_i$ and $\hat{\varepsilon}$ are $N_G \times N_G$ matrices.

Now the electromagnetic field is expanded in terms of plane waves, in basis state with zero divergence in order to guarantee $\nabla \cdot \mathbf{H} = 0$

$$\begin{aligned} H(\mathbf{r}, z) = \sum_{\mathbf{G}} \Bigg(& \phi_x(\mathbf{G}) \left[\hat{\mathbf{x}} - \frac{1}{q}(k_x + G_x)\hat{\mathbf{z}} \right] \\ & + \phi_y(\mathbf{G}) \left[\hat{\mathbf{y}} - \frac{1}{q}(k_y + G_y)\hat{\mathbf{z}} \right] \Bigg) e^{\imath(\mathbf{k}+\mathbf{G})\cdot\mathbf{r} + \imath q z} \end{aligned} \tag{3.5}$$

where $\phi_x(\mathbf{G})$ and $\phi_y(\mathbf{G})$ are the expansion coefficients, and $\hat{\mathbf{x}}, \hat{\mathbf{y}}$ and $\hat{\mathbf{z}}$ are conventional unit vectors that indicate axis directions. It is useful defining the vectors $\phi_x = [\phi_x(\mathbf{G_1}), \phi_x(\mathbf{G_1}), ...]^T$ and $\phi_y = [\phi_y(\mathbf{G_1}), \phi_y(\mathbf{G_1}), ...]^T$ in order to obtain in the momentum representation

$$\mathbf{h}(z) = e^{\imath q z} \left\{ \phi_x \hat{\mathbf{x}} + \phi_y \hat{\mathbf{y}} - \frac{1}{q}(\hat{k}_x \phi_x + \hat{k}_x \phi_y)\hat{\mathbf{z}} \right\}. \tag{3.6}$$

Using the Eqs. (3.6) and (3.3) it is possible providing an analogous expression for electric field Fourier components $e(z)$. Finally, by substituting these

[1]Note that the whole calculation is carried out for a fixed value of $\mathbf{k}$.

expressions in Eqs. (3.4), we get an asymmetric eigenvalue problem

$$\left\{ \begin{pmatrix} \hat{\varepsilon} & 0 \\ 0 & \hat{\varepsilon} \end{pmatrix} \left[\omega^2 - \begin{pmatrix} \hat{k}_y\hat{\eta}\hat{k}_y & -\hat{k}_y\hat{\eta}\hat{k}_x \\ -\hat{k}_x\hat{\eta}\hat{k}_y & \hat{k}_x\hat{\eta}\hat{k}_x \end{pmatrix} \right] - \begin{pmatrix} \hat{k}_x\hat{k}_x & \hat{k}_x\hat{k}_y \\ \hat{k}_y\hat{k}_x & \hat{k}_y\hat{k}_y \end{pmatrix} \right\} \times \begin{pmatrix} \phi_x \\ \phi_y \end{pmatrix} = q^2 \begin{pmatrix} \phi_x \\ \phi_y \end{pmatrix} \tag{3.7}$$

which can be written in a more compact form as

$$\left[\varepsilon(\omega^2 - \mathcal{K}) - K\right] \phi = q^2\phi \tag{3.8}$$

where $\varepsilon, \mathcal{K}$ and K are $2N \times 2N$ matrices. The eigenvectors ϕ_n and the corresponding eigenvalues q_n can be used in order to provide an expansion of $\mathbf{h}$ and $\mathbf{e}$ in terms of backward and forward propagating plane waves in the z direction

$$\begin{pmatrix} h_x(z) \\ h_y(z) \end{pmatrix} = \sum_n \begin{pmatrix} \phi_{x_n} \\ \phi_{y_n} \end{pmatrix} (e^{\imath q_n z} a_n + e^{\imath q_n (d-z)} b_n) \tag{3.9}$$

where d is the layer thickness, while a_n and b_n are the coefficients of the forward and backward going waves at z=0 and z=d interfaces, respectively. The Eq. (3.9) can be written in a more compact notation by introducing a diagonal matrix $\hat{f}(z)$, such that $\hat{f}_{nn}(z) = e^{\imath q_n z}$, and the vectors $h_\parallel(z) = [h_x(z), h_y(z)]^T$, $a = (a_1, a_2, ...)^T$ and $b = (b_1, b_2, ...)^T$

$$h_\parallel(z) = \Phi[\hat{f}(z)a + \hat{f}(d-z)b], \tag{3.10}$$

where the $2N \times 2N$ matrix Φ is composed by the column vectors ϕ_n.
Similarly it is possible providing an analogous expression for the electric field vector, defined as $e_\parallel(z) = [-e_y(z), e_x(z)]^T$,

$$e_\parallel(z) = (\omega^2 - \mathcal{K})\Phi\hat{q}^{-1}[\hat{f}(z)a - \hat{f}(d-z)b]. \tag{3.11}$$

Using the Eqs. (3.10) and (3.11) we can write

$$\begin{pmatrix} e_\parallel(z) \\ h_\parallel(z) \end{pmatrix} = \begin{pmatrix} (\omega^2 - \mathcal{K})\Phi\hat{q}^{-1} & (\omega^2 - \mathcal{K})\Phi\hat{q}^{-1} \\ \Phi & \Phi \end{pmatrix} \begin{pmatrix} \hat{f}(z)a \\ \hat{f}(d-z)b \end{pmatrix} \tag{3.12}$$

$$= M \begin{pmatrix} \hat{f}(z)a \\ \hat{f}(d-z)b \end{pmatrix} \tag{3.13}$$

Tangential field components must be continuous at the interface, thus the amplitudes a_l and b_l satisfy the relation

$$\begin{pmatrix} \hat{f}_l a_l \\ b_l \end{pmatrix} = I(l, l+1) \begin{pmatrix} a_{l+1} \\ \hat{f}_{l+1} b_{l+1} \end{pmatrix} \tag{3.14}$$

where $\hat{f}_l = \hat{f}_l(d_l)$, while the interface matrix is related to the layers matrices M_l and M_{l+1} by the simple equation

$$I(l, l+1) = M_l^{-1} M_{l+1} \tag{3.15}$$

Now we have all the elements in order to evaluate the total structure scattering matrix. If we consider two layers l and l', the scattering matrix $S(l', l)$ relates the field amplitude vectors in the following way

Scattering matrix

$$\begin{pmatrix} a_l \\ b_{l'} \end{pmatrix} = S(l', l) \begin{pmatrix} a_{l'} \\ b_l \end{pmatrix} = \begin{pmatrix} S_{11} & S_{12} \\ S_{21} & S_{22} \end{pmatrix} \begin{pmatrix} a_{l'} \\ b_l \end{pmatrix} \tag{3.16}$$

The total scattering matrix can be evaluated through an iterative procedure starting by the obvious relation $S(l, l) = 1$. The recipe is the following:

$$\begin{aligned}
S_{11}(l', l+1) &= (I_{11} - \hat{f}_l S_{12}(l', l) I_{21})^{-1} \hat{f}_l S_{11}(l' l) \\
S_{12}(l', l+1) &= (I_{11} - \hat{f}_l S_{12}(l', l) I_{21})^{-1} \\
&\quad \times (\hat{f}_l S_{12}(l'^{,l}) I_{22} - I_{12}) \hat{f}_{l+1} \\
S_{21}(l', l+1) &= S_{22}(l', l) I_{21} S_{11}(l', l+1) + S_{21}(l', l) \\
S_{22}(l', l+1) &= S_{22}(l', l) I_{21} S_{12}(l', l+1) + S_{22}(l', l) I_{22} \hat{f}_{l+1}
\end{aligned} \tag{3.17}$$

Once the scattering matrix $S(0, N)$ is found, the linear reflected and transmitted amplitudes can be easily evaluated

$$b_0 = S_{21}(0, N) a_0 \tag{3.18}$$

$$a_N = S_{11}(0, N) a_0 \tag{3.19}$$

Now it is only necessary to translate these amplitude into the electric and magnetic field [29].

3.3.2 Pump field propagation

In this section we briefly present how to evaluate the pump electric $\mathbf{E}_\omega(x, y, z)$ and the nonlinear polarization $\mathbf{P}^{NL}(x, y, z)$. As we have seen in Sec. 3.3.1, the electric field can be expanded in terms of an appropriate set of function and the expansion coefficients for the forward and backward propagating waves are a_l and b_l, respectively. Reference [29] has provided a simple expression for the amplitudes a_l and b_l in a generic l-th layer as a function of the reflected (a_0)and transmitted (b_N) amplitudes.

$$\begin{aligned}
a_l &= [1 - S_{12}(0, l) S_{21}(l, N)]^{-1} \\
&\times [S_{11}(0, l) a_0 + S_{12}(0, l) S_{22}(l, N) b_N],
\end{aligned} \tag{3.20}$$

$$\begin{aligned}
b_l &= [1 - S_{21}(l, N) S_{22}(0, l)]^{-1} \\
&\times [S_{21}(l, N) S_{11}(0, l) a_0 + S_{22}(l, N) b_N],
\end{aligned} \tag{3.21}$$

where $S(0,l)$ and $S(l,N)$ are the scattering matrices between the l-th layer and the first and last one, respectively.

Knowing the amplitudes a and b it is possible calculating the parallel components $\mathbf{e}_{\|}(z)$ using the relation (3.11), already given in Ref. [29]. Here we provide an analogous formula in order to evaluate even the component $e_z(z)$, that is required to the calculation of the nonlinear polarization

$$e_z(z) = \hat{\eta}(\hat{k}_y\Phi_x - \hat{k}_x\Phi_y)[\hat{\mathrm{f}}(z)a - \hat{\mathrm{f}}(d-z)b]. \tag{3.22}$$

Note that in this equation Φ_x and Φ_y are rectangular matrices $N\times 2N$, which are formed by the first N and last N rows of the matrix Φ respectively.

The electric field in the real space can now be evaluated as

$$E_i(x,y,z) = \sum_{\mathbf{G}} E_k(\mathbf{G},z)e^{i(\mathbf{k}+\mathbf{G})\cdot\mathbf{r}} \qquad i = x,y,z \tag{3.23}$$

and hence the nonlinear polarization can also be calculated. For example, in the third harmonic generation case we get

$$P_i^{3\omega}(x,y,z) = \sum_{j,k,h} \chi_{ijkh}(x,y,z)E_j(x,y,z)E_k(x,y,z)E_h(x,y,z). \tag{3.24}$$

It is worth to remember that in numerical calculation the field is evaluated only for certain finite ensemble of point and therefore the accuracy of the numerical results depends on the chosen mesh.

3.3.3 Solving the bound field problem in a single layer

We assume to work in the regime of negligible pump depletion, this approximation greatly simplifies the HG problem since $\mathbf{P}^{NL}$ is independent of the harmonic field so that the contribution of each layer can be treated independently as it happens in the transfer matrix formalism.

Nonlinear problem

If we assume an harmonic time dependence $e^{-i\omega t}$, where now ω indicates the *harmonic* frequency, we can write Maxwell equations (3.2) including nonlinear polarization terms:

$$\nabla\times\mathbf{H} = -i\epsilon\mathbf{E} - i\mathbf{P}^{\mathrm{NL}} \tag{3.25}$$

$$\nabla\times\mathbf{E} = i\omega^2\mathbf{H}. \tag{3.26}$$

The bound field is the particular solution of this non-homogeneous Maxwell equations in which the nonlinear polarization $\mathbf{P}^{NL}$ acts as a source of a harmonic electromagnetic field. In order to solve Eqs. (3.25) and (3.26) in a patterned multilayer system it is convenient to introduce a further simplification. Each layer is divided in N_{sub} thinner slices along the z direction, as shown in Fig.3.10. In each slice P^{NL} is taken constant and equal to:

$$\mathbf{P}^{NL}(\mathbf{r}) = \frac{1}{L}\int_0^L \mathbf{P}^{NL}(\mathbf{r},z)dz. \tag{3.27}$$

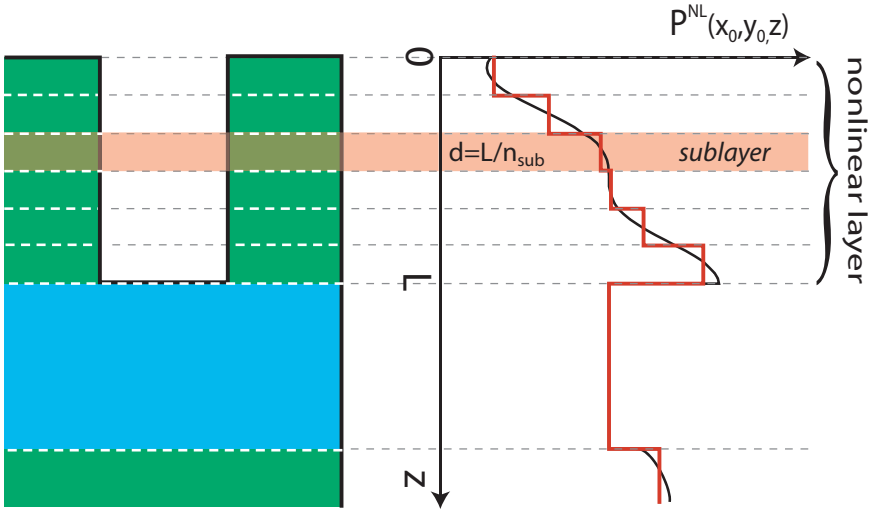

Figure 3.10: Discretization of nonlinear polarization along the vertical direction. Each nonlinear layer is divided in smaller sublayers where P^{NL} is taken equal to the averaged value.

where $L = d/N_{sub}$ is the subdivision length while d is the total layer width. The contribution of a single layer is the sum of all the subdivision contributions where P^{NL} is taken to be constant, now we have to solve the problem in each "sublayer" (see Fig. 3.10).Thus all the discussion henceforth will be referred to the generic single sublayer.

We expand $\mathrm{P^{NL}}$ in terms of plane waves

$$\mathbf{P^{NL}}(\mathbf{r}) = \sum_{\mathbf{G}} \tilde{\mathbf{P}}_{\mathbf{k}}(\mathbf{G}) e^{i(\mathbf{k}+\mathbf{G})\cdot\mathbf{r}} \tag{3.28}$$

where $\mathbf{G}$ are the reciprocal wave vectors defined by the layer pattern and $\mathbf{k}$ is the in-plane component of harmonic field wave-vector. It is convenient to define a new vector

$$\mathbf{p}(z) = \left[\tilde{\mathbf{P}}_{\mathbf{k}}(\mathbf{G}_1), \tilde{\mathbf{P}}_{\mathbf{k}}(\mathbf{G}_2), ...\right]^T \tag{3.29}$$

Now we write Eqs. (3.25) and (3.26) in a momentum representation and we obtain two equation sets analogous to Eqs (3.4) and (3.3)

$$\hat{k}_y h_z = -\hat{\varepsilon}\, e_x - p_x \tag{3.30a}$$
$$\hat{k}_x h_z = \hat{\varepsilon}\, e_y + p_y \tag{3.30b}$$
$$\hat{k}_x h_y - \hat{k}_y h_x = -\hat{\varepsilon}\, e_z - p_z \tag{3.30c}$$

and

$$\hat{k}_y e_z = \omega^2 h_x \tag{3.31a}$$

$$\hat{k}_x e_z = -\omega^2 h_y \tag{3.31b}$$

$$\hat{k}_x e_y - \hat{k}_y e_x = \omega^2 h_z \tag{3.31c}$$

There are two important differences: we have an additive nonlinear polarization term in the first set, which represents the source of harmonic fields and the z dependence is suppressed.

In order to evaluate the reflected and transmitted harmonic field we need to calculate the electric and magnetic bound tangential field components e_x, e_y, h_x and h_y. From (3.30a),(3.30b) and (3.31c) we obtain a linear non-homogeneous system in the bound components of the paralle electric field:

$$\left[\begin{pmatrix} \hat{k}_x\hat{k}_x & \hat{k}_x\hat{k}_y \\ \hat{k}_y\hat{k}_x & \hat{k}_y\hat{k}_y \end{pmatrix} - \omega^2 \begin{pmatrix} \hat{\varepsilon} & 0 \\ 0 & \hat{\varepsilon} \end{pmatrix}\right] \begin{pmatrix} -e_y \\ e_x \end{pmatrix} = \omega^2 \begin{pmatrix} -p_y \\ p_x \end{pmatrix} \tag{3.32}$$

which can be written in a more compact form as

$$(K - \omega^2 \varepsilon)\, e_{\parallel} = \omega^2 p_{\parallel} \tag{3.33}$$

where $p_{\parallel}=[-p_y, p_x]^T$. Analogously, using the equations (3.30c), (3.31a) and (3.31b), we obtain a system in h_x and h_y.

$$\left[\omega^2 - \begin{pmatrix} \hat{k}_y\hat{\eta}\hat{k}_y & -\hat{k}_y\hat{\eta}\hat{k}_x \\ -\hat{k}_x\hat{\eta}\hat{k}_y & \hat{k}_x\hat{\eta}\hat{k}_x \end{pmatrix}\right] \begin{pmatrix} h_x \\ h_y \end{pmatrix} = \omega^2 \begin{pmatrix} -\hat{k}_y\hat{\eta}p_z \\ \hat{k}_x\hat{\eta}p_z \end{pmatrix} \tag{3.34}$$

which can be written as

$$(\omega^2 - \mathcal{K})\, h_{\parallel} = p_{\perp} \tag{3.35}$$

where $p_{\perp}=[-\hat{k}_y\hat{\eta}p_z, \hat{k}_x\hat{\eta}p_z]^T$ The solution of these systems can be easily performed numerically. It is worth to notice that, for sublayers which belong to the same layer, the coefficient matrix of the linear system is the same. This fact has important consequence in the numerical implementation for what concerns the computing time.

3.3.4 Third-harmonic emission by a nonlinear layer

Once the bound field is known, the contribution of the nonlinear layer to reflected and transmitted harmonic field is evaluated by imposing continuity of tangential components of the field at layer interface. We consider the l-th layer and the interfaces $l/(l+1)$ and $(l\text{-}1)/l$, as shown in Fig. 3.11. In the nonlinear layer the total field is the sum of the bound contribution, which is constant, and the free harmonic field, while in the adjacent layers we have

Emission by a layer

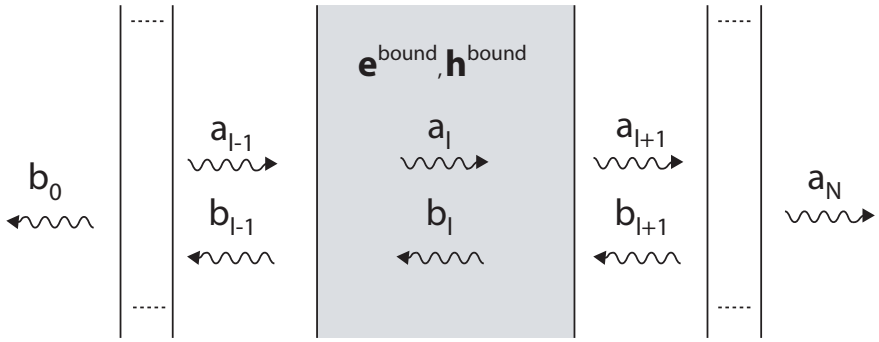

Figure 3.11: Nonlinear polarization generates in l-th layer bound electric and magnetic fields, solutions of the non-homogeneous problem. The terms are constant within the layer and have to be taken into account at the interfaces with $l-1/l$ and $l/l+1$. By imposing continuity of field tangential components it is possible evaluating reflected (b_0) and transmitted (a_n) nonlinear amplitudes.

only free harmonic contributions. The continuity relation can be written as

$$\mathbf{M}_{l-1}\begin{pmatrix} \hat{\mathrm{f}}_{l-1}a_{l-1} \\ b_{l-1} \end{pmatrix} - \mathbf{M}_l \begin{pmatrix} a_l \\ \hat{\mathrm{f}}_l b_l \end{pmatrix} = \begin{pmatrix} e_{\parallel}^{bound} \\ h_{\parallel}^{bound} \end{pmatrix} \tag{3.36}$$

$$\mathbf{M}_{l+1}\begin{pmatrix} a_{l+1} \\ \hat{\mathrm{f}}_{l+1}b_{l+1} \end{pmatrix} - \mathbf{M}_l \begin{pmatrix} \hat{\mathrm{f}}_l a_l \\ b_l \end{pmatrix} = \begin{pmatrix} e_{\parallel}^{bound} \\ h_{\parallel}^{bound} \end{pmatrix} \tag{3.37}$$

where $e_{\parallel}^{bound}$ and $h_{\parallel}^{bound}$ are the parallel components vector of the bound field, solutions of systems (3.32) and (3.34). Multiplying both Eqs. (3.36) and (3.37) by $\mathbf{M}_l^{-1}$ we get the nonlinear analogue of Eq. (3.14)

$$I(l,l-1)\begin{pmatrix} \hat{\mathrm{f}}_{l-1}a_{l-1} \\ b_{l-1} \end{pmatrix} = \begin{pmatrix} a_l \\ \hat{\mathrm{f}}_l b_l \end{pmatrix} + \begin{pmatrix} e'_{\parallel} \\ h'_{\parallel} \end{pmatrix} \tag{3.38a}$$

$$I(l,l+1)\begin{pmatrix} a_{l+1} \\ \hat{\mathrm{f}}_{l+1}b_{l+1} \end{pmatrix} = \begin{pmatrix} \hat{\mathrm{f}}_l a_l \\ b_l \end{pmatrix} + \begin{pmatrix} e'_{\parallel} \\ h'_{\parallel} \end{pmatrix} \tag{3.38b}$$

where

$$\begin{pmatrix} e'_{\parallel} \\ h'_{\parallel} \end{pmatrix} = M_l^{-1}\begin{pmatrix} e_{\parallel}^{bound} \\ h_{\parallel}^{bound} \end{pmatrix}$$

The boundary condition in the external media is that there are no incoming waves, therefore a_0=b_N=0. Using the scattering matrices given by the

resolution of the linear problem for the free harmonic field, we have that

$$a_{l-1} = S_{12}(0, l-1)b_{l-1} \tag{3.39a}$$
$$b_0 = S_{22}(0, l-1)b_{l-1} \tag{3.39b}$$
$$a_N = S_{11}(l+1, N)a_{l+1} \tag{3.39c}$$
$$b_{l+1} = S_{21}(l+1, N)a_{l+1}. \tag{3.39d}$$

Now, using equations (3.39a) and (3.39d) we can evaluate a_{l-1} and b_{l+1} and, substituting these expressions in (3.38a) and (3.38b), we obtain a linear algebraic systems in a_{l+1} and b_{l-1}.

$$\begin{pmatrix} R_{11} + R_{12}\hat{\mathrm{f}}_{l+1}S_{21}(l+1,N) & -\hat{\mathrm{f}}_l L_{11}\hat{\mathrm{f}}_{l-1}S_{12}(0,l-1) - \hat{\mathrm{f}}_l L_{12} \\ -\hat{\mathrm{f}}_l R_{21} - \hat{\mathrm{f}}_l R_{22}\hat{\mathrm{f}}_{l+1}S_{21}(l+1,N) & L_{21}\hat{\mathrm{f}}_{l-1}S_{12}(0,l-1) + L_{22} \end{pmatrix} \times$$
$$\times \begin{pmatrix} a_{l+1} \\ b_{l-1} \end{pmatrix} = \begin{pmatrix} (\mathrm{I} - \hat{\mathrm{f}}_l)e'_{\parallel} \\ (\mathrm{I} - \hat{\mathrm{f}}_l)h'_{\parallel} \end{pmatrix} \tag{3.40}$$

where we have indicated with L and R the interface matrices $I(l, l-1)$ and $I(l, l+1)$, respectively. Once this system has been solved we obtain b_0 and a_N through the relations (3.39b) and (3.39c), and therefore the reflected and transmitted contribution of l-th layer. Finally a sum over the nonlinear layer gives the total reflected and transmitted harmonic fields.

3.4 Conclusions

In this work we have presented some preliminary results concerning the analysis of third harmonic generation problem in a photonic crystal slab. These results have been compared with the nonlinear response of an unpatterned planar waveguide. The investigation has revealed an unexpected richness in nonlinear effect encountered. Theoretical results have been compared with experimental measurement, reaching a first partial agreement. Basically we observe an increase of THG efficiency when going from bulk silicon to SOI planar waveguide, due to a partial field confinement in the slab. The addition of a 1D pattern to the SOI waveguide can determine a dramatic improvement of the nonlinear response when pump radiation is resonant with a quasi-guided mode.
In order to increase the accuracy of theoretical results we have developed a new numerical method based on linear scattering matrix formalism, in order to calculate harmonic generation in patterned multilayer structure, in the approximation of negligible pump depletion.

Conclusions and future perspectives

In this work a theoretical study of second- and third- harmonic generation in photonic systems of present interest, such as planar microcavities and photonic crystals slabs, has been conducted. We believe that a better understanding of nonlinear effects in such systems is important for development of new optical devices, in which nonlinearities can be exploited in order to achieve new functionalities or to improve the existing ones.

Doubly resonant cavities have been already indicated as suitable systems in order to achieve great enhancement of second-harmonic conversion efficiency. We have shown that it is possible to realize a doubly resonant microcavity with periodic dielectric mirrors even when the refractive index dispersion cannot be compensated by birefringence, for example in cubic or amorphous materials. The design method, that we have developed in this work, has required an in-depth study of periodic dielectric Bragg reflectors and microcavities. In particular, we have given a complete description of optical properties of periodic dielectric mirrors, such as reflectance and phase delay, as a function of composition. We observed that, even though mirrors in *thick* and *thin* configuration can have similar reflectance, their phase behavior is complementary. This finding turned out to be crucial in DRM design, where refractive index dispersion is compensated by an appropriate engineering of mirror phase properties.
The use of periodic mirrors allows the design to be carried out by means of the photonic gap map concept and, analogously, a planar microcavity can be viewed as a one-dimensional photonic crystal with a repeated defect layer. In these systems the external angle of incidence is an important tuning parameter, which becomes a very powerful tool when input and output field polarizations are different, because of polarization splitting of cavity modes.
The study of second-harmonic generation in DRM has been performed in the presence of bulk and surface nonlinearities. In the first case we provided

a theoretical description of SHG in symmetric microcavities, giving an analytic expression for the cavity enhancement in phase-matching and anti phase-matching conditions. Numerical calculations have been performed on GaAs and AlGaAs cavities with Alox/AlGaAs dielectric mirrors. We have introduced the concepts of phase-matching and anti phase-matching with reference to microcavity systems. Furthermore we demonstrated that, in a doubly resonant microcavity with bulk nonlinearity, nonlinear polarization and harmonic field are phase-matched, or anti phase-matched, only within the cavity layer. The simulations were found to be in a satisfactory agreement with the analytical model, showing that the conversion efficiency in resonant cavities grows exponentially with the number N of mirror periods. In particular we demonstrated that in a phase-matched doubly resonant microcavity the cavity enhancement can be two orders of magnitude more intense than in the single resonant case.
We also performed a study of amorphous silicon nitride multilayer systems, where a second-order nonlinearity arises from symmetry breaking at the interface between two layers, and thus SHG is a surface effect. Numerical calculations have been performed using the nonlinear transfer matrix method, which has been adapted in order to describe surface nonlinearities. We have found good agreement with the first experimental results, thus opening the possibility to a more detailed investigations of such systems.

We presented some preliminary results on third-harmonic generation in photonic crystal slabs. The aim of this work was the understanding of the enhancement in THG due to resonant coupling of the pump field with a quasi-guided mode in a Silicon-On-Insulator one-dimensional patterned waveguides. First, the analysis of PhC-slabs has required a detailed study of the bare waveguide nonlinear response, in order to separate the THG enhancement due to the waveguide configuration from that determined by the photonic pattern. Theoretical and experimental results agree in showing that THG increases when going from bulk silicon to the SOI waveguide, because of vertical confinement, and from SOI to the patterned system, when the pump is coupled to a photonic mode. Preliminary theoretical results have shown only a partial agreement with measurements. Thus we have developed a new numerical method which, in principle, allows to describe nonlinear interactions in one- and two- dimensional patterned multilayer systems. This method has been presented in detail, nevertheless no numerical results have been presented since its numerical implementation has still to be completed. The great flexibility of this method opens the possibility to the study of harmonic generation and parametric conversion in a great variety of photonic systems.

Appendix A

Nonlinear Transfer Matrix Method

The transfer matrix method is a commonly used approach in order to study linear propagation in a one-dimensional multilayer structure. Here we present an extension which allows to treat harmonic generation process in the limit of negligible pump depletion [52].
We wish to emphasize that, when the effects of harmonic generation on pump field can be neglected, the nonlinear transfer matrix method is an exact solution of the problem and that the process can be divided in three independent steps: (i) linear propagation of the pump field, (ii) nonlinear polarization generation and (iii) propagation of the harmonic field through the structure. The central idea of the method is that, the total reflected and transmitted harmonic fields can be expressed as the sum of separate layer contributions from all nonlinear layers.

A.0.1 Linear transfer matrix method

Since we are working in the approximation of negligible pump depletion, we assume the pump field to propagate linearly in the multilayer. This fact can be expressed in terms of *interface* and *propagation* matrices, which allow to evaluate field amplitude variations at the interface between two layers and to describe the field propagation in an homogenous medium, respectively
We consider the multilayer shown in Fig.A.1 composed by n layers of width d_i and dielectric constant ϵ_i, with i=1,2,..,n. The axis z is normal to the structure and $x-z$ is the plane of incidence. If we assume an harmonic time dependence $\exp(-\imath\omega t)$, the electric field in each layer (for each polarization s or p) can be written as

$$E_j(\mathbf{r}) = [E_j^+ e^{\imath k_z z} + E_j^- e^{-\imath k_z z}] e^{\imath(k_x x - \omega t)} \tag{A.1}$$

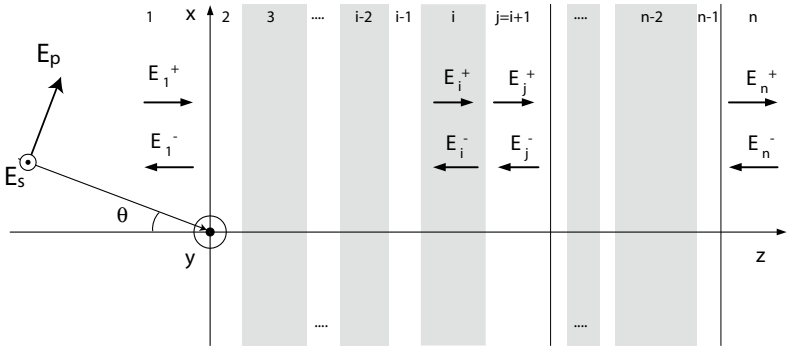

Figure A.1: Amplitude scheme in a multilayer

where k_z and k_x are the wave-vector components along axis x and z, respectively, while E_j^+ and E_j^- indicate forward and backward propagating wave amplitudes.
By imposing continuity of the tangential components of electric and magnetic fields at the interface i-j, we obtain a linear homogeneous system in field amplitudes $E_i^{+(-)}$ and $E_j^{+(-)}$. This systems can be expressed by the help of matrices in a more compact form

$$\mathbf{E}_i = \mathbf{M}_{ij}\mathbf{E}_j \tag{A.2}$$

where $\mathbf{E}_j$ is the vector of forward and backward propagating filed amplitudes in the i-th layer and $\mathbf{M}_{ij}$ is the *interface matrix* from the j-th to the i-th layer

Interface matrix

$$\mathbf{E}_j = \begin{bmatrix} E_j^+ \\ E_j^- \end{bmatrix}, \tag{A.3}$$

with

$$\mathbf{M}_{ij} = \frac{1}{t_{ij}} \begin{bmatrix} 1 & r_{ij} \\ r_{ij} & 1 \end{bmatrix}. \tag{A.4}$$

The elements t_{ij} and r_{ij} depend on field polarization and they result

$$r_{ij,s} = \frac{N_i - N_j}{N_i + N_j}, \quad t_{ij,s} = \frac{2N_i}{N_i + N_j} \tag{A.5}$$

and

$$r_{ij,p} = \frac{\epsilon_i N_j - \epsilon_j N_i}{\epsilon_i N_j + \epsilon_j N_i}, \quad t_{ij,p} = \frac{2[\epsilon_i \epsilon_j]^{1/2} N_i}{\epsilon_i N_j + \epsilon_j N_i}, \tag{A.6}$$

for s- and p- polarized fields, respectively. Here $N_j = \epsilon_j \cos\theta_j$, where θ_j is the refraction angle in j-th layer given by Snell's law.

The propagation of the electric field in the i-th layer is described using the *propagation* matrix Φ, which is defined as

$$\mathbf{E}_i(z_i + d_i) = \Phi_i \mathbf{E}_i(z_i) \tag{A.7}$$

and

Propagation matrix

$$\Phi_i = \begin{bmatrix} \phi_i & 0 \\ 0 & \bar{\phi}_i \end{bmatrix}, \tag{A.8}$$

where $\phi_i = \exp(\imath k_{z,i}\, d_i)$ and $\bar{\phi}_i$ represents field dephasing of forward and backward propagating waves, respectively.
The structure transfer matrix can be evaluated by simply multiplying interface and propagation matrices following the order given by multilayer structure:

Transfer matrix

$$\mathbf{T}_{n1} = \mathbf{M}_{n,n-1}\Phi_{n-1}\mathbf{M}_{n-1,n-2}\Phi_{n-2}\ldots\Phi_2\mathbf{M}_{21}. \tag{A.9}$$

Once the transfer matrix is found it is possible to evaluate linear reflectance and transmittance coefficient. In fact, in the hypothesis that the field is incident in the first layer, we can write

$$\begin{bmatrix} E_n^+ \\ 0 \end{bmatrix} = \begin{bmatrix} T_{11} & T_{12} \\ T_{21} & T_{22} \end{bmatrix} \begin{bmatrix} E_1^+ \\ E_1^- \end{bmatrix} \tag{A.10}$$

where E_1^+ is the incident field, while E_1^- and E_n^+ are the reflected and transmitted ones, respectively. Thus, reflectance and transmittance coefficients r and t result

$$r = \frac{E_1^-}{E_1^+} = -\frac{T_{21}}{T_{22}} \tag{A.11}$$

$$t = \frac{E_n^+}{E_1^+} = \frac{\det(\mathbf{T})}{T_{22}} \tag{A.12}$$

Once the reflectance coefficient is known, it is straightforward to evaluate the electric field amplitudes in the f-th layer. In fact, if we consider the amplitude vector of the firs layer $\mathbf{E}_1$, where $E_1^- = rE_1^+$, we obtain

$$\mathbf{E}_f = \mathbf{T}_{f1}\mathbf{E}_1 \tag{A.13}$$

where $\mathbf{T}_{f1}$ is the transfer matrix from the first to the f-th layer, evaluated by using Eq. (A.9) where n must be substituted with f.

A.0.2 Second harmonic generation by multilayer structures

The method, which has been described in the previous section, allows to study pump field propagation in a multilayer structure. Now we introduce

the hypothesis that one or more layers are made of nonlinear material, and we restrict ourselves to the case of second order nonlinearity [1].
In the approximation of negligible pump depletion, Maxwell equations become non-homogeneous linear differential equations so that the total field can be expressed as the sum of two contributions: a *free* electric field $\mathbf{E}$, solution of the corresponding homogeneous problem, and a *bound* electric $\mathbf{E}_s$, that is particular solution of non-homogenous wave equation [2]. In a homogeneous layer the particular solution can be analytically found and it results

$$\mathbf{E}_s = \frac{4\pi}{\epsilon_s - \epsilon_J}(\mathbf{P}_y^{NL} + \mathbf{P}_\perp^{NL}) - \frac{4\pi}{\epsilon_j}\mathbf{P}_\parallel^{NL}. \tag{A.14}$$

where $\epsilon_j = \epsilon_j(2\omega)$, $\epsilon_s = \epsilon_j(\omega)$ and $\mathbf{P}^{NL}$ is the nonlinear polarization which can be evaluated once nonlinear tensor $\chi^{(2)}$ is known. $\mathbf{P}_y$ is the s-polarized nonlinear polarization, while the components of p-polarized nonlinear polarization, which are parallel and orthogonal to the pump wave vector, are indicated with subscripts $\parallel$ and $\perp$, respectively.

The problem can be solved separately for each field polarization ($y, \parallel$ and $\perp$). From now we shall use $\mathbf{E}_s$ in order to indicate the generic bound field vector

$$\mathbf{E}_s = \begin{bmatrix} E_s^+ \\ E_s^- \end{bmatrix} \tag{A.15}$$

where E_s^+ and E_s^- indicate forward and backward waves amplitudes.
Because of the presence of bound field terms, the condition of tangential field components continuity must be reformulated by including $\mathbf{E}_s$. The resulting algebraic linear system can be written in a form similar to Eq. (A.2):

$$\mathbf{E}_i = \mathbf{M}_{ij}\mathbf{E}_j + \mathbf{M}_{ij}^{(s)}\mathbf{E}_J^{(s)} \tag{A.16}$$

Bound interface matrix

where $\mathbf{M}_{ij}^{(s)}$ is the *bound interface matrix* which have the same form of Eq. (A.4) but r_{ij} and t_{ij} depend on field polarization and have the following expressions:

$$r_{ij,s}^{(s)} = \frac{N_i - N_j^{(s)}}{N_i + N_j^{(s)}}, \qquad t_{ij,s}^{(s)} = \frac{2N_i}{N_i + N_j^{(s)}} \tag{A.17}$$

$$r_{ij,p\perp}^{(s)} = \frac{\epsilon_i(\omega)N_j - \epsilon_j(2\omega)N_i^{(s)}}{\epsilon_i(\omega)N_i + \epsilon_j(2\omega)N_i^{(s)}}, \quad t_{ij,p\perp}^{(s)} = \frac{2n_i(2\omega)n_j(\omega)N_i}{\epsilon_i(\omega)N_j + \epsilon_j(2\omega)N_i^{(s)}} \tag{A.18}$$

$$r_{ij,p\parallel}^{(s)} = -1, \qquad t_{ij,p\parallel}^{(s)} = \frac{2\cos\theta_{2\omega,i}}{\sin\theta_{\omega,j}}. \tag{A.19}$$

[1] The reader can find a complete treatment of third harmonic generation problem in Ref [52]

[2] All field and polarization terms are intended to be at 2ω.

where $N_j = \epsilon_j \cos\theta_{2\omega,j}$ and $N_j^{(s)} = \epsilon_s \cos\theta_{\omega,j}$.

In analogy with the linear problem, we can define the *bound propagation matrix*, which describe $\mathbf{E}_s$ propagation in the $j-th$ layer. This matrix is indicated with $\mathbf{\Phi}_s$ and it has the same form of (A.8), but with

$$\phi_j^{(s)} = e^{i(k_z, j^{(s)} d_j)}. \tag{A.20}$$

Let us calculate the j-th layer contributions to second harmonic field in the adjacent layers i and k. If we express the boundary condition at the interfaces $i-j$ and $j-k$ we obtain the following linear system

$$\begin{cases} \mathbf{E}_j(z_j) + \mathbf{M}_{ji}\mathbf{M}_{ij}^{(s)}\mathbf{E}_j(z_j)^{(s)} = \mathbf{M}_{ji}\mathbf{E}_i(z_i) \\ \mathbf{E}_k(z_k) = \mathbf{M}_{kj}\Phi_j\mathbf{E}_j(z_j) + \mathbf{M}_{kj}^{(s)}\Phi_j^{(s)}\mathbf{E}_j(z_j)^{(s)} \end{cases} \tag{A.21}$$

where (s) indicates all quantities referred to the bound field. From the first equation we evaluate $\mathbf{E}_j$, and if we substitute the result in the second of Eq. (A.21), we get:

$$\begin{aligned} \mathbf{E}_k(z_k) &= \mathbf{M}_{kj}\Phi_j\mathbf{M}_{ji}\mathbf{E}_i(z_i) \\ &+ (\mathbf{M}_{kj}^{(s)}\Phi_j^{(s)} - \mathbf{M}_{kj}\Phi_j\mathbf{M}_{ji}\mathbf{M}_{ij}^{(s)})\mathbf{E}_j(z_j)^{(s)}. \end{aligned} \tag{A.22}$$

Now we define the vector

$$\mathbf{S}_j = (\bar{\Phi_j}\mathbf{M}_{jk}\mathbf{M}_{kj}^{(s)}\Phi_j^{(s)} + \mathbf{M}_{ji}\mathbf{M}_{ij}^{(s)})\mathbf{E}_j(z_j)^{(s)} \tag{A.23}$$

and use the identity $T_{ki} = \mathbf{M}_{kj}\Phi_j\mathbf{M}_{ji}$, in order to write Eq. (A.22) as

$$\mathbf{E}_k(z_k) = \mathbf{T}_{ki}\mathbf{E}_i(z_i) + \mathbf{M}_{kj}\Phi_j\mathbf{S}_j \tag{A.24}$$

Note that the first part of Eq. (A.24) describes the linear propagation of the free harmonic field, while the terms containing $\mathbf{S}_j$ represents a field contribution originated by the nonlinear polarization.
Now, starting from Eq. (A.24), and putting $k = n$ and $i = 1$ we obtain

$$\mathbf{E}_n(z_n) = \mathbf{T}_{n1}\mathbf{E}_1(z_1) + \mathbf{M}_{nj}\Phi_j\mathbf{S}_j \tag{A.25}$$

If we assume that no harmonic fields are incident on the multilayer, we can write

$$\mathbf{R}_{jn}\begin{bmatrix} E_n^+(j) \\ 0 \end{bmatrix} - \mathbf{L}_{j1}\begin{bmatrix} 0 \\ E_1^-(j) \end{bmatrix} = \mathbf{S}_j \tag{A.26}$$

where we have multiplied both members of Eq. (A.25) by the transfer matrix from layer n to layer j $\mathbf{R}_{jn} = (\mathbf{M}_{nj}\Phi_j)^{-1}$, and we have defined the matrix $\mathbf{L}_{j1} = \mathbf{R}_{jn}\mathbf{T}_{n1}$, which is the transfer matrix from the first layer to

the j-th one.
Solving this linear system in the reflected and transmitted amplitudes, we obtain the contribution of the j-th layer:

$$\begin{bmatrix} E_n^+(j) \\ E_1^-(j) \end{bmatrix} = \frac{1}{R_{11}L_{22} - R_{21}L_{12}} \begin{bmatrix} L_{22} & -L_{12} \\ R_{21} & -R_{11} \end{bmatrix} \mathbf{S}_j. \tag{A.27}$$

Finally the total reflected and transmitted fields, for each polarization, are given by the sum over all nonlinear layers:

$$\begin{bmatrix} E_n^+ \\ E_1^- \end{bmatrix} = \sum_j \begin{bmatrix} E_n^+(j) \\ E_1^-(j) \end{bmatrix}. \tag{A.28}$$

Note in particular that p-polarized result is the sum of the ones obtained for parallel and orthogonal components of nonlinear polarization, that is

$$\begin{bmatrix} E_n^+ \\ E_1^- \end{bmatrix}_p = \sum_j \begin{bmatrix} E_n^+(j) \\ E_1^-(j) \end{bmatrix}_{p\perp} + \sum_j \begin{bmatrix} E_n^+(j) \\ E_1^-(j) \end{bmatrix}_{p\parallel}. \tag{A.29}$$

Appendix B

Units and Dimensions

Conversions Tables

Quantity	Gaussian	MKSA
Velocity of light	c	$(\mu_0\epsilon_0)^{-1/2}$
Electric field (potential or voltage)	$\mathbf{E}(\Phi, V)$	$\sqrt{4\pi\epsilon_0}\mathbf{E}(\Phi, V)$
Displacement	$\mathbf{D}$	$\sqrt{\frac{4\pi}{\epsilon_0}}\mathbf{D}$
Charge density (charge, current density, current, polarization)	$\rho(q, \mathbf{J}, I, \mathbf{P})$	$\frac{1}{4\pi\epsilon_0}\rho(q, \mathbf{J}, I, \mathbf{P})$
Magnetic induction (magnetization)	$\mathbf{B}(\mathbf{M})$	$\sqrt{\frac{4\pi}{\mu_0}}\mathbf{B}(\mathbf{M})$
Magnetic field	$\mathbf{H}$	$\sqrt{4\pi\mu_0}\mathbf{H}$
Conductivity	σ	$\frac{\sigma}{4\pi\epsilon_0}$
Dielectric constant	ϵ	$\frac{\epsilon}{\epsilon_0}$
Permeability	μ	$\frac{\mu}{\mu_0}$
Resistance (impedance,inductance)	$R(Z, L)$	$4\pi\epsilon_0 R(Z, L)$
Capacitance	C	$\frac{C}{4\pi\epsilon_0}$
Linear susceptibility	$\chi^{(1)}$	$\frac{1}{4\pi}\chi^{(1)}$
Second-order nonlinear susceptibility	$\chi^{(2)}$	$\frac{1}{4\pi\sqrt{4\pi\epsilon_0}}\chi^{(2)}$
Third-order nonlinear susceptibility	$\chi^{(3)}$	$\frac{1}{16\pi^2\epsilon_0}\chi^{(3)}$

Table B.1: To convert any equation in Gaussian variables to the corresponding MKSA quantities, on both side of the equation replace the relevant symbols listed below in the "Gaussian" column by the corresponding in the "MKSA" one. The reverse transformation is also allowed. Notice that the symbol of mass, length, time, force, and other not specifically electromagnetic quantities are unchanged. Quantities which differ dimensionally from one another only by power of length and/or time are grouped together where possible.

Conversions Tables for Given Amounts of Physical Quantity

Physical Quantity	Symbol	MKSA	Gaussian
Length	l	1 meter (m)	10^2 centimeters (cm)
Time	t	1 second (sec)	1 second (sec)
Mass	m	1 kilogram (Kg)	10^3 grams (g)
Force	F	1 Newton (N)	10^5 dynes
Energy	W	1 J	10^7 ergs
Power	P	1 W	10^7 ergs sec^{-1}
Charge	q	1 coulomb (C)	3×10^9 statcoulombs
Potential	V	1 volt	$\frac{1}{300}$ statvolt
Electric field	E	1 volt m^{-1}	$\frac{1}{3} \times 10^4$ statvolt cm^{-1}
Polarization	P	1 C m^{-2}	3×10^5 dipole moment cm^{-3}
Displacement	D	1 C m^{-2}	$12\pi \times 10^5$ statvolt cm^{-1}
Linear susceptibility	χ	1	$\frac{1}{4\pi}$
Second order suscept.	$\chi^{(2)}$	1 m V^{-1}	$\frac{3}{4\pi} \times 10^4$ esu
Third order suscept.	$\chi^{(3)}$	1 m^2 V^{-2}	$\frac{3^2}{4\pi} \times 10^8$ esu
n-th order suscept.	$\chi^{(n)}$	1 m^{n-1} V$^{-(n-1)}$	$\frac{3^{n-1}}{4\pi} \times (10^4)^{n-1}$ esu

Table B.2: The table provides the conversion of the most used physical quantities from the MKSA to the Gaussian system and viceversa. All factors of 3 (apart from exponents) should be replaced by (c=2.99792456). The second order nonlinear susceptibility are in general expressed in units of pm V^{-1}, where 1pm V^{-1}=$\frac{3}{4\pi} \times 10^{-8}$ esu.

Fundamental Constants and Conversions

Constant	Symbol	Value
Velocity of light	c	$2.99792456 \times 10^{10}$ cm$\cdot$ s^{-1}
Electron charge	$-e$	-4.803×10^{-10} esu
Electron mass	m_e	9.10953×10^{-28} g
Proton mass	m_p	1.67252×10^{-24} g
Plank constant	h	6.62559×10^{-27} erg$\cdot$ s^{-1}
		4.1357×10^{-15} eV$\cdot$Hz^{-1}
	$\hbar = h/2\pi$	1.054588×10^{-27} erg$\cdot$ s^{-1}
Boltzmann constant	k	1.380662×10^{-16} erg$\cdot$ K^{-1}
		0.861735×10^{27} eV$\cdot$ K^{-1}
Avogadro Number	N_A	6.022045×10^{23} mol^{-1}

1eV	=	1.602189×10^{-12} erg
(in frequency units)	=	2.41797×10^{14} Hz
(in wavenumber units)	=	8.06548×10^{3} cm^{-1}
(in wavelength units)	=	1.23984×10^{-4} cm
(in temperature units)	=	1.16045×10^{4} K

Bibliography

[1] J. A. Armstrong, N. Bloembergen, J. Ducuing, and P. S. Pershan. Interactions between light waves in a nonlinear dielectric. *Physical Review*, 127(6):1918–1939, 1962. URL `http://link.aip.org/link/?PR/127/1918/1`.

[2] Robert C. Miller and Albert Savage. Harmonic generation and mixing of cawo[sub 4]: Nd[sup 3 +] and ruby pulsed laser beams in piezoelectric crystals. *Physical Review*, 128(5):2175–2179, 1962. URL `http://link.aip.org/link/?PR/128/2175/1`.

[3] P. A. Franken, A. E. Hill, C. W. Peters, and G. Weinreich. Generation of optical harmonics. *Physical Review Letters*, 7(4):118–119, 1961. URL `http://link.aps.org/abstract/PRL/v7/p118`.

[4] M. Bass, P. A. Franken, A. E. Hill, C. W. Peters, and G. Weinreich. Optical mixing. *Physical Review Letters*, 8(1):18–18, 1962. URL `http://link.aps.org/abstract/PRL/v8/p18`.

[5] N. Bloembergen and A. J. Sievers. Nonlinear optical properties of periodic laminar structures. *Applied Physics Letters*, 17(11):483–486, 1970. URL `http://link.aip.org/link/?APL/17/483/1`.

[6] J. P. van der Ziel and M. Ilegems. Second harmonic generation in a thin alas-gaas multilayer structure with wave propagation in the plane of the layers. *Applied Physics Letters*, 29(3):200–202, 1976. URL `http://link.aip.org/link/?APL/29/200/1`.

[7] A. Fiore, E. Rosencher, V. Berger, and J. Nagle. Electric field induced interband second harmonic generation in gaas/algaas quantum wells. *Applied Physics Letters*, 67(25):3765–3767, 1995. URL `http://link.aip.org/link/?APL/67/3765/1`.

[8] A. Fiore, V. Berger, E. Rosencher, P. Bravetti, and J. Nagle. Phase matching using an isotropic nonlinear optical material. *Nature*, 391 (6666):463–466, 1998.

[9] K. L. Vodopyanov, K. O'Neill, G. B. Serapiglia, C. C. Phillips, M. Hopkinson, I. Vurgaftman, and J. R. Meyer. Phase-matched second harmonic generation in asymmetric double quantum wells. *Applied Physics Letters*, 72(21):2654–2656, 1998. URL `http://link.aip.org/link/?APL/72/2654/1`.

[10] G. D. Boyd A. Ashkin and J. M. Dziedzic. Resonant optical second harmonic generation and mixing. *IEEE J. Quantum Electronics*, QE-2: 109–123, 1966.

[11] Z. Y. Ou and H. J. Kimble. Enhanced conversion efficiency for harmonic generation with double resonance. *Optics Letters*, 18(13):1053–1055, 1993. URL `http://www.opticsinfobase.org/abstract.cfm?URI=OL-18-13-1053`.

[12] T. V. Dolgova, A. I. Maidikovskii, M. G. Martem'yanov, G. Marovsky, G. Mattei, D. Schuhmacher, V. A. Yakovlev, A. A. Fedyanin, and O. A. Aktsipetrov. Giant second harmonic generation in microcavities based on porous silicon photonic crystals. *JETP Letters*, 73(1):6–9, 2001. URL `http://link.aip.org/link/?JTP/73/6/1`.

[13] Vittorio Pellegrini, Raffaele Colombelli, Iacopo Carusotto, Fabio Beltram, Silvia Rubini, Roberta Lantier, Alfonso Franciosi, Claudio Vinegoni, and Lorenzo Pavesi. Resonant second harmonic generation in znse bulk microcavity. *Applied Physics Letters*, 74(14):1945–1947, 1999. URL `http://link.aip.org/link/?APL/74/1945/1`.

[14] V. Berger. Second-harmonic generation in monolithic cavities. *Journal of the Optical Society of America B: Optical Physics*, 14(6):1351–1360, 1997. URL `http://www.opticsinfobase.org/abstract.cfm?URI=JOSAB-14-6-1351`.

[15] C. Simonneau, J. P. Debray, J. C. Harmand, P. Vidakovic, D. J. Lovering, and J. A. Levenson. Second-harmonic generation in a doubly resonant semiconductor microcavity. *Optics Letters*, 22(23):1775–1777, 1997. URL `http://www.opticsinfobase.org/abstract.cfm?URI=OL-22-23-1775`.

[16] Marco Liscidini and Lucio Claudio Andreani. Highly efficient second-harmonic generation in doubly resonant planar microcavities. *Applied Physics Letters*, 85(11):1883–1885, 2004. URL `http://link.aip.org/link/?APL/85/1883/1`.

[17] see special issue Nonlinear Optics of Photonic Crystals. Nonlinear optics of photonic crystals. *Journal of the Optical Society of America B: Optical Physics*, 19(9):1961–2296, 2002. URL `http://www.opticsinfobase.org/abstract.cfm?URI=JOSAB-19-9-1961`.

[18] R.E. Slusher and B.J. Eggleton. *Nonlinear optics*, volume 10 of *Series in Photonics*. Springer, Berlin, 2003.

[19] M. Centini, C. Sibilia, M. Scalora, G. D'Aguanno, M. Bertolotti, M. J. Bloemer, C. M. Bowden, and I. Nefedov. Dispersive properties of finite, one-dimensional photonic band gap structures: Applications to nonlinear quadratic interactions. *Physical Review E (Statistical Physics, Plasmas, Fluids, and Related Interdisciplinary Topics)*, 60(4):4891–4898, 1999. URL `http://link.aps.org/abstract/PRE/v60/p4891`.

[20] Y. Dumeige, P. Vidakovic, S. Sauvage, I. Sagnes, J. A. Levenson, C. Sibilia, M. Centini, G. D'Aguanno, and M. Scalora. Enhancement of second-harmonic generation in a one-dimensional semiconductor photonic band gap. *Applied Physics Letters*, 78(20):3021–3023, 2001. URL `http://link.aip.org/link/?APL/78/3021/1`.

[21] G. D'Aguanno, M. Centini, M. Scalora, C. Sibilia, Y. Dumeige, P. Vidakovic, J. A. Levenson, M. J. Bloemer, C. M. Bowden, J. W. Haus, and M. Bertolotti. Photonic band edge effects in finite structures and applications to chi[sup (2)] interactions. *Physical Review E (Statistical, Nonlinear, and Soft Matter Physics)*, 64(1):016609, 2001. URL `http://link.aps.org/abstract/PRE/v64/e016609`.

[22] Giuseppe D'Aguanno, Marco Centini, Michael Scalora, Concita Sibilia, Mario Bertolotti, Mark J. Bloemer, and Charles M. Bowden. Generalized coupled-mode theory for chi[sup (2)] interactions in finite multilayered structures. *Journal of the Optical Society of America B: Optical Physics*, 19(9):2111–2121, 2002. URL `http://www.opticsinfobase.org/abstract.cfm?URI=JOSAB-19-9-2111`.

[23] Y. Dumeige, I. Sagnes, P. Monnier, P. Vidakovic, I. Abram, C. Meriadec, and A. Levenson. Phase-matched frequency doubling at photonic band edges: Efficiency scaling as the fifth power of the length. *Physical Review Letters*, 89(4):043901, 2002. URL `http://link.aps.org/abstract/PRL/v89/e043901`.

[24] Marco Centini, Giuseppe D'Aguanno, Letizia Sciscione, Concita Sibilia, Mario Bertolotti, Michael Scalora, and Mark J. Bloemer. Second

harmonic generation in one-dimensional photonic crystals: optimization procedure. volume 5450, pages 275–281. SPIE, 2004. URL http://link.aip.org/link/?PSI/5450/275/1.

[25] M. Notomi, K. Yamada, A. Shinya, J. Takahashi, C. Takahashi, and I. Yokohama. Extremely large group-velocity dispersion of line-defect waveguides in photonic crystal slabs. *Physical Review Letters*, 87(25):253902, 2001. URL http://link.aps.org/abstract/PRL/v87/e253902.

[26] D. Labilloy, H. Benisty, C. Weisbuch, T. F. Krauss, R. M. De La Rue, V. Bardinal, R. Houdre, U. Oesterle, D. Cassagne, and C. Jouanin. Quantitative measurement of transmission, reflection, and diffraction of two-dimensional photonic band gap structures at near-infrared wavelengths. *Physical Review Letters*, 79(21):4147–4150, 1997. URL http://link.aps.org/abstract/PRL/v79/p4147.

[27] A. R. Cowan and Jeff F. Young. Mode matching for second-harmonic generation in photonic crystal waveguides. *Physical Review B (Condensed Matter and Materials Physics)*, 65(8):085106, 2002. URL http://link.aps.org/abstract/PRB/v65/e085106.

[28] J. P. Mondia, H. M. van Driel, W. Jiang, A. R. Cowan, and Jeff F. Young. Enhanced second-harmonic generation from planar photonic crystals. *Optics Letters*, 28(24):2500–2502, 2003. URL http://www.opticsinfobase.org/abstract.cfm?URI=OL-28-24-2500.

[29] D. M. Whittaker and I. S. Culshaw. Scattering-matrix treatment of patterned multilayer photonic structures. *Physical Review B (Condensed Matter and Materials Physics)*, 60(4):2610–2618, 1999. URL http://link.aps.org/abstract/PRB/v60/p2610.

[30] F. Zernike and J. E. Midwinter. *Applied Nonlinear Optics*. Wiley, New York, 1930.

[31] Y. R. Shen. *The principles of Nonlinear Optics*. Wiley, New York, 1984.

[32] D. L. Mills. *Nonlinear Optics*. Springer, New York, 1998.

[33] N. Bloembergen. *Nonlinear optics*. Benjamin, New York, 1965.

[34] Robert C. Miller. Optical second harmonic generation in piezoelectric crystals. *Applied Physics Letters*, 5(1):17–19, 1964. URL http://link.aip.org/link/?APL/5/17/1.

[35] R. K. Chang, J. Ducuing, and N. Bloembergen. Dispersion of the optical nonlinearity in semiconductors. *Physical Review Letters*, 15(9): 415–418, 1965. URL `http://link.aps.org/abstract/PRL/v15/p415`.

[36] J. J. Wynne and G. D. Boyd. Study of optical difference mixing in ge and si using a co[sub 2] gas laser. *Applied Physics Letters*, 12(5): 191–192, 1968. URL `http://link.aip.org/link/?APL/12/191/1`.

[37] P. A. Wolff and Gary A. Pearson. Theory of optical mixing by mobile carriers in semiconductors. *Physical Review Letters*, 17(19):1015–1017, 1966. URL `http://link.aps.org/abstract/PRL/v17/p1015`.

[38] Federico Capasso, Jerome Faist, and Carlo Sirtori. Mesoscopic phenomena in semiconductor nanostructures by quantum design. *Journal of Mathematical Physics*, 37(10):4775–4792, 1996. URL `http://link.aip.org/link/?JMP/37/4775/1`.

[39] Federico Capasso. Band-gap engineering: from physics and materials to new semiconductor devices. *Science*, 235:172–176, 1987.

[40] N. Bloembergen and P. S. Pershan. Light waves at the boundary of nonlinear media. *Physical Review*, 128(2):606–622, 1962. URL `http://link.aip.org/link/?PR/128/606/1`.

[41] R. W. Terhune, P. D. Maker, and C. M. Savage. Optical harmonic generation in calcite. *Physical Review Letters*, 8(10):404–406, 1962. URL `http://link.aps.org/abstract/PRL/v8/p404`.

[42] J. A. Giordmaine. Mixing of light beams in crystals. *Physical Review Letters*, 8(1):19–20, 1962. URL `http://link.aps.org/abstract/PRL/v8/p19`.

[43] Jordi Martorell, R. Vilaseca, and R. Corbalan. Second harmonic generation in a photonic crystal. *Applied Physics Letters*, 70(6):702–704, 1997. URL `http://link.aip.org/link/?APL/70/702/1`.

[44] Fielding Brown, Robert E. Parks, and Arthur M. Sleeper. Nonlinear optical reflection from a metallic boundary. *Physical Review Letters*, 14(25):1029–1031, 1965. URL `http://link.aps.org/abstract/PRL/v14/p1029`.

[45] C. H. Lee, R. K. Chang, and N. Bloembergen. Nonlinear electroreflectance in silicon and silver. *Physical Review Letters*, 18(5):167–170, 1967. URL `http://link.aps.org/abstract/PRL/v18/p167`.

[46] N. Bloembergen, R. K. Chang, S. S. Jha, and C. H. Lee. Optical second-harmonic generation in reflection from media with inversion symmetry. *Physical Review*, 174(3):813–822, 1968. URL `http://link.aip.org/link/?PR/174/813/1`.

[47] M. Falasconi, L.C. Andreani, A.M. Malvezzi, M. Patrini, V. Mulloni, and L. Pavesi. Bulk and surface contributions to second-order susceptibility in crystalline and porous silicon by second-harmonic generation. *Surface Science*, 481:105–112, 2001.

[48] P. Guyot-Sionnest, W. Chen, and Y. R. Shen. General considerations on optical second-harmonic generation from surfaces and interfaces. *Physical Review B (Condensed Matter)*, 33(12):8254–8263, 1986. URL `http://link.aps.org/abstract/PRB/v33/p8254`.

[49] H. W. K. Tom, C. M. Mate, X. D. Zhu, J. E. Crowell, T. F. Heinz, G. A. Somorjai, and Y. R. Shen. Surface studies by optical second-harmonic generation: The adsorption of o[sub [bold 2]], co, and sodium on the rh(111) surface. *Physical Review Letters*, 52(5):348–351, 1984. URL `http://link.aps.org/abstract/PRL/v52/p348`.

[50] X. D. Zhu, Th. Rasing, and Y. R. Shen. Surface diffusion of co on ni(111) studied by diffraction of optical second-harmonic generation off a monolayer grating. *Physical Review Letters*, 61(25):2883–2885, 1988. URL `http://link.aps.org/abstract/PRL/v61/p2883`.

[51] T. F. Heinz, M. M. T. Loy, and W. A. Thompson. Study of si(111) surfaces by optical second-harmonic generation: Reconstruction and surface phase transformation. *Physical Review Letters*, 54(1):63–66, 1985. URL `http://link.aps.org/abstract/PRL/v54/p63`.

[52] D. S. Bethune. Optical harmonic generation and mixing in multilayer media: analysis using optical transfer matrix techniques. *Journal of the Optical Society of America B: Optical Physics*, 6(5):910–916, 1989. URL `http://www.opticsinfobase.org/abstract.cfm?URI=JOSAB-6-5-910`.

[53] T.F. Heinz. *Nonlinear Optics of Surfaces and Interfaces, PhD Dissertation*. PhD thesis, Berkeley, 1982. URL `http://heinz.phys.columbia.edu`.

[54] Fang-Fang Ren, Rui Li, Chen Cheng, Hui-Tian Wang, Jianrong Qiu, Jinhai Si, and Kazuyuki Hirao. Giant enhancement of second harmonic generation in a finite photonic crystal with a single defect and dual-localized modes. *Physical Review B (Condensed Matter and Materials Physics)*, 70(24):245109, 2004. URL `http://link.aps.org/abstract/PRB/v70/e245109`.

[55] J.D. Joannopoulos, R.D. Meade, and J.N.Winn. *Photonic Crystals*. Princeton University Press, Princeton, 1995.

[56] P. Yeh and A. Yariv. *Optical Waves in Crystals*. Wiley Series in Pure ans Applied Optics. Wiley, New York, 1984.

[57] E.D. Palik. *Handbook of Optical Constants of Solids II*. Academic, Orlandok, 1991.

[58] Joseph H. Apfel. Graphical method to design multilayer phase retarders. *Applied Optics*, 20(6):1024–1029, 1981. URL `http://www.opticsinfobase.org/abstract.cfm?URI=AO-20-6-1024`.

[59] Joseph H. Apfel. Phase retardance of periodic multilayer mirrors. *Applied Optics*, 21(4):733–738, 1982. URL `http://www.opticsinfobase.org/abstract.cfm?URI=AO-21-4-733`.

[60] H.A. McLeod. *Thin-Film Optical Filters 2nd ed.* Hilger, 1986.

[61] A. Tsigopoulos, T. Sphicopoulos, I. Orfanos, and S. Pantelis. Wavelength tuning analysis and spectral characteristics ofthree-section dbr lasers. *IEEE Journal of Quantum Electronics*, 28(2):415–426, 1992.

[62] Giovanna Panzarini, Lucio Claudio Andreani, A. Armitage, D. Baxter, M. S. Skolnick, V. N. Astratov, J. S. Roberts, Alexey V. Kavokin, Maria R. Vladimirova, and M. A. Kaliteevski. Exciton-light coupling in single and coupled semiconductor microcavities: Polariton dispersion and polarization splitting. *Physical Review B (Condensed Matter and Materials Physics)*, 59(7):5082–5089, 1999. URL `http://link.aps.org/abstract/PRB/v59/p5082`.

[63] M. Galli, M. Belotti, D. Bajoni, M. Patrini, G. Guizzetti, D. Gerace, M. Agio, L. C. Andreani, and Y. Chen. Excitation of radiative and evanescent defect modes in linear photonic crystal waveguides. *Physical Review B (Condensed Matter and Materials Physics)*, 70(8):081307, 2004. URL `http://link.aps.org/abstract/PRB/v70/e081307`.

[64] R. P. Stanley, R. Houdre, U. Oesterle, M. Ilegems, and C. Weisbuch. Impurity modes in one-dimensional periodic systems: The transition from photonic band gaps to microcavities. *Physical Review A (Atomic, Molecular, and Optical Physics)*, 48(3):2246–2250, 1993. URL `http://link.aps.org/abstract/PRA/v48/p2246`.

[65] A. A. Dukin, N. A. Feoktistov, V. G. Golubev, A. V. Medvedev, A. B. Pevtsov, and A. V. Sel'kin. Polarization splitting of optical resonant modes in a-si:h/a-sio[sub x]:h microcavities. *Physical Review E (Statistical, Nonlinear, and Soft Matter Physics)*, 67(4):046602, 2003. URL `http://link.aps.org/abstract/PRE/v67/e046602`.

[66] M. Ohashi, T. Kondo, R. Ito, S. Fukatsu, Y. Shiraki, K. Kumata, and S. S. Kano. Determination of quadratic nonlinear optical coefficient of al[sub x]ga[sub 1 - x]as system by the method of reflected second harmonics. *Journal of Applied Physics*, 74(1):596–601, 1993. URL `http://link.aip.org/link/?JAP/74/596/1`.

[67] Marco Liscidini and Lucio Claudio Andreani. Second harmonic generation in doubly resonant microcavities with periodic dielectric mirrors. *submitted to Physical Review E (Statistical Physics, Plasmas, Fluids, and Related Interdisciplinary Topics)*, 2005.

[68] W. M. M. Kessels, J. J. H. Gielis, I. M. P. Aarts, C. M. Leewis, and M. C. M. van de Sanden. Spectroscopic second harmonic generation measured on plasma-deposited hydrogenated amorphous silicon thin films. *Applied Physics Letters*, 85(18):4049–4051, 2004. URL `http://link.aip.org/link/?APL/85/4049/1`.

[69] K. Pedersen and P. Morgen. Dispersion of optical second-harmonic generation from si(111)7 x 7. *Physical Review B (Condensed Matter)*, 52(4):R2277–R2280, 1995. URL `http://link.aps.org/abstract/PRB/v52/pR2277`.

[70] S. Lettieri, S. Di Finizio, P. Maddalena, V. Ballarini, and F. Giorgis. Second-harmonic generation in amorphous silicon nitride microcavities. *Applied Physics Letters*, 81(25):4706–4708, 2002. URL `http://link.aip.org/link/?APL/81/4706/1`.

[71] Fabrizio Giorgis. Optical microcavities based on amorphous silicon–nitride fabry–p[e-acute]rot structures. *Applied Physics Letters*, 77(4): 522–524, 2000. URL `http://link.aip.org/link/?APL/77/522/1`.

[72] V. Ballarini, G. Barucca, E. Bennici, C.F. Pirri, C. Ricciardi, E. Tresso, and F. Giorgis. Second-harmonic generation in amorphous silicon nitride microcavities. *Physica E*, 16:591–595, 2003. URL `http://www.sciencedirect.com`.

[73] A. Feigel, Z. Kotler, and B. Sfez. Effective second-order susceptibility in photonic crystals mode of centrosymmetric materials. *Physical Review B (Condensed Matter and Materials Physics)*, 65(7):073105, 2002. URL `http://link.aps.org/abstract/PRB/v65/e073105`.

[74] S. Lettieri, F. Gesuele, P. Maddalena, M. Liscidini, L. C. Andreani, C. Ricciardi, V. Ballarini, and F. Giorgis. Second-harmonic generation in hydrogenated amorphous-si[sub 1 - x]n[sub x] doubly resonant microcavities with periodic dielectric mirrors. *Applied Physics Letters*, 87(19):191110, 2005. URL `http://link.aip.org/link/?APL/87/191110/1`.

[75] Y. S. Kivshar and G. P. Agrawal. *Optical solitons: from fibers to photonic crystals*. Academic Press, Amsterdam, 2003.

[76] M. L. Dowell, R. C. Hart, A. Gallagher, and J. Cooper. Self-focused light propagation in a fully saturable medium: Experiment. *Physical Review A (Atomic, Molecular, and Optical Physics)*, 53(3):1775–1781, 1996. URL `http://link.aps.org/abstract/PRA/v53/p1775`.

[77] F. S. Felber and J. H. Marburger. Theory of nonresonant multistable optical devices. *Applied Physics Letters*, 28(12):731–733, 1976. URL `http://link.aip.org/link/?APL/28/731/1`.

[78] J. H. Marburger and F. S. Felber. Theory of a lossless nonlinear fabry-perot interferometer. *Physical Review A (General Physics)*, 17(1):335–342, 1978. URL `http://link.aps.org/abstract/PRA/v17/p335`.

[79] H. M. Gibbs, T. N. C. Venkatesan, S. L. McCall, A. Passner, A. C. Gossard, and W. Wiegmann. Optical modulation by optical tuning of a cavity. *Applied Physics Letters*, 34(8):511–514, 1979. URL `http://link.aip.org/link/?APL/34/511/1`.

[80] H. M. Gibbs, S. L. McCall, T. N. C. Venkatesan, A. C. Gossard, A. Passner, and W. Wiegmann. Optical bistability in semiconductors. *Applied Physics Letters*, 35(6):451–453, 1979. URL `http://link.aip.org/link/?APL/35/451/1`.

[81] W. K. Burns and N. Bloembergen. Third-harmonic generation in absorbing media of cubic or isotropic symmetry. *Physical Review B (Solid State)*, 4(10):3437–3450, 1971. URL `http://link.aps.org/abstract/PRB/v4/p3437`.

[82] Charles C. Wang, J. Bomback, W. T. Donlon, C. R. Huo, , and J. V. James. Optical third-harmonic generation in reflection from crystalline and amorphous samples of silicon. *Physical Review Letters*, 57(13):1647–1650, 1986. URL `http://link.aps.org/abstract/PRL/v57/p1647`.

[83] M. Galli, D. Bajoni, M. Patrini, G. Guizzetti, D. Gerace, L. C. Andreani, M. Belotti, and Y. Chen. Single-mode versus multimode behavior in silicon photonic crystal waveguides measured by attenuated total reflectance. *Physical Review B (Condensed Matter and Materials Physics)*, 72(12):125322, 2005. URL `http://link.aps.org/abstract/PRB/v72/e125322`.

[84] V. N. Astratov, D. M. Whittaker, I. S. Culshaw, R. M. Stevenson, M. S. Skolnick, T. F. Krauss, and R. M. De La Rue.

Photonic band-structure effects in the reflectivity of periodically patterned waveguides. *Physical Review B (Condensed Matter and Materials Physics)*, 60(24):R16255–R16258, 1999. URL http://link.aps.org/abstract/PRB/v60/pR16255.

[85] M. Patrini, M. Galli, F. Marabelli, M. Agio, L.C. Andreani, and Y. Chen D. Peyrade. Photonic bands in patterned silicon-on-insulator waveguides. *IEEE Journal of Quantum Electronics*, 38(7):885–890, 2002.

[86] A. M. Malvezzi, G. Vecchi, M. Patrini, G. Guizzetti, L. C. Andreani, F. Romanato, L. Businaro, E. Di Fabrizio, A. Passaseo, and M. De Vittorio. Resonant second-harmonic generation in a gaas photonic crystal waveguide. *Physical Review B (Condensed Matter and Materials Physics)*, 68(16):161306, 2003. URL http://link.aps.org/abstract/PRB/v68/e161306.

[87] J. Torres, D. Coquillat, R. Legros, J. P. Lascaray, F. Teppe, D. Scalbert, D. Peyrade, Y. Chen, O. Briot, M. Le Vassor d'Yerville, E. Centeno, D. Cassagne, and J. P. Albert. Giant second-harmonic generation in a one-dimensional gan photonic crystal. *Physical Review B (Condensed Matter and Materials Physics)*, 69(8):085105, 2004. URL http://link.aps.org/abstract/PRB/v69/e085105.

[88] Gabriele Vecchi, Andrea M. Malvezzi, Maddalena Patrini, Giorgio Guizzetti, Lucio C. Andreani, Marco Liscidini, Yong Chen, and David Peyrade. Nonlinear optical studies of one-dimensional soi photonic crystal slabs. volume 5450, pages 260–268. SPIE, 2004. URL http://link.aip.org/link/?PSI/5450/260/1.

[89] Philippe Lalanne and G. Michael Morris. Highly improved convergence of the coupled-wave method for tm polarization. *Journal of the Optical Society of America A: Optics, Image Science, and Vision*, 13(4):779–784, 1996. URL http://www.opticsinfobase.org/abstract.cfm?URI=JOSAA-13-4-779.

[90] M. G. Moharam, Eric B. Grann, Drew A. Pommet, and T. K. Gaylord. Formulation for stable and efficient implementation of the rigorous coupled-wave analysis of binary gratings. *Journal of the Optical Society of America A: Optics, Image Science, and Vision*, 12(5):1068–1076, 1995. URL http://www.opticsinfobase.org/abstract.cfm?URI=JOSAA-12-5-1068.

[91] Evgeny Popov. Light diffraction by relef grating: a macroscopic and microscopic view. *Progress in Optics*, 31:141, 1993.

[92] Erwin G. Loewen and Evgeny Popov. *Diffraction Gratings and Applications*. Optical engineering. Marcell Dekker Inc. , New York, 1997.

List of publications and Conference Presentations

Publications:

1. M. Liscidini and L. C. Andreani "Highly efficient second-harmonic generation in doubly resonant planar microcavities," *Appl. Phys. Lett.* **85**, 1883 (2004)

2. M. Liscidini and L. C. Andreani "Second Harmonic Generation in Doubly Resonant Microcavity with Periodic dielectric Mirrors," *Phys. Rev. E* (2005) in press

3. S. Lettieri, F. Giosuele, P. Maddalena, M. Liscidini, L. C. Andreani, C. Ricciardi, V. Ballarini and F. Giorgis "Second Harmonic Generation in a-$Si_{1-x}N_x$:H doubly resonant microcavities with periodic dielectric mirrors," *Appl. Phys. Lett.* **87**, 191110 (2005)

4. G. Vecchi, A. M. Malvezzi, M. Patrini, G. Guizzetti, L. C. Andreani, M. Liscidini, Y. Chen, and D. Peyrade "Nonlinear optical studies of one-dimensional SOI photonic crystal slabs," *Proc. SPIE Int. Soc. Opt. Eng.* **5450**, 260 (2004)

5. C. Comsachi, G. Vecchi, A. M. Malvezzi, M. Patrini, G. Guizzetti, M. Liscidini, L. C. Andreani, D. Peyrade and Y. Chen "Enhanced third harmonic reflection and diffraction in Silicon on Insulator photonic waveguides," *Appl. Phys. B* **81**, 305 (2005)

Contributed Talks:

1. M. Liscidini and L. C. Andreani "COST P11 Meeting, " Roma, Italia, October 17-20, 2004

2. M. Liscidini and L. C. Andreani, "International Quantum electronics Conference 2005 and the Pacific Rim Conference on Lasers and Electro-Optics 200", Tokyo, Japan, July 11-15, 2005

3. M. Liscidini, D. Gerace and L. C. Andreani, "SPIE International Congress on Optics and Optoelectronics", Warsaw, Poland, 28 August - 2 September, 2005

Acknowledgements

I would like to gratefully thank Maria and our families for their continuous support and love during these wonderful years.

This work could not be carried out without my supervisor Prof. Lucio Claudio Andreani to which I am grateful for his patient guidance and outstanding kindness. I am sure that his teaching and example will be very precious for all my future research activities.

I would like to take the present opportunity to acknowledge Mario Agio who strongly helped me during my graduation thesis and the beginning of the PhD.

My deep gratefulness is for all the "Optical Spectroscopy group", in particular to Alessandra, Davide, Eva, Gabriele and Maddalena. A special acknowledgement to Dario for the English revision and to Michele for his very useful LaTeX suggestions

A special acknowledgement to Giacomo Bormetti for the stimulating work pauses and discussions.

Finally, I wish to acknowledge all the people who share with me the days at the Department of Physics "A. Volta" and continuously offer me outstanding personal growth occasions. Among them I wish to mention in particular Andrea Vai and Pietro Galinetto.

This work is entirely dedicated to Daniele Bajoni, Dario Gerace and Matteo Galli, with which I share sincere passion for the physics and a deep friendship.